UNIVERSITY OF SOUTHAMPTON

FACULTY OF ENGINEERING, SCIENCE AND MATHEMATICS

School of Engineering Sciences

DEVELOPMENTS IN REDOX FLOW BATTERIES

by

Ravichandra Tangirala B.Tech, M.Sc

Thesis for the degree of Doctor of Philosophy

May 2011

UNIVERSITY OF SOUTHAMPTON

ABSTRACT

FACULTY OF ENGINEERING, SCIENCE & MATHEMATICS

SCHOOL OF ENGINEERING SCIENCES

Doctor of Philosophy

Developments in Redox Flow Batteries

by Ravichandra Tangirala B.Tech, M.Sc

This thesis describes the investigation of the electrochemistry principles, technology, construction and composition of the electrode materials, electrolyte and additives used in redox flow batteries. The aim was to study a flow battery system with an appreciable working performance.

The study explores and compares mainly three different redox flow battery technologies; all-vanadium, soluble lead-acid and a novel copper-lead dioxide flow batteries. The first system is based in sulfuric acid electrolyte environment whilst the other two are in methanesulfonic acid. Various cell parameters such as cell voltage, individual electrode potentials, flow rate and efficiencies (in particular voltage, charge and energy) have been utilized to compare.

Further research in other redox couples and comparative study towards the design, construction and electrochemistry, along with the performance of these three batteries in relation to other electrochemical energy storage technologies available was also discussed. These technological studies are of particular interest for applications in the renewable energy storage (offshore and onshore) and sustainable energy research (grid integration and micro generation).

Contents

List of tables (Page No.)

Chapter I

Chapter II

Chapter III

Chapter IV

Chapter IV

List of figures (Page No.)

Chapter I

Chapter II

Chapter III

Chapter IV

DECLARATION OF AUTHORSHIP

I, ……***Ravichandra . Tangirala***……,

declare that the thesis entitled

……..……..***Developments in Redox Flow Batteries***……..……

and the work presented in the thesis are both my own, and have been generated by me as the result of my own original research. I confirm that:

- this work was done wholly or mainly while in candidature for a research degree at this University;
- where any part of this thesis has previously been submitted for a degree or any other qualification at this University or any other institution, this has been clearly stated;
- where I have consulted the published work of others, this is always clearly attributed;
- where I have quoted from the work of others, the source is always given. With the exception of such quotations, this thesis is entirely my own work;
- I have acknowledged all main sources of help;
- where the thesis is based on work done by myself jointly with others, I have made clear exactly what was done by others and what I have contributed myself;
- parts of this work have been published as

1. *"A novel flow battery: A lead acid battery based on an electrolyte with soluble lead(II) Part VIII. The cycling of a 10 cm×10cm flow cell*", J. Collins, G. Kear, X. Li, C.T.J. Low, D. Pletcher, **R.C. Tangirala**, D. Stratton-Campbell, F.C. Walsh and C. Zhang, Journal of Power Sources, **195** (2009) 1731.

2. *"A novel flow battery: A lead acid battery based on an electrolyte with soluble lead(II) Part IX: Electrode and electrolyte conditioning with hydrogen peroxide*", J. Collins, G. Kear, X. Li, C.T.J. Low, D. Pletcher, **R.C. Tangirala**, D. Stratton-Campbell, F.C. Walsh and C. Zhang, Journal of Power Sources, **195** (2009) 2975.

3. *"Copper deposition at segmented, reticulated vitreous carbon cathode in Hull cell* ", **R.C. Tangirala**, C.T.J. Low, C. Ponce-de-León, F.C. Walsh, Transactions of the Institute of Metal Finishing, **88** (2010) 84.

4. *"A semi-empirical model of All-vanadium redox flow battery"*, **R.C. Tangirala**, A.A. Shah, R.G.A. Wills, R. Singh and F.C. Walsh, J. Electrochem. Soc., **158** (2011) A671(Article in press).

Signed: ……..

Date:…….

Acknowledgements

I am most grateful to **Prof. F.C. Walsh and Dr. Carlos Ponce-de-León Albarrán,** both are the personal inspiration behind this research work and the following peer reviewed literature, during these three years at the University of Southampton. I am also thankful to Prof. D. Pletcher for his guidance and support over the years. I am also indebted to the Electrochemical Engineering Laboratory postdoctoral personnel and senior staff, Dr. Gareth Kear and Dr. Xiaohong Li in particular; whose help made my progression a smooth and knowledgeable journey. My special gratitude also go to Dr. R.G.A Wills and Dr. A.A. Shah, whose patient yet important roles in helping me over the last few days for completion of this thesis. I would also present my gratitude to people both staff and student alike, from administration and the departments of chemistry, materials and electronics for their support and advice.

I would like to thank the EDMC workshop technicians Mr. Peter Sellen and Mr. Christopher Williams along with Mr. Lee Mulholland and Mr. Przemyslaw Tryc from "Caplin" Glassblowing Workshop, for their prompt attention to my work requirements over these years at Southampton.

I am indebted to the School of Engineering Sciences, University of Southampton for financial support provided for this research through the RTSG scheme and also immensely thankful for the financial support provided by the technology partners E-ON and C-Tech Innovation Ltd. through the TSB grant TP/4/EET/6/I/2296 for the project of soluble lead-acid and copper-lead dioxide flow batteries.

I am thankful to the people in both my laboratory and office, for their friendship. Always in the forefront to my success in life are my parents whose love and support has made things possible and to whom ***"this thesis is dedicated"***.

List of symbols

Symbol	Description	Quantity	units
a	Constant	5.10	cm
A	Active area of the electrode		cm^2
A_{in}	Inlet/outlet area of the electrodes		cm^2
A_s	Active surface area for reaction		cm^2
b	Constant	5.24	$A\ cm^{-2}$
b_e	Breadth of the electrode	10	cm
c	Concentration of reactant / oxidant		$mol\ dm^{-3}$
c_{H^+}	Concentration of protons		$mol\ dm^{-3}$
$c^0_{H^+}$	Initial concentration of protons	4.2	$mol\ dm^{-3}$
$c^{res}_{H^+}$	Concentration of protons in the reservoir		$mol\ dm^{-3}$
c_{H_2O}	Concentration of water		$mol\ dm^{-3}$
$c^0_{H_2O}$	Initial concentration of water	4.23	$mol\ dm^{-3}$
$c^{res}_{H_2O}$	Concentration of water in the reservoir		$mol\ dm^{-3}$
c_i	Molar concentration of species i = V(II), V(III), V(IV), V(V)		$mol\ dm^{-3}$
c^0_i	Initial concentration of species		$mol\ dm^{-3}$
c^{res}_i	Concentration of species in the reservoir		$mol\ dm^{-3}$
c_O	Concentration of the oxidant		$mol\ dm^{-3}$
c_R	Concentration of the reductant		$mol\ dm^{-3}$
$c_{V(II)}$	Concentration of V(II) species		$mol\ dm^{-3}$
$c_{V(III)}$	Concentration of V(III) species		$mol\ dm^{-3}$
$c_{V(IV)}$	Concentration of V(IV) species		$mol\ dm^{-3}$
$c_{V(V)}$	Concentration of V(V) species		$mol\ dm^{-3}$
$c^0_{V(II)}$	Initial V(II) concentration	0.06	$mol\ dm^{-3}$
$c^0_{V(III)}$	Initial V(III) concentration	1.140	$mol\ dm^{-3}$
$c^0_{V(IV)}$	Initial V(IV) concentation	1.140	$mol\ dm^{-3}$

$c^0_{V(V)}$	Initial V(V) concentration	0.06	mol dm^{-3}
D	diffusion coefficient of the reactant		cm^2 s^{-1}
E^0	Formal potential of the total reaction = $E^0_2 - E^0_1$		V
E^0_1	Formal potential of the reaction at the negative electrode	−0.26	V
E^0_2	Formal potential of the reaction at the positive electrode	1.004	V
E_{-ve}	Negative electrode potential		V
E_{+ve}	Positive electrode potential		V
$E^{0'}_{-ve}$	Standard electrode potential (negative electrode)		V
E_c	Energy stored during charge		Watts or kW
E_{cell}	Cell voltage		V
E^0_{cell}	Open-circuit cell voltage		V
E^e_{cell}	Equilibrium cell voltage		V
E_d	Energy recovered during discharge		Watts or kW
E_{max}	Maximum open-circuit voltage		V
E_{min}	Minimum open-circuit voltage		V
F	Faraday's constant	96485.34	C mol^{-1}
ΔG	Gibbs free energy		Watts or kW
[H$^+$]	Concentration of protons in the electrode		mol dm^{-3}
h_e	height of the electrode	10	cm
I or I_{appl}	Current applied or drawn from the cell		A
I_0	Exchange current		A
$(IR)_e$	Ohmic drop across the solution		V
$(IR)_m$	Ohmic drop across the membrane		V
$(IR)_c$	Ohmic drop across the electrode/plates		V
j_{app}	Applied current density	100	mA cm^{-2}
j_L	Limiting current density		mA cm^{-2}
j_x	Current density at a distance x on the electrode		mA cm^{-2}
K	Constant of proportionality		

k	Reaction rate constant		$\mathrm{m\ s^{-1}}$
k^0	Reaction standard rate constant		$\mathrm{m\ s^{-1}}$
k_1	Reaction rate constants associated with the reactions at positive electrode		$\mathrm{m\ s^{-1}}$
k_2	Reaction rate constants associated with the reactions at negative electrode		$\mathrm{m\ s^{-1}}$
$k_{1,\mathrm{ref}}$	Reference rate constant for positive electrode reaction at 293 K	3.56×10^{-6}	$\mathrm{m\ s^{-1}}$
$k_{2,\mathrm{ref}}$	Reference rate constant for negative electrode reaction at 293 K	3×10^{-9}	$\mathrm{m\ s^{-1}}$
k_o	Rate constant of the oxidation reaction		$\mathrm{m\ s^{-1}}$
k_r	Rate constant of the reduction reaction		$\mathrm{m\ s^{-1}}$
n	Number of electrons		
n_d	Drag-coefficient		
$N_{\mathrm{H_2O}}^{drag}$	Molar flux of the water through the membrane		
$\mathrm{O}^{\dagger}$, O'	Oxidized electroactive species		
Q_c	Charge passed during charge		C
Q_d	Charge passed during discharge		C
R	Molar gas constant	8.314	$\mathrm{J\ K^{-1}\ mol^{-1}}$
$\mathrm{R}^{\dagger}$, R'	Reduced electroactive species		
S	Specific surface area for reaction	420	$\mathrm{m^{-1}}$
t	Time		s
t_c	Time taken to charge		s
t_d	Time taken to discharge		s
t_{fc}	Time taken to fully charge		s
T	Temperature	300	K
T_{ref}	Reference temperature		K
u	Electrolyte flow velocity		$\mathrm{m\ s^{-1}}$
v	Mean electrolyte flow velocity		$\mathrm{cm\ s^{-1}}$
V_e	Volume of the electrode	4×10^{-5}	$\mathrm{m^3}$

V_r	Volume of the reservoir	2.232×10^{-4}	m^3
w_c	Width of the current collector	0.005	m
w_e	Width of the electrode	0.004	m
w_m	Width of the membrane	1.25×10^{-4}	m
x	Distance along the cathode from the high current density end		cm

Greek symbols

Symbol	Description	Quantity	units
α	Transfer coefficient	0.5	
γ_i	Diffusive mass transfer coefficient		
δ	$=V_e/V_r$		
δ_i	Thickness of the boundary		
ε	Porosity of the electrode	0.67	
$\tilde{\varepsilon}$	Constant		
η	Overpotential		V
η_1	Overpotential at the negative electrode		V
η_2	Overpotential at the positive electrode		V
η_a	Activation or charge transfer overpotential		V
η_C	Charge efficiency		
η_{conc}	Mass transport or concentration overpotential		V
η_E	Energy efficiency		
η_{rxn}	Reaction overpotential		V
η_V	Voltage efficiency		
λ	Membrane water content	22	
ν	Kinematic viscosity		$cm^2\ s^{-1}$
ρ_{felt}	Density of the felt		$kg\ m^{-3}$
ρ_{fiber}	Density of the fibre		$kg\ m^{-3}$
σ_c	Electronic conductivity of the graphite current collector	9.1×10^4	$S\ m^{-1}$
σ_e	Ionic conductivity of the electrolyte		$S\ m^{-1}$
σ_m	Conductivity of the membrane	100	$S\ m^{-1}$
τ	Direct measure of residence time of reaction		s
ω	1. Linear flow rate of the electrolyte	1	$cm^3\ s^{-1}$
	2.Angular velocity		$rad\ s^{-1}$

List of Abbreviations

Notation	Abbreviation
2-D	Two dimensional
3-D	Three dimensional
CVD	Chemical vapour deposition
D.C.	Direct current
EDX	Energy dispersive X-ray spectroscopy
HDTMAH	Hexadecyltrimethylammonium hydroxide
MSA	Methanesulfonic acid
OCV	Open-circuit voltage
PCB	Printed circuit board
PEG	Polyethylene glycol
PN	Propionitrile
ppi	Pores per inch
PTFE	Polytetraflouro ethylene
PVDF	Polyvinyldine difluoride
RDE	Rotating disc electrode
RFB / RFBs	Redox flow battery / batteries
RVC	Reticulated vitreous carbon
SCE	Saturated calomel electrode
SEM	Scanning electron microscopy
SHE	Standard hydrogen electrode
SLA	Sealed lead acid battery
SoC	State of charge
VRFB	Vanadium redox flow battery
VRLA	Valve-regulated lead acid battery

Chapter-I

Introduction

1.1. The need for energy storage

Increasing demands for energy are largely being fulfilled by conventional power generation systems. This continued reliance on fossil fuels is potentially damaging the fragile environment. The concerns raised by governments and society over CO_2 emissions from burning fossil fuels[1-3] have led to demands for low-carbon, sustainable energy resourcing[4]. Although renewable energy systems are slowly emerging (still only representing 2% of the total production), little is being done to relieve reliance on traditional power generation methods[2,5,6,7]. A great deal of funding is being invested in research and testing along with the construction of clean energy technologies, especially in solar and wind energy generation systems[8]. In the European Energy Initiative 2007 report[9], wind and solar energy initiatives were given top priority. The expected surge in the use of these renewable energy sources has created new scope for the application of rechargeable secondary battery systems[4, 10-12].

In addition to the efficient storage of energy for future renewable energy installations, secondary rechargeable batteries can be used to store surplus energy from existing generating sources (during off-peak times). This can improve network stability, providing load levelling, reliability and ultimately reduce carbon dioxide emissions[l,13]. Localized usage of batteries at power stations would reduce costs substantially. Surplus power production units which are needed only during peak demand can potentially be decommissioned, with economically run base-load plants operating efficiently at peak times with energy storage systems for additional power requirements[14].

One promising rechargeable battery system is the redox flow battery (RFB). RFBs are a particularly viable choice for large-scale energy storage[15]. The reasons include: simple construction, ease of operation and low maintenance requirements, which makes them more attractive than, other electrochemical energy storage technologies available on the

market, such as nickel-cadmium and sodium-sulfur batteries, which cannot be readily recycled[16-18]. Table 1.1 compares redox flow battery systems to other energy storage systems for large scale-applications. Numerous rechargeable batteries are available and the market for their application is rapidly increasing[10,11,20,21].

Storage system	**Lifetime (Years)**	**Energy density (kWh kg^{-1})**	**% Efficiency**	**Maximum installed capacity (MW)**	**Development status (Large-scale)**	**Reference**
Pumped Hydro	75	0.001	70 – 80	≈ 90,000	Developed	20,23,24, 27
Flow batteries	30	0.03 – 0.8	75 – 85	10 – 12	Developing	20,23,24, 27
Metal-Air batteries	10	0.7	50	0.006	Developing	2,5,20,23,24,27
Stationary lead-Acid batteries	13	0.04	75	1.2	Developed	2,5,24,27
Super capacitors	15	0.02	93 – 98	0.005 – 0.1	Developing	2,5,24,27
Fly wheels	20	0.2	90 – 95	≈ 1	Developed	2,5,24,27

Table1.1: A simple comparison table of flow batteries with other large-scale energy storage systems.

1.2. The Flow battery

An RFB is a secondary (rechargeable) battery system that functions as an electrochemical energy conversion device for energy storage. RFBs convert chemical energy into electrical energy by reduction and oxidation of electroactive species dissolved in an electrolyte that flows between a storage tank and an electrochemical cell. The positively and negatively charged electrolyte solutions containing the redox couples are circulated through the electrode compartments via large capacity electrolyte storage tanks external to the electrochemical cell. In the electrochemical cell, the two electrolytes are usually (but not always) separated by an ion exchange membrane[15,22], as shown in Fig 1.1 below:

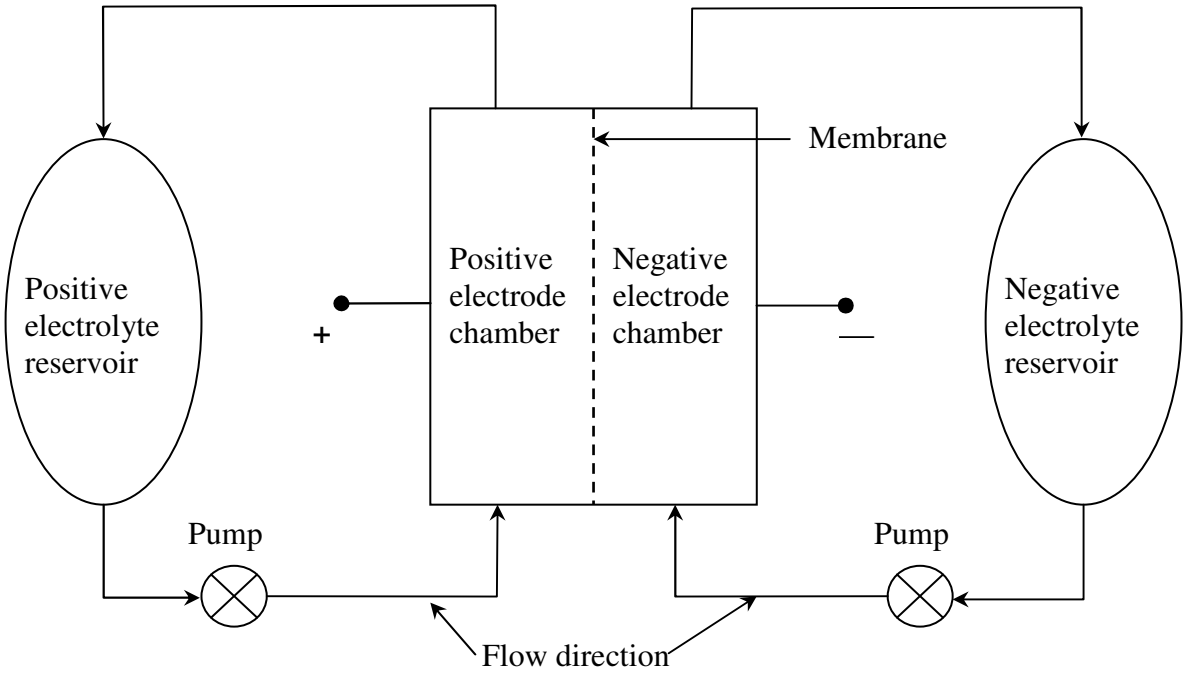

Fig 1.1: A schematic representation of a redox flow battery system.

The energy storage capacity can be increased with the volume of the reservoirs and the concentrations of electroactive species, while the power output by the active electrode surface area and number of cells (when placed in a stack). Fig. 1.2 shows an example of a bipolar stack assembly. This cell construction has positive and negative current-collecting plates at each end and bipolar plates for each of the middle cells. The positive electrolyte is passed on one side of the bipolar plate and the negative electrolyte through on the other side. Bipolar plate arrangement increase both the capacity and power with minimal increments in the available industrial space and pumping capacity[13,16].

RFBs find particular applications in stand-alone renewable energy systems, such as wind turbines, photovoltaic units and tidal power systems[25,26]. Other applications include distributed generation systems and improvement of power quality[27], as well as frequency/voltage control.

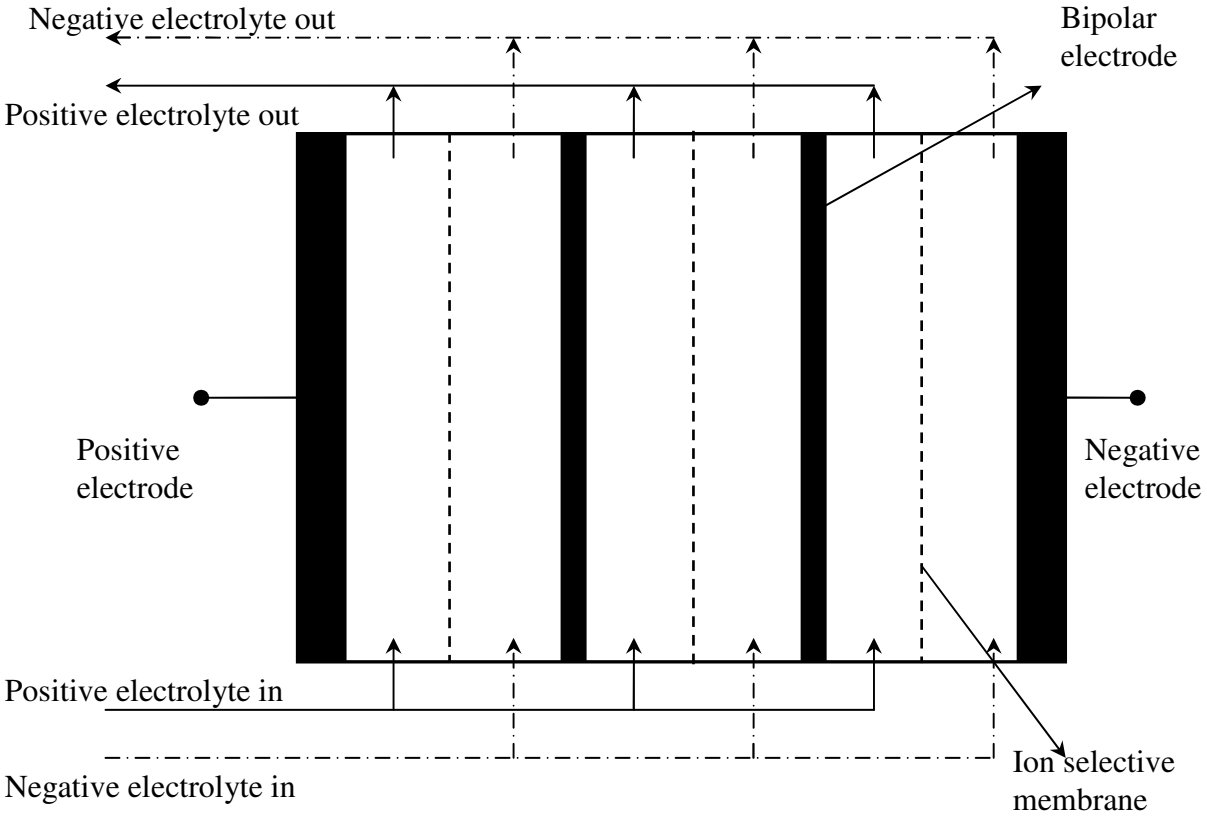

Fig 1.2: A schematic representation of a bipolar cell stack containing three cells.

Various RFB systems[28] have been developed[22,29], including the iron-chromium[53], bromine polysulfide[5,15,16,22,29,41], all-vanadium[22,30,31,40,52], vanadium-bromine[16,22,31,45,55], zinc-bromine[22,29,32,54], zinc-cerium[16,20,22,33,56] and soluble lead acid cells[13,14,16,22,30,34] (including valve-regulated lead acid (VRLA) and sealed lead acid (SLA)). Some of these will be discussed in more detailed in section 1.3.3. The following sections explain the various constructional characteristics of redox flow cell systems.

1.3. Types of redox flow batteries

The electrochemical cell is the main part of the RFB system. It consists of positive and negative electrodes in a parallel plate arrangement. The two electrodes parallel to each other are usually divided by a membrane, which can be cationic or anionic, although some systems operate even without a membrane. Fig 1.3 shows a simplified classical redox flow cell where the species $O^{\dagger}$ and O' are oxidized and reduced to $R^{\dagger}$ and R', respectively

(where *n* is the number of electrons), corresponding to the negative and positive electrode reactions during charge and discharge as shown in reactions (1) and (2)

$$O' + ne^- \underset{\text{discharge}}{\overset{\text{charge}}{\rightleftharpoons}} R' \quad (1)$$

$$R^\dagger + ne^- \underset{\text{discharge}}{\overset{\text{charge}}{\rightleftharpoons}} O^\dagger \quad (2)$$

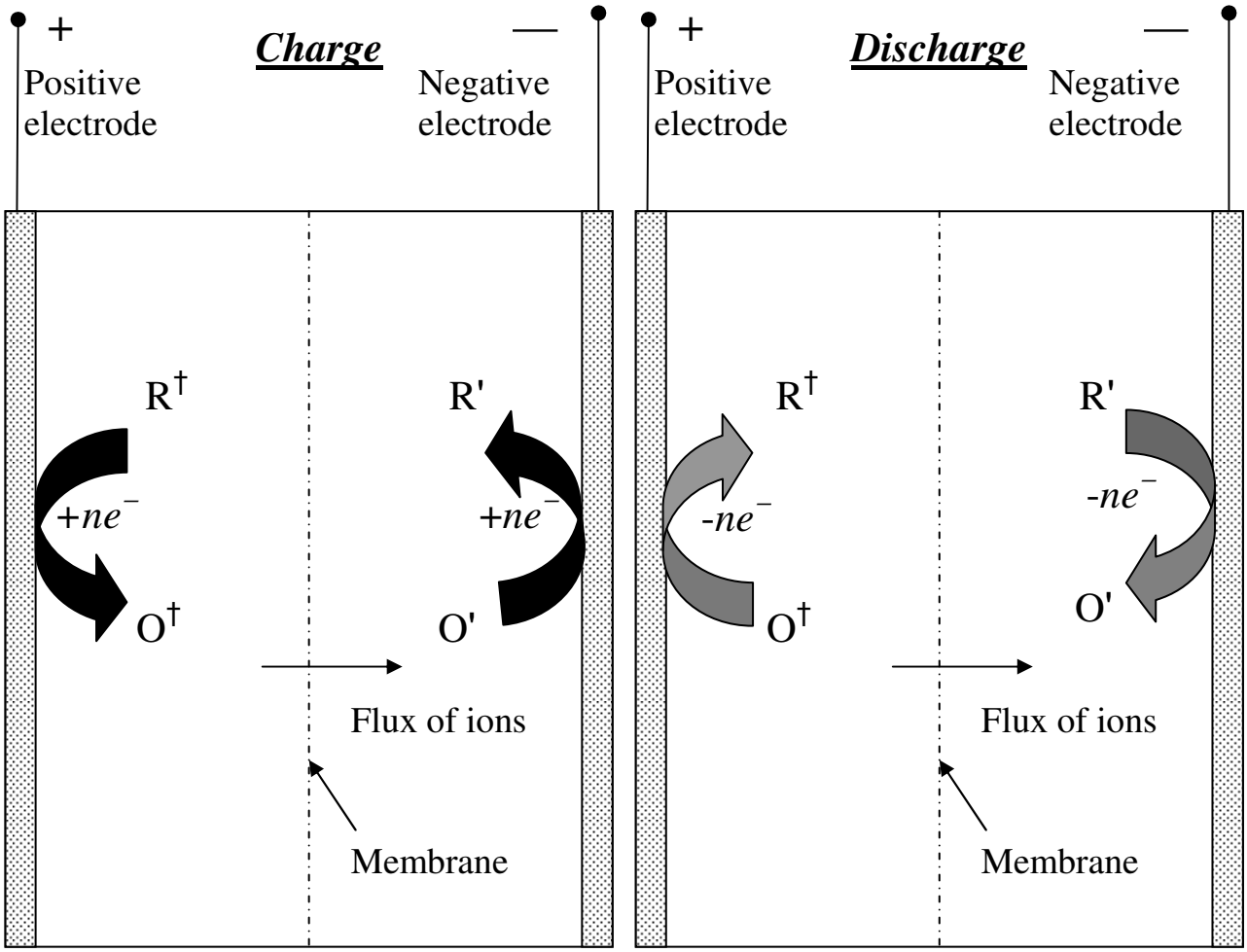

Fig 1.3: Schematic of a classical redox flow battery.

1.3.1. Categorisation

Redox flow batteries can be categorised in many ways depending on the type of cell construction, operational phase of electroactive species and the mode of charge storage[16,22,23,32]. Some types and examples are:

(1) two soluble liquid phases species i.e. liquid / liquid phase (all-vanadium, vanadium-bromine or vanadium/polyhalide)

(2) a liquid / solid phase (lead-lead dioxide, copper-lead dioxide)

(3) a liquid / gaseous phase (zinc-air, aluminium-air) and

(4) a combination of liquid / solid and liquid / liquid phase (zinc-cerium)

These selections are usually made after consideration of the standard redox potential of each individual redox couple in order to obtain a maximum cell voltage, which can be estimated from the redox potentials (*vs.* standard hydrogen electrode (SHE) at 25 ºC) available, e.g. Fig 1.4.

The classification depending on the cell configuration can be simplified into two types, namely divided and undivided cells. Each has its own advantages and disadvantages, as shown below.

(a). Divided cell. In this configuration each cell in the flow battery has two channels; one containing the positive electrolyte and one containing the negative electrolyte. The membrane that divides the two electrodes can be cationic or anionic and helps to avoid mixing of the two different electrolytes in the cell as well as to maintain balanced chemistry between the two compartments [44]. This type of construction requires two reservoirs and two electrolyte circuits, which usually increases the cell cost and complicates the cell design. The all-vanadium and zinc-bromine systems, which have been successfully tested and scaled-up, are two examples of divided cell systems. The all-vanadium system provides high efficiency along with a one-off capital cost, whilst the zinc-bromine system has a high energy density. However, both have problems associated with stability, electrolyte cross-over (cross contamination) and membrane costs.

(b). Undivided cell. This type of cell offers simple design and is associated with lower construction costs[20]. The cell consists of two parallel-plate electrodes forming a

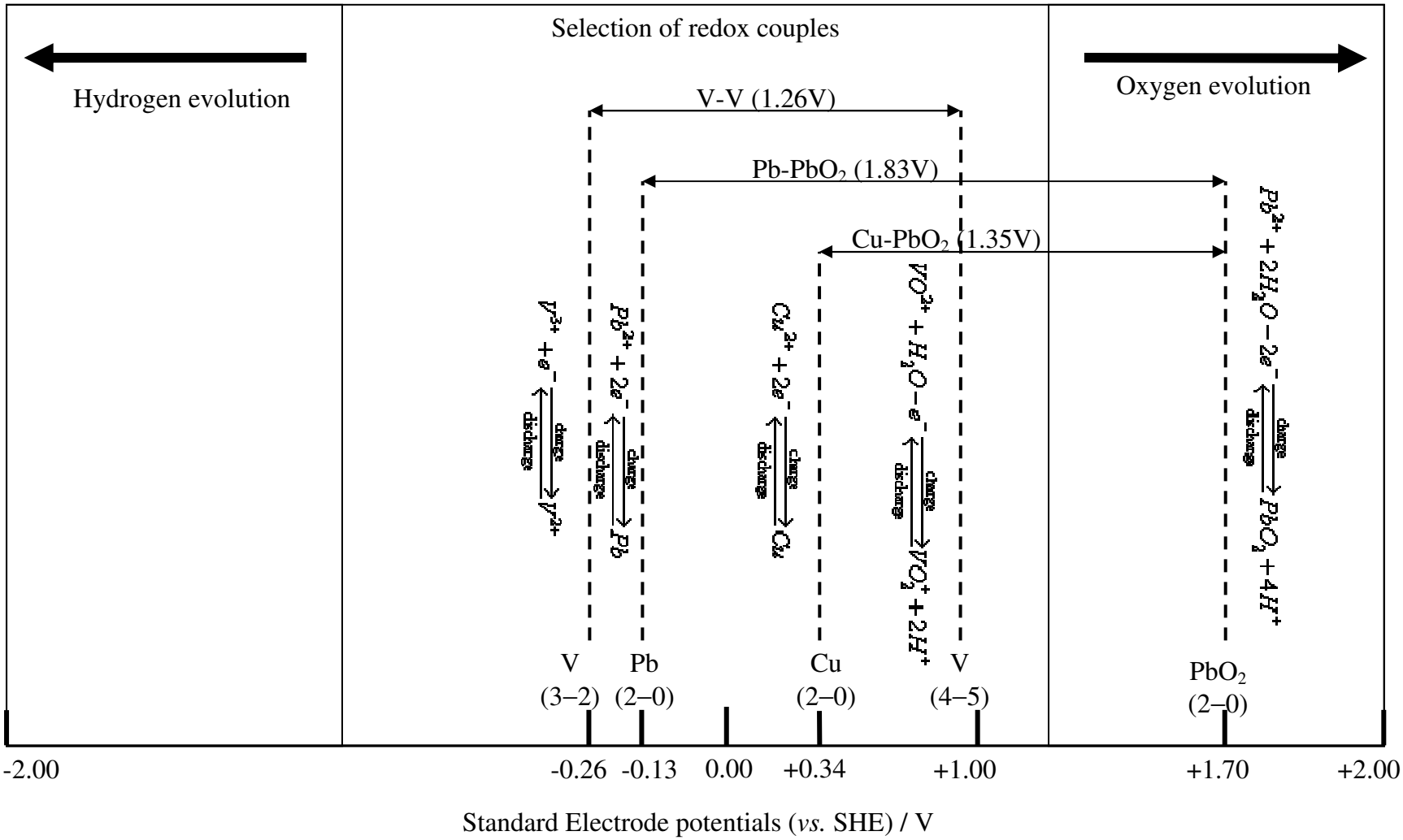

Fig 1.4: Chart showing the standard potentials of redox couples (with the transition of oxidation states indicated) discussed in this thesis[17,59,60]

single flow-by compartment in the middle. Examples of undivided cells include the zinc-nickel flow battery[35] and the soluble-lead acid flow battery[36-38]. The absence of a membrane also necessitates careful selection of the redox couples to avoid self-discharging reactions.

RFBs can also be classified in terms of the specific mode of electrochemical charge storage:

- Stored in the electrolyte as reduced / oxidised species *e.g.*, all-vanadium flow battery.
- Stored in the phase on the electrode surface. This can be in the form of a deposit, *e.g.*, soluble lead-acid battery.
- A combination of the first two cases, *e.g.*, zinc-cerium or zinc-bromine flow batteries.

The first case is a classical example of a *redox flow battery* (RFB), where the energy of the battery is related to the size of the electrolyte tanks. The latter two cases are know as *hybrid flow batteries*, where the energy of the battery is dependent on the amount of the electroactive species retained within the flow cell rather than the tank[79].

1.3.2. Electrodes

A typical unit contains two electrodes. The unit cells can be combined using bipolar electrodes to construct stacks as shown in Fig 1.2. The electrodes should be highly conductive. Issues of metal corrosion, alloy purity, along with the economic factors have led to research into low-cost electrode materials. Hence in this thesis different low cost carbon material such as felts, foams, fibres and composites, have been investigated and utilised. What follows is a brief description of these materials and their most important characteristics.

(a) Carbon felt

This material forms a flexible 3-D electrode structure with a network of carbon fibers woven or bundled together. They are normally produced by thermal degradation with subsequent carbonization both from natural (e.g. sheep's wool) or polyvinyl substrates[39]. Felts are usually very porous and well suited for flow-through design electrodes[40]. The porosity can be calculated using equation (3) below[41]:

$$\varepsilon = \left(\frac{\rho_{fiber} - \rho_{felt}}{\rho_{fiber}} \right) \tag{3}$$

where, ρ_{fiber} is the density of the fibre and ρ_{felt} is the density of the felt.

Felts also tend to withstand high stress (compressed up to 90 % in volume) and typically possess a high specific surface area (GFA5 type: 171 $cm^2\ cm^{-3}$)[39,41,42]. Fig 1.5 shows a scanning electron microscopic (SEM) image of this material, with the network of micro fibres. Fig 1.5 (a) and a close-up image of a carbon fibre Fig 1.5 (b) strand with its width (7.26 μm) indicated. The carbon fibres shown are non-aligned and are loosely packed.

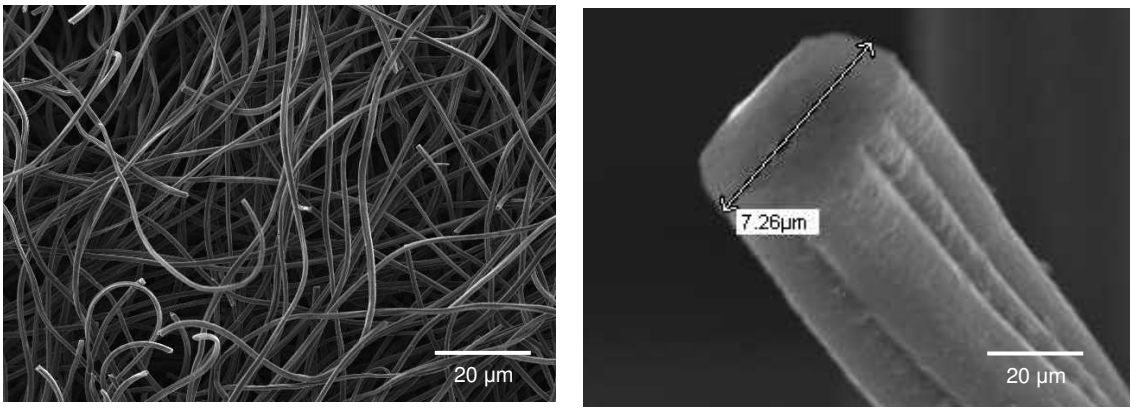

(a) (b)

Fig 1.5: (a) SEM image of the carbon felt surface (b) SEM image of a single fibre in the felt.

Felts are also used in the production of other carbonaceous substances such as carbon cloths[43,44] and carbon whiskers on composite electrodes[39]. They are also used to produce carbon reinforced composites with a high tensile strength (100–300 kg mm^{-2}), which is greater than some metallic materials and their alloys[39].

(b). Carbon foam

Carbon foam, also called Reticulated Vitreous Carbon (RVC), has a 3D porous skeletal structure. Unlike carbon felt, it is not compressible but has a greater void volume (90–97 %). A higher porosity lead to a greater specific surface area of the foam, ranging from 12 cm^2 cm^{-3}-for 10 ppi, up to $\cong 66$ cm^2 cm^{-3} for 100 ppi[45,46]. The skeletal structure is completely made up of vitreous carbon, which is obtained by the polymerisation of a resin combined with a foaming agent. This is followed by carbonisation, resulting in glassy porous carbon foam. Polyureatheane and phenolic resins are commonly used; which have a carbon yield between 3 and 50 %. Carbon foams can also be used for their ability to resist high temperatures in non-oxidizing environments[45,47].

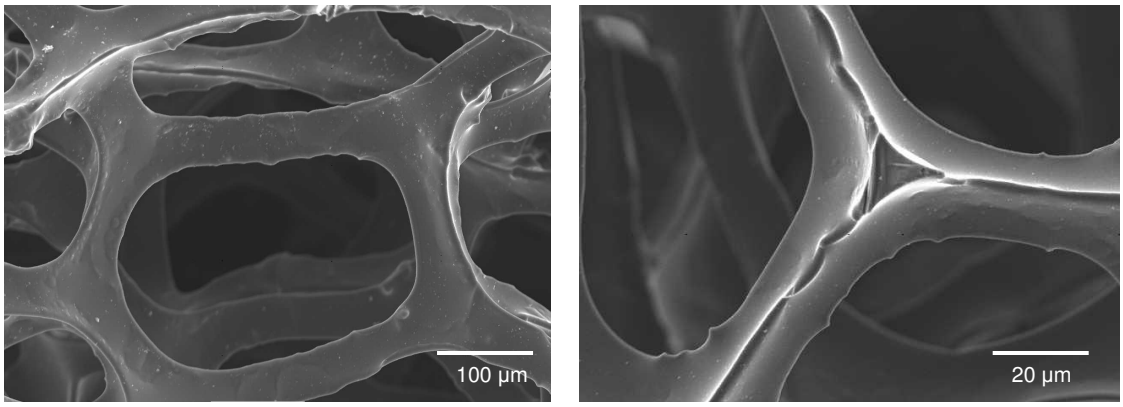

(a) (b)

Fig 1.6: (a) SEM image of the carbon foam surface (b) SEM image of the strut joint from a 1 cm^2 carbon foam cube sample of 80 ppi.

RVC is much lighter compared to other carbon materials due to its low carbon content. It also has a high electrical conductivity (0.035 to 5.64 S m^{-1})[45]. The lack of compressibility is due to the formation of rigid struts, can be seen in Fig 1.6, which shows the SEM images of (a) structural voids and (b) the detailed struts of the RVC. Fig 1.6 also reveals a honeycomb structure. The interconnections are similar to triangular struts, which form an hexagonal shape creating a void in the middle.

(c) Carbon composite electrodes

Carbon composite electrodes are widely used in electrochemical applications due to their controllable electrochemical properties and low cost. Carbon composites are formed with carbon and a non-conducting binder mixed accordingly (allowed to cure to a shape and size defined by the mould used). Many types of carbon materials can be used in composite manufacturing, including particulate forms of carbon fibres, foam, nanotubes or felts and graphite. These electrodes tend to have all or some of the combined properties of the individual substrates of carbon material used in the composites and the binders. The active surface layers can be prepared using various surface modification techniques like chemical vapour deposition (CVD)[48], doping[45] or heat treatment[42,43], with the addition of chemicals (e.g. MnO_2, Li, Ni, Co, Fe) and dopants (e.g. diamond or boron). The electrodes produced by these methods usually have a 3-D activated surface and a carbon composite base layer.

Carbon composites can also form as 2-D (non macro porous) electrodes. Two commercial composite carbon electrodes used extensively as electrode materials in this report were Entegris® (polyvinyl-ester composite) and ®SIGRACET (SGL Group Ltd.) Polyvinyldine difluoride (PVDF). These are manufactured using expanded graphite and by the process of bulk moulding at temperatures of 180–250 °C under high pressure (> 40 M Pa). They are also highly conductive (70 S cm^{-1})[51]. Of these electrodes, Entegris carbon has the highest

flexural strength 57 N mm^{-2}, compared with 40 N mm^{-2} for SGL carbon. However, repeated manual cleaning or regular occurrence of gas evolutions (side reactions) could degrade the electrode surface causing it to either crack or become soft and powdery. This effect will be described in detail in the soluble-lead-acid battery section (Chapter 3).

1.3.3. Examples of Redox Flow Batteries

Various redox couples are considered for application in RFBs. This thesis investigates three RFBs; specifically, the all-vanadium, the soluble-lead acid and the copper-lead dioxide flow batteries. Table 1.2 compares these cells and other battery systems. The electrode reactions (with electrode potentials *vs.* SHE) and a brief description of the RFBs are given below.

- **All-vanadium battery**[16,22,31,40,52]. This battery system is one of the most widely developed and uses vanadium ions in their four oxidation states. The cell is divided by a proton exchange membrane (typically Nafion®). Carbon or graphite felt is utilised as the electrode material for both the positive and negative electrodes. The vanadium ions are highly soluble (1-2 mol dm^{-3}) in the sulfuric acid (H_2SO_4) electrolyte (2-4 mol dm^{-3}). The electrochemical reactions of the positive and negative electrodes are:

$$VO^{2+} + H_2O - e^- \underset{\text{discharge}}{\overset{\text{charge}}{\rightleftharpoons}} VO_2^+ + 2H^+ \qquad E^0 = +1.00\ V\ vs.\ \text{SHE} \tag{4}$$

$$V^{3+} + e^- \underset{\text{discharge}}{\overset{\text{charge}}{\rightleftharpoons}} V^{2+} \qquad E^0 = -0.26\ V\ vs.\ \text{SHE} \tag{5}$$

Due to the use of the same element (i.e. vanadium) in both the half-cells, problems of cross-contamination are avoided. The system is highly efficient ($\cong 90$ %) and can be used for large-scale energy storage. This battery is not damaged by fluctuating power requirements or deep discharge cycles.

Type of redox flow battery/system	Electrode reactions	Electrode material	Membrane	Cell voltage (V *vs.* SHE)	Current density (A m^{-3})	Operating temperature (°C)	% Energy efficiency	References
Bromine / poly sulphide	+ ve: $3Br^- \underset{\text{discharge}}{\overset{\text{charge}}{\rightleftharpoons}} Br_3^- + 2e^-$ − ve: $S_4^{2-} + 2e^- \underset{\text{discharge}}{\overset{\text{charge}}{\rightleftharpoons}} 2S_2^{2-}$	Carbon polymer composite	Cationic membrane	1.54	600	35	67	5, 15, 16, 22, 41
All-Vanadium	+ ve: $VO^{2+} + H_2O - e^- \underset{\text{discharge}}{\overset{\text{charge}}{\rightleftharpoons}} VO_2^+ + 2H^+$ − ve: $V^{3+} + e^- \underset{\text{discharge}}{\overset{\text{charge}}{\rightleftharpoons}} V^{2+}$	Graphite felt	Nafion® 117	1.26	800	35–55	< 80	16, 22, 31, 40, 52
Zn-Bromine	+ ve: $3Br^- \underset{\text{discharge}}{\overset{\text{charge}}{\rightleftharpoons}} Br_3^- + 2e^-$ − ve: $Zn^{2+} + 2e^- \underset{\text{discharge}}{\overset{\text{charge}}{\rightleftharpoons}} Zn$	Carbon polymer composite	Porous or ionic separator	1.82	15–200	30–50	40–93	16, 22, 32, 29, 54
Vanadium-bromine	+ ve: $2Br^- + Cl^- \underset{\text{discharge}}{\overset{\text{charge}}{\rightleftharpoons}} ClBr_2^- + 2e^-$ − ve: $VBr_3 + e^- \underset{\text{discharge}}{\overset{\text{charge}}{\rightleftharpoons}} VBr_2 + Br^-$	Graphite felt	Nafion® 112	1.3	600	30–50	< 90	16, 22, 31,55
Soluble-lead acid	+ ve: $Pb^{2+} + 2H_2O - 2e^- \underset{\text{discharge}}{\overset{\text{charge}}{\rightleftharpoons}} PbO_2 + 4H^+$ − ve: $Pb^{2+} + 2e^- \underset{\text{discharge}}{\overset{\text{charge}}{\rightleftharpoons}} Pb$	Carbon polymer composite	No membrane	1.8	100–600	0–30	< 70	13, 14, 16, 22, 34
Zinc-cerium	+ ve: $2Ce^{3+} \underset{\text{discharge}}{\overset{\text{charge}}{\rightleftharpoons}} 2Ce^{4+} + 2e^-$ − ve: $Zn^{2+} + 2e^- \underset{\text{discharge}}{\overset{\text{charge}}{\rightleftharpoons}} Zn$	Zn: Carbon polymer Ce: Platinised titanium	Nafion® 117	2.5(charge) 2 (discharge)	5000	30–50	70–75	16, 20, 56,
Copper-lead dioxide	+ ve: $Pb^{2+} + 2H_2O - 2e^- \underset{\text{discharge}}{\overset{\text{charge}}{\rightleftharpoons}} PbO_2 + 4H^+$ − ve: $Cu^{2+} + 2e^- \underset{\text{discharge}}{\overset{\text{charge}}{\rightleftharpoons}} Cu$	Carbon polymer composite	No membrane	1.3	100–300	20–35	< 70	37

Table 1.2: Comparison of various redox flow battery systems.

The high capital cost of the vanadium based electrolyte and limited life-time of the membrane are the two main limitations of this battery.

- **Soluble-lead acid battery**[13,14,16,22,34]. This battery has been developed recently. The electrolyte contains lead (II) (1-2 mol dm^{-3}) in aqueous methanesulfonic acid (MSA). This acid is more environmentally friendly and less oxidising than H_2SO_4[57]. The system is undivided with the advantage of a lower capital cost compared to that of the vanadium system. Carbon-composite based electrode materials (Entegris or PVDF carbons) are generally used. The electrochemical reactions of the positive and negative electrodes with their respective electrode potentials are:

$$Pb^{2+} + 2H_2O - 2e^- \underset{\text{discharge}}{\overset{\text{charge}}{\rightleftharpoons}} PbO_2 + 4H^+ \qquad E^0 = +1.70\ V\ vs.\ \text{SHE} \qquad (6)$$

$$Pb^{2+} + 2e^- \underset{\text{discharge}}{\overset{\text{charge}}{\rightleftharpoons}} Pb \qquad E^0 = -0.13\ V\ vs.\ \text{SHE} \qquad (7)$$

This RFB system employs the inter-conversion of solid and solution phases at both electrodes. It has a good charge efficiency ($\cong 85$ %) and a voltage efficiency in the range of 60–70 %. Additives for the control of electrodeposit morphologies are required during operation.

- ***Copper-Lead dioxide battery***[37]. This RFB is first described and characterised in this thesis. The electrolyte is a combination of copper(II) and lead(II) (1–2 mol dm^{-3}) in methanesulfonic acid (1–2 mol dm^{-3}). This flow battery also utilises carbon composite electrodes. The cell is similar to the soluble-lead acid cell; both are undivided and involve the inter conversion of solid electrodeposits and soluble solution species. The positive and negative electrode reactions and their respective electrode potentials are:

$$Pb^{2+} + 2H_2O - 2e^- \underset{\text{discharge}}{\overset{\text{charge}}{\rightleftharpoons}} PbO_2 + 4H^+ \qquad E^0 = +1.70\ V\ vs.\ \text{SHE} \qquad (8)$$

$$Cu^{2+} + 2e^- \underset{\text{discharge}}{\overset{\text{charge}}{\rightleftharpoons}} Cu \qquad E^0 = +0.34\ V\ vs.\ \text{SHE} \qquad (9)$$

The charge efficiency is high (80-90 %) and a voltage efficiency of ≅ 60 % can be achieved. Additives are required for an improved morphology of the PbO_2 electrodeposits and long-term cycling of the battery.

- **Bromine/polysulfide battery**[5,15,16,22,41]. This system is based on the positive and negative electrolytic reactions as shown in (10) and (11). The open-circuit potential is around 1.5 V. The positive and negative electrolytes consist of sodium bromide (NaBr) and sodium polysulfide (Na_2S_n, where n= 4,), respectively, which are highly soluble in aqueous media. The system utilizes carbon composite materials for the positive electrode and nickel foam for the negative electrode. A cation selective membrane is used to prevent the sulfur anions from reacting with bromine. Cross-contamination and electrolyte balance are two key issues, along with preventing sulfur deposition during operation. The electrochemical reactions of the positive and negative electrodes with their respective electrode potentials are:

$$3Br^- \underset{\text{discharge}}{\overset{\text{charge}}{\rightleftharpoons}} Br_3^- + 2e^- \qquad E^0 = +1.09\ V\ vs.\ \text{SHE} \qquad (10)$$

$$S_4^{2-} + 2e^- \underset{\text{discharge}}{\overset{\text{charge}}{\rightleftharpoons}} 2S_2^{2-} \qquad E^0 = -0.51\ V\ vs.\ \text{SHE} \qquad (11)$$

- **Zinc-Bromine battery**[16,22,29,32,54]. This combination of redox couples results in higher theoretical cell voltage than that of the bromine-polysulfide system, with the positive and negative electrode reactions as shown in reactions (12) and (13) below. Although fundamental studies are usually based on a platinum foil for bromine

production, the typical electrode substrate used in these batteries is a carbon-polymer composite.

$$3Br^- \underset{\text{discharge}}{\overset{\text{charge}}{\rightleftharpoons}} Br_3^- + 2e^- \qquad E^0 = +1.09\ V\ vs.\ \text{SHE} \tag{12}$$

$$Zn^{2+} + 2e^- \underset{\text{discharge}}{\overset{\text{charge}}{\rightleftharpoons}} Zn \qquad E^0 = -0.76\ V\ vs.\ \text{SHE} \tag{13}$$

This combination also requires the presence of a membrane to separate bromine from the zinc half-cell compartment; otherwise, the overall efficiency reduces due to the reaction of bromine with the metallic zinc deposited on the electrode. This system also requires additives of quaternary ammonium salts or propionitrile (PN) for the formation of complexes with bromine, which help to reduce self-discharge and the vapour pressure of bromine. Additives can improve the overall energy efficiency to $\cong 90\ \%$[32].

- **Vanadium-Bromine battery**[16,22,31,55]. The vanadium-bromine battery is in some respects an improvement on the all-vanadium flow battery for vehicular applications[22]. It utilises carbon or graphite felt bonded onto conductive plastic sheets as electrodes. The species of vanadium are still highly soluble (2 mol dm^{-3}) and stable in sulphuric acid. The electrochemical reactions of the positive and negative electrodes with their respective electrode potentials are:

$$2Br^- + Cl^- \underset{\text{discharge}}{\overset{\text{charge}}{\rightleftharpoons}} ClBr_2^- + 2e^- \qquad E^0 = +1.05\ V\ vs.\ \text{SHE} \tag{14}$$

$$VBr_3 + e^- \underset{\text{discharge}}{\overset{\text{charge}}{\rightleftharpoons}} VBr_2 + Br^- \qquad E^0 = -0.25\ V\ vs.\ \text{SHE} \tag{15}$$

Further improvements have been made using the vanadium/polyhalide couple[57], in combination with graphite felt electrodes. Both of these systems use a Nafion® membrane to divide the positive and negative electrode compartments, and can attain high cell voltages of ≅ 1.3 V and charge efficiencies of > 95 %.

- **Zinc-Cerium battery**[16,20,22,56]. This system developed by Plurion systems Inc., is similar to the zinc-bromine system. It has an open-circuit voltage ≅ 2.5 V (during charge) and uses a Nafion® membrane. MSA based electrolytes are usually used. A platinised titanium mesh for the positive electrode and a carbon composite electrode for the negative can be used in the flow cell. The cell has the disadvantage of possible cross-contamination due to the presence of two different electrolytic species. The electrochemical reactions of the positive and negative electrodes with their respective electrode potentials are:

$$2Ce^{3+} \underset{\text{discharge}}{\overset{\text{charge}}{\rightleftharpoons}} 2Ce^{4+} + 2e^{-} \qquad E^0 = +1.44\ V\ vs.\ \text{SHE} \tag{16}$$

$$Zn^{2+} + 2e^{-} \underset{\text{discharge}}{\overset{\text{charge}}{\rightleftharpoons}} Zn \qquad E^0 = -0.76\ V\ vs.\ \text{SHE} \tag{17}$$

1.3.4. Figures of merit

The performance of a redox flow battery system can be measured in terms of current density, cell voltage, the energy/power densities and the voltage, charge and energy efficiencies. In this thesis, voltage efficiency values required for the calculation of the figures of merit have been evaluated using average values for each charge and discharge cycle. The determination of these figures of merit is important for characterising the performance of the flow battery, the rate of reactant conversion, and the design factors affecting the performance during operation. The efficiencies are defined below.

The ***voltage efficiency*** measures the ratio of the instantaneous cell voltage between discharge and charge and can be defined as:

$$\eta_V = \left(\frac{\left(\frac{1}{t_d - t_c} \right) \int_{t_c}^{t_d} E_{cell} \cdot dt}{\left(\frac{1}{t_c} \right) \int_{0}^{t_c} E_{cell} \cdot dt} \right) \tag{18}$$

where E_{cell} is the cell voltage and t_d and t_c are the times taken to discharge and charge, respectively.

The ***charge efficiency*** is the ratio between the number of coulombs used during discharge divided by the number of coulombs required to charge the system. The following equation gives this relationship:

$$\eta_C = \left(\frac{Q_d}{Q_c} \right) = \left(\frac{\int_{t_c}^{t_d} I \cdot dt}{\int_{0}^{t_c} I \cdot dt} \right) \tag{19}$$

where, Q_d and Q_c are the charges passed during discharge and charge, respectively and I is the current drawn or applied to the cell.

The ***energy efficiency*** is the ratio of the energy between the discharge and charge periods. It can be expressed as follows:

$$\eta_E = \left(\frac{E_d}{E_c} \right) = \eta_V \cdot \eta_C \tag{20}$$

where, E_d and E_c are the energy recovered and stored during discharge and charge, respectively[22].

1.4. Scope of this thesis

In this thesis, fundamental studies of two emerging RFB technologies (the all-vanadium, and the soluble lead-acid RFBs) and a new system (the copper-lead dioxide RFB) are performed. Each electrolyte is characterised by cyclic voltammetry and then used in the test cells to generate charge–discharge cycles. This includes a brief description of the thermodynamics, electrode kinetics and governing equations for the appropriate calculations required to analyse the systems. The vanadium system normally uses sulfuric H_2SO_4 due to its high solubility for vanadium (up to 2 mol dm^{-3}), while the other two systems use MSA[57].

MSA has been used extensively due to its more environmentally-friendly and less oxidising nature compared to H_2SO_4. Another reason is that lead and copper salts are highly soluble in this acid (up to 2 mol dm^{-3})[58]. The solubility levels of the redox active species determine the capacity of the flow cell and therefore high concentration solutions are desirable. The solubility of lead in MSA has been calculated previously and found to steadily decrease with the an increase in the concentration of free acid (1–8 mol dm^{-3})[13,57,58].

The all-vanadium system is at a stage of extensive scale-up testing for a range of applications. It has high charge ($\cong 95$ %) and energy efficiencies ($\cong 85$ %), when compared to other technologies. "***Chapter II: The All-Vanadium flow battery***" provides an investigation of the electrochemistry of vanadium in a H_2SO_4 electrolyte. A 100 cm^2 custom-made test cell was used to carry out investigations of the vanadium system providing performance data as a function of concentration, flow rate, current density and

temperature. The results were used to calculate figures of merit for a constant as well as a variable state of charge (SoC). A control-oriented mathematical model for the calculation of the cell voltage of the flow battery was also developed. The results were analysed accordingly and discussed in comparison with other flow battery systems.

The soluble lead-acid has good charge efficiency ($\cong 85$ %), whilst the voltage efficiency oscillates between 60 and 80 %. By virtue of its simple construction and ease of assembly in a laboratory environment, this cell was selected for further study in this thesis. "***Chapter III: The Soluble lead-acid flow battery***" introduces the electrochemistry of the lead and lead dioxide redox couples, and the operation of the soluble lead-acid flow battery in MSA electrolyte is investigated. The performance with various electrode materials and electrolyte compositions under extensive (≥ 150) cycling of the flow battery is considered. The results are analysed, and a comparison to the all-vanadium flow battery is provided.

A new combination of redox couples demonstrated proof-of-concept operation of a Cu-PbO_2 flow battery. It has a high charge efficiency ($\cong 90$ %), similar to that of a vanadium system, and reasonable voltage efficiency ($\cong 65\%$). Due to the cheaper sourcing of the electrolyte, the nominal use of additives and compatibility with the soluble-lead acid test system, this combination was considered for testing in a flow cell. "***Chapter IV: The copper-leaddioxide flow battery*****"** introduces a study of this novel RFB, including initial electrokinetic studies of the electrolyte and the charge-discharge characteristics on a 100 cm^2 cell test-rig, along with effects of additives. The results are compared with those of the previous two flow battery systems.

1.4.1: Methodology

(a) Cell potential

An electrode material in contact with an electrolyte solution will develop a potential, characterised by the composition of the electrolyte and the characteristics of the electrode material. This electrode potential can be measured with respect to a reference electrode. Two conducting materials immersed in an electrolytic medium would have a potential difference and can form an electrochemical cell. The potential difference of the total cell (E_{cell}) can be written as the difference between the electrode potential on the positive (E_{+ve}) and negative (E_{-ve}) half cells as in equation below[59] :

$$E_{cell} = E_{-ve} - E_{+ve} \tag{21}$$

If a spontaneous reaction occurs upon connection to an external conducting circuit, the cell is called a galvanic cell[59]. If the occurrence of reaction requires an external power source with a voltage higher than that of the open-circuit voltage of the cell, it is an electrolytic cell[59]. Flow batteries operate as electrolytic cells (during charge) and galvanic cells (during discharge).

In the simplest case, the electrode reactions can be described by the following simple electron transfer reaction:

$$O' + ne^- \underset{k_o}{\overset{k_r}{\rightleftharpoons}} R' \tag{22}$$

where O' is the oxidant, R' is the reductant, n is the number of electrons involved in the reaction, and k_r and k_o are the rate constants for the reduction and oxidation reactions at the electrode, respectively.

The energy dissipated by the reaction can be expressed as the Gibbs free energy (ΔG):

$$\left|\Delta G\right| = nF\left|E_{cell}\right| \tag{23}$$

where n is the number of electrons transferred and F is Faraday's constant.

The relation between the electrode potential (E_{-ve} or E_{+ve}) and the concentrations of the participants in the reaction (22) can be approximated by the Nernst equation[59]. This equation is normally written in terms of reactant activities, which in some instances can be approximated by the concentrations[59] as to give (example negative electrode):

$$E_{-ve} = E_{-ve}^{0'} + \frac{RT}{nF}\ln\left(\frac{c_O}{c_R}\right) \tag{24}$$

where E_{-ve} is the electrode potential, $E_{-ve}^{0'}$ is the standard potential of the redox couple, R is the molar gas constant, T is the temperature and c_O and c_R are the concentrations of O and R, respectively.

From the above equation (24), the equilibrium potentials of the individual positive (E_{+ve}^{e}) and negative (E_{-ve}^{e}) electrodes can be calculated theoretically, and the difference between these two potentials is known as the equilibrium cell potential or cell voltage (E_{cell}^{e}):

$$E_{cell}^{e} = E_{-ve}^{e} - E_{+ve}^{e} \tag{25}$$

The deviation of this potential difference from equilibrium upon the application of a current is known as polarization, which can be quantified measured by the overpotential η as follows:

$$\eta = E_{cell} - E^{e}_{cell} \tag{26}$$

The electrode reaction (22) is hindered by a number of steps or processes. Inefficiencies arise from barriers to electron and ion transfer, mass-transport resistances and side reactions or other surface reactions, as indicated in Fig 1.7. Each of these resistances are apparent in distinct regions of the current–voltage curve. Under steady state conditions, the reaction rates of the processes are the same, but one or more steps limits or controls the reaction. This limiting process is called the rate-determining step.

The need to apply an overpotential (η) is to overcome the ohmic drops across the solution ($(IR)_e$), membrane ($(IR)_m$) and electrode/plates ($(IR)_c$). The ohmic drop across the solution can be reduced by appropriate cell design, careful choice of the solution composition and by reducing the inter-electrode gap between the two electrodes. The total cell voltage (E_{cell}) can be given as[60]:

$$E_{cell} = E^{e}_{cell} - |\eta_1| - |\eta_2| - |(IR)_e| - |(IR)_m| - |(IR)_c| \tag{27}$$

where, η_1 and η_2 are the overpotentials at the negative and positive electrodes.

The negative and positive electrode overpotentials are each a combination of two main overpotentials associated with the electrode reactions[59]:

- ***Activation or charge transfer overpotential*** (η_a) occurs when the electron transfer process becomes the rate determining step or the applied current purely supplies activation energy required to drive the reaction.
- ***Mass transport or concentration overpotential*** (η_{conc}) occurs when the mass transport to the reaction sites is the rate determining step.

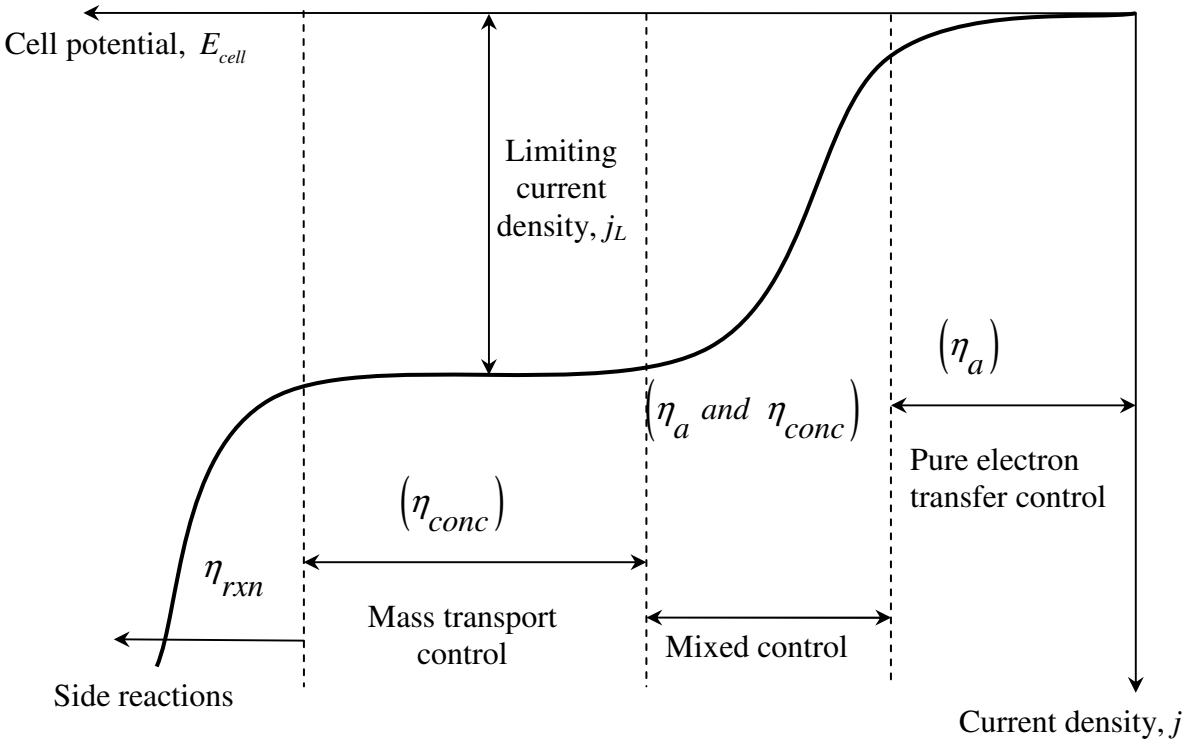

Fig 1.7: Figure showing the j- E_{cell} response and the corresponding region of electrode reaction along with the overpotentials associated[60].

In addition, the presence of side reactions such as gas evolution can lower the cell voltage by consuming a portion of the applied current, leading to reaction overpotential (η_{rxn}).

The occurrence of an overpotential during different steps of the electrode process is depicted in the Fig 1.7. This figure shows the occurrence of a charge transfer overpotential during the pure electron transfer step at low current densities, which is followed by a mixed region of activation and mass transport control, at intermediate current densities. This in turn is followed by a region of complete mass transport control at higher current

densities, where only concentration overpotentials can be observed. In this region the limiting current density can be determined. If the electrode potential increases beyond the region of mass-transport control, side reactions such as gas evolution can occur.

In dynamic operation, the same resistances and overpotentials are observed; in that case as functions of time or the state of charge. This is discussed in detailed in ***Chapter II***.

(b) Electrode kinetics

The relationship between the applied current (*I*) and the overpotential (η), for reaction (22) can be approximated by the Butler-Volmer equation[59]:

$$I = nFAk^0\left(c_O \exp\left(-\frac{\alpha nF}{RT}\eta_a\right) - c_R \exp\left(\frac{(1-\alpha)nF}{RT}\eta_a\right)\right) \tag{28}$$

where, $k^0 (= k_r = k_o)$ is the reaction standard rate constant, A is the active area of the electrode and α is a transfer coefficient ($\simeq 0.5$), which can be considered as the fraction of change in the overpotential leading to a change in the rate constant in the charge transfer controlled region[60].

At steady state, a simplified relationship between the applied current (*I*) and the activation overpotential (η_a) is given by[59]:

$$I = I_0\left(\exp\left(-\frac{\alpha nF}{RT}\eta_a\right) - \exp\left(\frac{(1-\alpha)nF}{RT}\eta_a\right)\right) \tag{29}$$

where $I_0 (= nFAk^0 c)$ is the exchange current, defined as the current equal in magnitude to that of the individual currents for the individual oxidation and reduction reactions on the

same electrode of active area A at equilibrium, when the rate constants for oxidation and reduction are equal (k^0), with a reactant (either oxidant or reductant) concentration of c[59].

(c) Electrolyte testing

The electrolytes used for the soluble lead-acid and copper-lead dioxide flow batteries in this thesis have been tested following a specific procedure: first a procedure to investigate the reaction kinetics of the redox pair was investigated followed by constant current deposition, using a classical Hull Cell, and finally testing using a small-scale flow cell.

The first test for the reaction kinetics was cyclic voltammetry using a rotating disc electrode (MSRX speed controller and rotator, Pine research instruments), which was connected to a computer-controlled Autolab® (PGSTAT302N with a 20 A booster, ECO CHEMIE). The concentration of the electroactive species in the electrolyte was kept low at all times ($\cong 20$ mmol dm^{-3}). This solution was placed into a three-electrode glass cell setup, with a platinum mesh as the counter electrode and a saturated calomel electrode (SCE) reference electrode. The rotating disc electrode is a hydrodynamic tool that uses forced convection to enhance the rate of mass transport to the electrode surface and enables both quantitative voltammetric and galvanostatic studies of the electrochemical reactions[61].

The mass-transport characteristics of the electroactive species to be used in the flow cell need to be determined as a function of the applied current density and the potential. The limiting current density j_L is the value at which the current density is independent of the potential and solely depends on the rate of mass-transport of the electroactive species to the electrode surface. The relationship between the limiting current density and the rate of mass transport of the electroactive species is given by the Levich equation[60]:

$$j_L = 0.623nFD^{2/3}\omega^{1/2}\nu^{-1/6}c \quad (30)$$

where D is diffusion coefficient of the reactant ($cm^2\ s^{-1}$), ω is angular velocity (rad s^{-1}), ν is kinematic viscosity coefficient of the electrolyte ($cm^2\ s^{-1}$) and c is the concentration (mol dm^{-3}) of the reactant or the electroactive species in the electrolyte.

The limiting current density values are plotted against the square root of the angular velocity of the rotating disc electrode (RDE). This provides a linear plot passing through the origin (when the electrochemical process is mass-transport controlled). The gradient can be used to calculate the diffusion coefficient of the reactants, which reflects the rate of mass transport within the electrolyte towards the electrode surface.

The concentrated electrolyte ($\geq$ 0.5 mol dm^{-3}) was then subjected to a series of constant current depositions using a Hull Cell (Kocour®). This cell is a very useful tool to observe electrodeposits under uncontrolled hydrodynamic conditions at constant currents. The trapezoidal shape of the cell allows variation in the depositions for a range of current densities. The relationship between the current density and the position a long the electrode can be approximated by[62]

$$j_x = I_{appl}\left(a - b\log x\right) \quad (31)$$

where j_x is the current density at a distance of x (distance along the cathode from the high current density end), I_{appl} is the applied current and a and b are constants (a = 5.10 and b = 5.24 when the units of measurements are expressed in cm and A cm^{-2}, respectively).

The deposits were characterised under a scanning electron microscope (SEM) and with energy dispersive X-ray (EDX) spectroscopy. The electrolyte was further tested in a 6 cm^2 flow cell[36]. It was then tested in a 100 cm^2 cell for scale-up and cyclability. Additives in the electrolyte were assessed to improve reversibility and cycling.

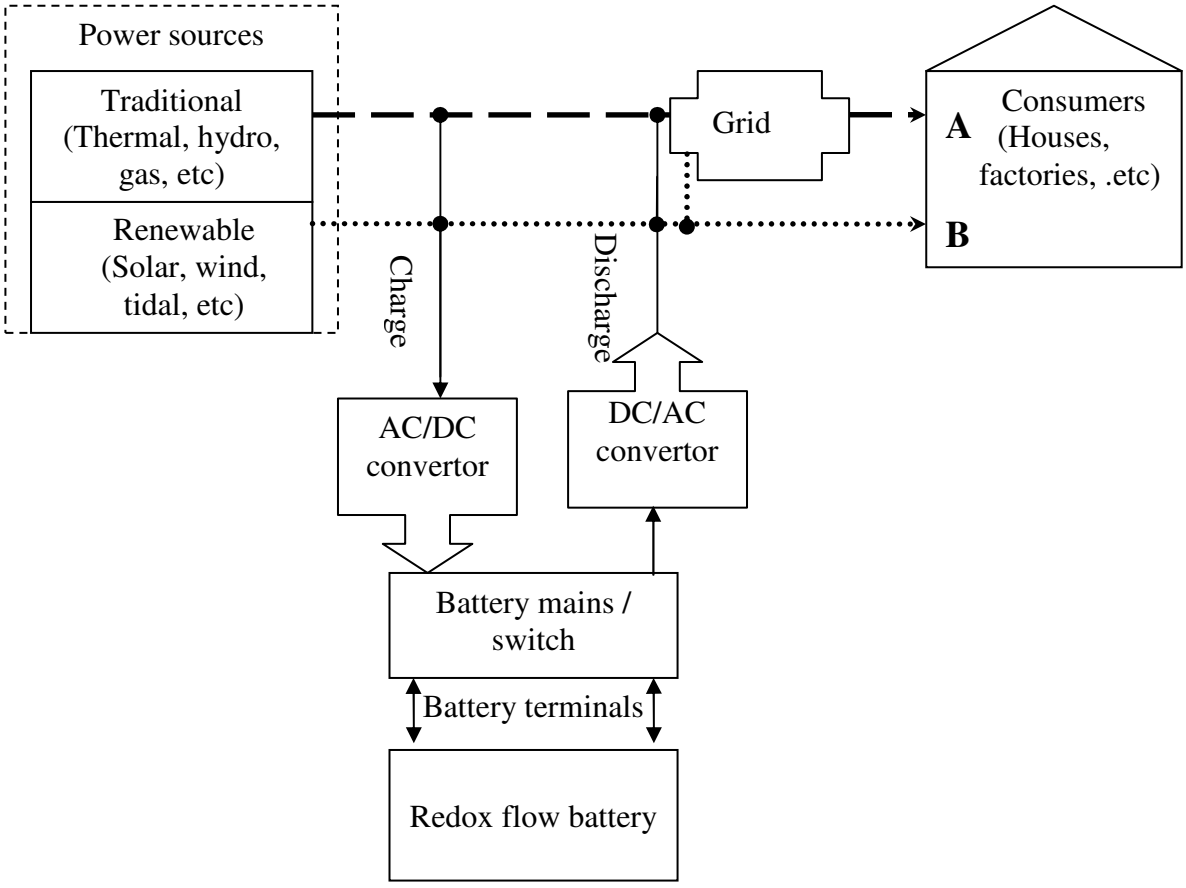

Fig 1.8: A schematic showing the application of redox flow battery at a commercial level with (**A**). possible connection through grid and (**B**). direct usage.

1.4.2. Discussion of scale-up

The successful scale–up and the extended cycling analysis would enable a RFB commercialization in two areas, namely as a stationary energy storage device or as a mobile energy storage/production unit (e.g. in electric vehicles). Each battery would have to be matched to the exact application requirements, such as high energy density or low power density[4,10,11]. The installed capacity of these applications can range from a few kW

to MW. Fig 1.8 provides a scenario for RFB utilization as a stationary energy storage device, with the following potential application;

(A) The battery is used in conjunction with an energy production unit (traditional/renewable) and the electrical grid, for load levelling and peak shaving, in which the battery would be charged at off-peak hours and discharged during peak hours. This would eliminate the need for additional generation units or high maintenance generation units.

(B) The battery is used with intermittent renewable energy conversion system, such as wind, solar and tidal; these systems can be made highly reliable by the use of energy storage devices. This can be done either by connecting to the grid or directly connecting to the consumer. The former can allow load levelling and/or peak shaving, whilst the latter can be used in isolated generation, stand alone systems or in places with reliable sources of natural energy, such as deserts and high seas.

The most commercialised of all of the three RFBs discussed in this thesis is the VRFB technology. Its application range from small (1kW) to medium scale (10-100 kW) energy storage[64] currently including wind farms[10], telecommunications[77], stand alone-systems[12], medium-scale energy storage in factories[11] and mobile devices such as golf carts[64]. Although patented 25 years ago[40,52] by University of New South Wales[64], the major corporations involved with research and development as well as the application of VRFB technology include, Re-Fuel Ltd., VRB Power[65], VFuel Pty Ltd.[66], Cellenium (Mitsubishi) Corporation[67], Sumitomo Electric Corporation, CellStrom GmBH[68]. Other variants such as the vanadium–bromine and the vanadium poly halide systems are also under investigation for further research and commercialization[31,55].

Similar applications could arise for the soluble lead-acid RFB, which has been developed towards pilot-scale operation in less than 10 years by the University of Southampton, C-Tech Innovation Ltd. and E.ON, UK[14,36,69-75]. This battery is of particular interest due to the high recyclability, low cost and availability of lead. Future applications include stand-alone medium to large scale energy storage connected to the electricity grids.

The copper-lead dioxide RFB is at the early stages of development; the electrochemistry, cell engineering and performance of the battery are actively under investigation. The possibility of operating at high current densities ($\geq$250 mA cm^{-2} at electrode areas $\cong$ 100 cm^2) is an attractive feature of this system, provided the voltage efficiency can be improved.

RFB technology has become more viable in recent years, partly due to the incentives provided by governments around the world and especially in Europe for meeting ambitious CO_2 reduction targets, via renewable power generation initiatives involving wind, tidal and solar energy installations[9,25,26,30,78]. The physical isolation of many power generation locations make the redox flow batteries a highly cost-efficient option for energy storage, transmission and distribution.

References:

[1]. B.P. Gollomp, *IEEE Transactions on Instrumentation and Measurement*, 52, **4**, 2003.

[2]. J. Kondoh, I. Ishii, H. Yamaguchi, A. Murata, K. Otani, K. Sakuta, N. Higuchi, S. Sekine, M. Kamimoto, *Energ Convers Manag,* **41** (2000) 1863

[3]. T. J. Hammons, J. S. McConnach, *Elec Power Compon Syst*, **33** (2005) 39.

[4]. R.M. Della, D.A.J. Rand, *J. Power Sourc.*, **100** (2001) 2.

[5]. I. Hadjipaschalis, A. Poullikkas, V. Efthimiou, *Renew Sustain Energ Rev,* **13** (2009) 1513.

[6]. J. Baker, *Energy Policy*, **36** (2008) 4368.

[7]. Varun, R. Prakash, I.K. Bhat, *Renew Sustain Energ Rev*, **13** (2009) 2716.

[8]. E. Martinot, *Energy Policy,* **29** (2001) 689

[9]. *'Towards a low carbon future'*, A European Strategic Energy Technology Plan (Set-Plan)**,** available online http://eur-lex.europa.eu/LexUriServ/LexUriServdo?uri=COM:2007:0723:FIN:EN:PDF, accessed on April 24, 2011.

[10]. R.M. Dell, *Solid State Ionics*, **134** (2000) 139.

[11]. S. Yoda, K. Ishihara*, J. Power Sourc.*, **81-82** (1999) 162.

[12]. "*Battery Technology for Data Centers and Network Rooms: VRLA Reliability and Safety*", White Paper # 39, American Power Conversion © 2003. ww.ptsdcs.com/ whitepapers/29.pdf, accessed on April 24, 2011.

[13]. R.G.A. Wills, "*A Lead-Acid Flow Battery for Utility Scale Energy Storage and Load Levelling*", Thesis for Degree of Doctor of Philosophy, University of Southampton, October 2004.

[14]. A. Hazza, D. Pletcher and R.G.A. Wills, *Phys Chem Chem Phys*., **6** (2004) 1773.

[15]. F.C. Walsh, *Pure Appl. Chem.*, **73** (2001) 1819.

[16]. M.J. Watt-Smith, R.G.A. Wills, F.C. Walsh, *Encyclopedia of electrochemical power sources*, **5** (2009) 438.

[17]. D. Linden, T. Reddy, "*Handbook of Batteries"* (3rd Edition) © 2002 McGraw-Hill.

[18].K. F. Blurton, H. G. Oswin, "*Refuelable Batteries",* available online http://www.anl. gov/PCS/acsfuel/preprint%20archive/Files/16_4_BOSTON_04-72_0048.pdf, accessed on April 24, 2011.

[19]. B. Schumm Jr., "*Batteries"*, Eagle Cliffs Inc*,* Cleveland, OH 44140, USA, *June 2002.*

[20]. C. Schaber, P. Mazza, R. Hammerschlag, *The Electricity Journal*, **17** (2004) 21

[21]. K.L. Blurton, H.G. Oswin, *Refeulable batteries*, available online http://www.anl. .gov/PCS/acsfuel/preprint%20archive/Files/16_4_BOSTON_04-72_0048.pdf, accessed on April 24, 2011.

[22]. C. Ponce-de-Léon, A. Fŕıas-Ferrer, J. Gonźalez-Garćıa, D.A. Sźanto, F.C. Walsh, *J. Power Sourc. ,* **160**, (2006), 716.

[23]. H. Ibrahima, A. Ilincaa, J. Perron, *Renew Sustain Energ Rev*, **12** (2008) 1221.

[24]. A. Rufer, **"***Solutions for Storage of Electrical Energy*", Laboratoired'électronique industrielle LEI, EPFL, Ecole Polytechnique Fédérale de Lausanne, CH 1015 Lausanne, Switzerland.

[25]. T. Shigematsu, T. Kumamoto, H. Deguchi, N. Tokuda, *Patent no: 7061205*, Sumitomo Electric Industries, Ltd. and The Kansai Electric Power Co., Inc., Osaka, Japan, 2006. http://www.freepatentsonline.com/ 7061205.html, accessed on April 24, 2011.

[26]. I. Tsuda, K. Kurokawa, K. Nozaki, *Photovol. Engy. Conv.*, **1** (1994) 946.

[27]. S.M. Schoenung and W.V. Hassenzahl, Sandia Report, Sandia National Laboratories, August, 2003. available online www.prod.sandia.gov/cgi-bin/techlib/access-control.pl/2003/032783.pdf., accessed on April 24, 2011.

[28].http://www.electricitystorage.org/ESA/technologies/technology_comparisons/, accessed on April 24, 2011.

[29]. A. Price, S. Bartley, S. Male, G. Cooley, *Power Eng J,* **13** (1999) 122.

[30]. "*Review of Electrical Energy Storage Technologies and Systems and of their Potential for the UK***",** report carried out under DTI Technology Programme: New and

Renewable Energy by EA technology first published 2004. www.berr.gov.uk/files/file15185.pdf., accessed on April 24, 2011.

[31]. M. Skyllas-Kazacos, *Encyclopedia of Electrochemical Power Sources*, (2009) 444.

[32]. C. Ponce de León, F.C. Walsh, *Encyclopedia of Electrochemical Power Sources*, (2009) 487.

[33]. A. Paulenova, S.E. Creager, J.D. Navratil, Y. Wei, *J. Power Sourc.*, **109** (2002) 431.

[34]. R.G.A. Wills, J. Collins, D. Stratton-Campbell, C.T.J. Low, D. Pletcher, Frank C. Walsh, *J. Appl. Electrochem.,* **40** (2010) 955.

[35]. J. Cheng, L. Zhang, Y.S. Yang, Y.H. Wen, G.P. Cao, X.D. Wang, *Electrochem Comm.*, **9** (2007) 2639.

[36]. D. Pletcher, R. Wills, *Phys Chem Chem Phys,* **6** (2004) 1779.

[37]. J. Pan, Y. Sun, J. Cheng , Y. Wen, Y. Yang, P. Wan, *Electrochem Comm.,* **10** (2008) 1226.

[38]. J.W. Long, B. Dunn, D.R. Rolison, H.S. White, *Chem. Rev.*, **104**(2004) 4463.

[39]. O. Vohler, P.L. Reiser, R. Martina, D. Overhoff, *Angew. Chem. Internat. Edit.,* **9** (1970) 414.

[40]. C. Ponce-de-Léon, F.C. Walsh, A. Rose, J.B. Lakeman, D.J. Browning, R.W. Reeve, *J. Power Sourc.*, **164** (2007) 441.

[41]. H. Zhou, H. Zhang, P. Zhao, B. Yi, *Electrochim. Acta,* **51** (2006) 6304.

[42]. J. Ludek, W. Yuezhou, M. Kumagai, *J. Rare Earths*, **24** (2006) 257.

[43]. W. Benzinger, K.J. Hüttinger, *Carbon*, **37** (1999) 941.

[44]. V. Neburchilov, H. Wang, J.J. Martin, W. Qu, *J. Power Sourc.*,**195** (2010) 1271.

[45]. J.M. Friedrich, C. Ponce-de-Léon, G.W. Reade, F.C. Walsh, *J. Electroanal. Chem.,* **561** (2004) 203.

[46]. I. Whyte, "*Reticulated vitreous carbon cathodes for metal ion removal*", Thesis for Degree of Doctor of Philosophy, University of Southampton, 1992.

[47]. M. Calvo, R. Garcı´a, S. R. Moinelo, *Energy & Fuels***, 22** (2008) 3376.

[48]. J.M. Rosolen, S. Tronto, M.S. Marchesin, E.C. Almeida, N.G. Ferreira, C.H.P. Poá, S.R.P. Silva, *App. Phy. Lett.*, **88** (2006) 083116.

[49]. J. Kim, M. Shioya, H. Kobayashi, J. Kaneko, M. Kido, *Comp. Sc. Tech.*, **64** (2004) 2221.

[50]. J. Kim, M. Shioya, H. Kobayashi, J. Kaneko, M. Kido, *Comp. Sc. Tech.*, **64** (2004) 2231.

[51]. http://www.entegrisfuelcells.com/StandardPlates.aspx, accessed on April 24, 2011.

[52]. M. Skyllas-Kazacos, M. Rychcik, R.G. Robins, A.G. Fane, M.A. Green, *J Electrochem Soc.*, (1986) 1057.

[53]. D.A. Johnson, M.A. Reid, *J Electrochem Soc.*, (1985) 1058.

[54]. P. Lex, B. Jonshangen, *Power Eng J.*, (1999) 142.

[55]. H. Vafiadis, M. Skyllas-Kazacos, *J Membr Sci.*, **279** (2006) 394.

[56]. http://plurionsystems.com/tech_flow_advantages.html, accessed on April 24, 2011.

[57]. D. Gernon, M. Wu, T. Buszta, P. Janney, *Green Chem.*, **1** (1999) 127.

[58]. M. Schlensinger, M. Paunovic, "*Modern Electroplating*", 4th edition, John Wiley and Sons. Inc.© 2000.

[59]. A.J. Bard, L.R. Faulkner, "*Electrochemical Methods: Fundamentals and Applications"*, 2nd Edition, Copyright 2001© John Wiley & Sons, Inc.,

[60]. D. Pletcher, "*A First Course in Electrode Processes*", 1991 the Electrochemical Consultancy, Romsey.

[61]. C.T.J. Low and F.C. Walsh, *Surf Coating Tech,* **202** (2008) 1339.

[62]. D.R. Gabe, *Met Finish,* **97** (1999) 592.

[63]. N. A. Hampson and A. J. S. McNeil, in '*Electrochemistry*', ed. D. Pletcher, Specialist Periodical Report, The Royal Society of Chemistry, London, **8** (1983) 1.

[64]. http://www.vrb.unsw.edu.au/ accessed on April 24, 2011

[65]. http://www.pdenergy.com/ accessed on April 24, 2011

[66]. http://vanadiumbattery.com/index.php/welcome/index/ accessed on April 24, 2011

[67]. http://www.cellstrom.com/ accessed on April 24, 2011

[68]. http://www.vfuel.com.au/ accessed on April 24, 2011

[69]. D. Pletcher, R.G.A. Wills, *J. Power Sourc.*, **149** (2005) 96.

[70]. A. Hazza, D. Pletcher and R.G.A. Wills, *J. Power Sourc.*, **149** (2005) 103.

[71]. D. Pletcher, H. Zhou, G. Kear, C.T.J. Low and F.C. Walsh, *J. Power Sourc.*, **180** (2006) 630.

[72]. D. Pletcher, H. Zhou, G. Kear, C.T.J. Low and F.C. Walsh, *J. Power Sourc.*, **180** (2008) 621.

[73]. X. Li, D. Pletcher, F.C. Walsh, *Electrochemi Acta*, **54**(2009) 4688.

[74]. J. Collins, G. Kear, X. Li, C.T.J. Low, D. Pletcher, R.C. Tangirala, D.S. Campbell, F.C. Walsh, C. Zhang, *J. Power Sourc.*, **195** (2010) 1731.

[75]. J. Collins, G. Kear, X. Li, C.T.J. Low, D. Pletcher, R.C. Tangirala, D.S. Campbell, F.C. Walsh, C. Zhang, *J. Power Sourc.*, **195** (2010) 2975.

[76]. J. Davis, "*Advantages of using Vanadium Redox Batteries in Telecommunications Prime Power Sites"*, VRB Power Systems, Inc., Vancouver B.C. V7Y1C6 Canada. http://www.vrbpower.com/docs/whitepapers accessed on April 24, 2011

[77]. E. Martinot, *Energy Policy,* **29** (2001) 689.

[78]. M. Bartolozzi, *J. Power Sourc.*, **27** (1989) 219.

Chapter -II

The All-Vanadium Flow Battery

2.1. Introduction

The all-vanadium redox flow battery (VRFB) is a well known flow battery technology developed and patented by the University of New South Wales in Australia[1] and is under commercialisation by a number of companies. This battery contains V(II)/V(III) $\left(V^{2+}/V^{3+}\right)$ and V(IV)/V(V) $\left(VO^{2+}/VO_2^{+}\right)$ redox couples in the negative and positive half-cell electrolytes, respectively[2,3], and has been the most widely studied RFB[4,5]. VRFBs are ideally suited for large-scale and medium-scale energy storage applications[6,7]. The systems are highly efficient (> 90 %) and recyclable[8]. During charge and discharge, the following reactions occur[9] at the positive and negative electrodes, respectively.

$$VO^{2+} + H_2O - e^- \underset{\text{discharge}}{\overset{\text{charge}}{\rightleftharpoons}} VO_2^{+} + 2H^{+} \qquad E^0 = +1.00\ V\ vs.\ \text{SHE} \qquad (1)$$

$$V^{3+} + e^- \underset{\text{discharge}}{\overset{\text{charge}}{\rightleftharpoons}} V^{2+} \qquad E^0 = -0.26\ V\ vs.\ \text{SHE} \qquad (2)$$

To provide electrical and vanadium ion insulation, as well as to maintain charge balance, an ion-exchange membrane, commonly Nafion®, is employed as a separator (as shown in Fig 2.1). If membrane crossover occurs, the half-cell electrolytes can be remixed and the system can be returned to its original state (albeit with a reduced energy efficiency). The VRFB possesses many advantages over other redox batteries and these are largely due to the use of vanadium redox couples in both half-cells. All of the reactants and products of the electrode reactions can remain soluble.

VRFB technology has commercially been used in combination with renewable energy sources such as wind turbines[10] and solar power installations[11]. It has also been used for stand alone applications, for load levelling and peak shaving[12], and in the field of telecommunications[13].

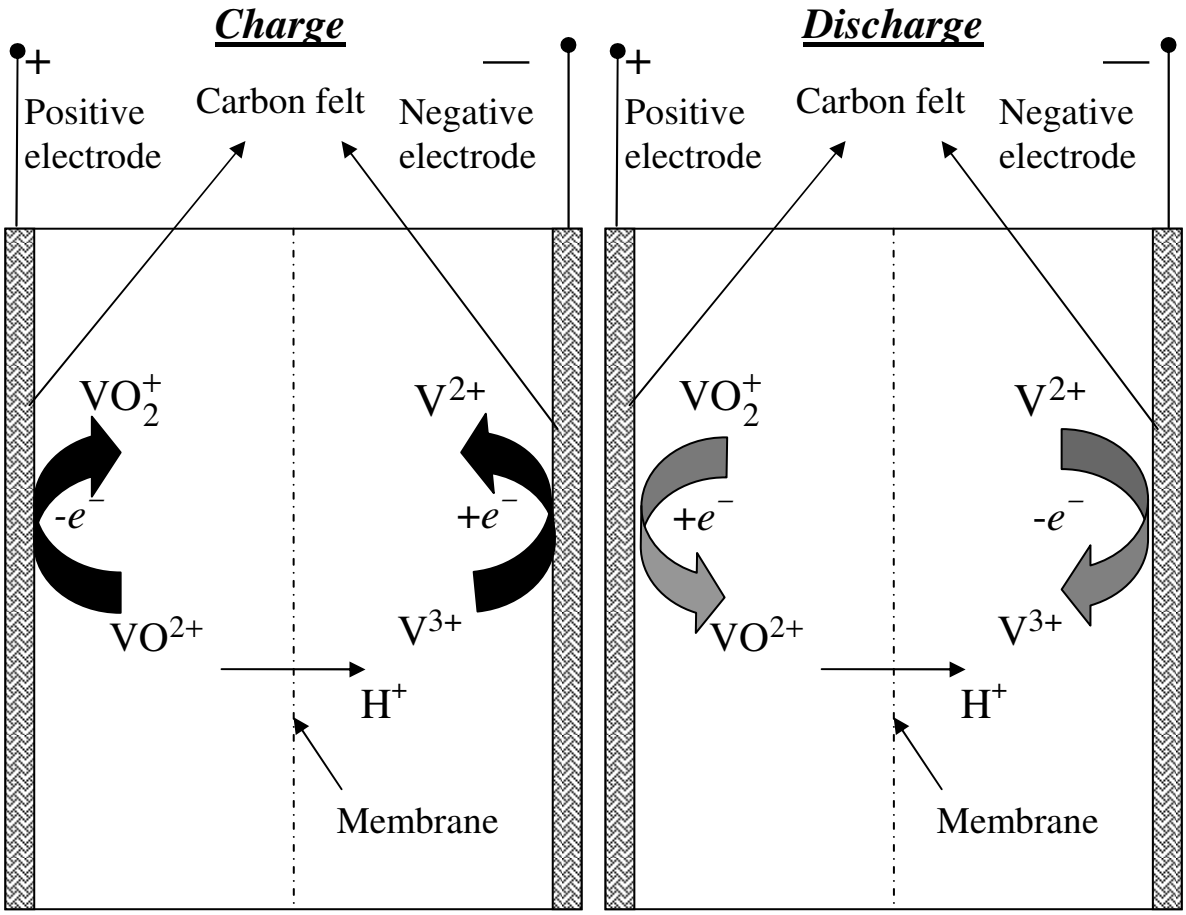

Fig 2.1: Schematic diagram showing the charge-discharge of an all-vanadium redox flow battery.

Previous research on VRFB systems has included electrode selection and characterisation[14-19], system optimisation[20,21], membrane studies[22-27] and investigation of the chemical reactions[9,28,29], together with electrolyte manufacture and characterisation[30-32] and mathematical modelling[33-36]. The effects on performance of different materials and of operating conditions such as the current density, the electrolyte flow rate, the vanadium concentration and, particularly, the system temperature remain relatively unexplored for operation under practical conditions. Such characterisation of VRFB systems and optimisation of their performance with respect to the reaction environment are essential to reducing costs, improving performance and developing systems that are capable of efficient scale-up.

Laboratory-based investigations (considering materials, operating conditions, additives and cell structure) can be highly costly, as well as time- and labour-intensive. In order to reduce costs and timescales, modelling and simulation can be employed during the design and test cycles, and used to control and monitor systems in real time[37-40] provided, of course, that the model parameters are available from suitable experimental data. Mathematical models of the VRFB system have also been developed by Shah *et al.*[33-34] and by Li and Hikihara[41]. These models incorporate the modes of transport (diffusion, convection and electron migration), the electrochemical kinetics (including hydrogen and oxygen evolution[35,36]) and heat losses[34]. It is not feasible, however, to incorporate this level of detail in control/monitoring tools or in stack models.

There is, therefore, a need to develop control-oriented models[42,43] that can rapidly, but accurately capture the performance of VRFB systems. Hence, in this thesis, such a control-oriented model was developed for a unit-cell VRFB system, and validated with charge-discharge data from a laboratory bench-top unit cell (100 cm^2 area), for different volumetric flow rates, vanadium concentrations, applied current densities and system temperatures.

2.2 Experimental arrangement

The experimental investigation reported in this chapter has been run on a 100 cm^2 custom-made flow cell system. Charge-discharge cycling of the VRFB was performed at constant current densities using an in-house designed control system with a D.C. power supply (Thurlby Thandar Instruments TSX3510p programmable PSU 35 V, 18 A) and an electronic load (Thurlby Thandar Instruments LD300 DC Electronic Load 80 V, 80 A). The vanadium electrolyte was obtained from a commercial source (Refuel Technology Ltd., UK). The electrolyte contained a total vanadium concentration in the range 1.0–1.6

mol dm^{-3}, as a V(III)/V(IV) mixture, in 4.0 mol dm^{-3} H_2SO_4, at a temperature of 297 ± 2 K. The volumetric flow rate was in the range 0.5–3 cm^3 s^{-1}.

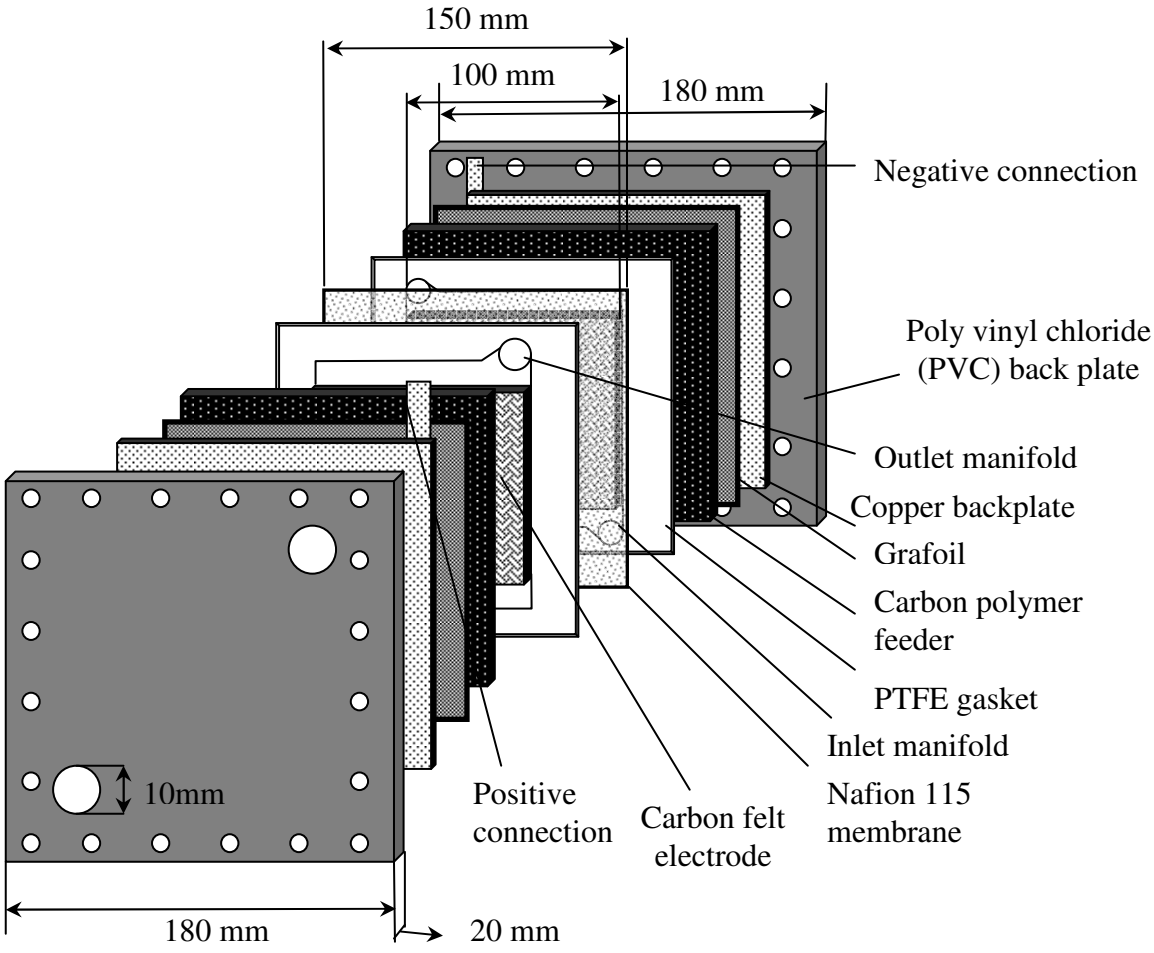

Fig 2.2: Exploded view of the 100 cm^2 vanadium flow battery unit test cell.

2.2.1. Test cell construction

The test cell was connected to two 0.25 dm^3 glass reservoirs (Scott Duran©) under N_2 atmosphere via a flow controlled double head peristaltic pump (Watson-Marlow Console drive 505s digital) using Norprene® A-60-F piping (10 mm outside diameter, 8 mm inside diameter). A Nafion® 115 proton exchange membrane (150 mm × 150 mm; dry thickness ca. 125 µm) divided cell containing graphite rods (8 mm diameter from Sigma Aldrich) was connected in hydraulic series *via* the outlet of each electrolyte compartment of the VRFB.

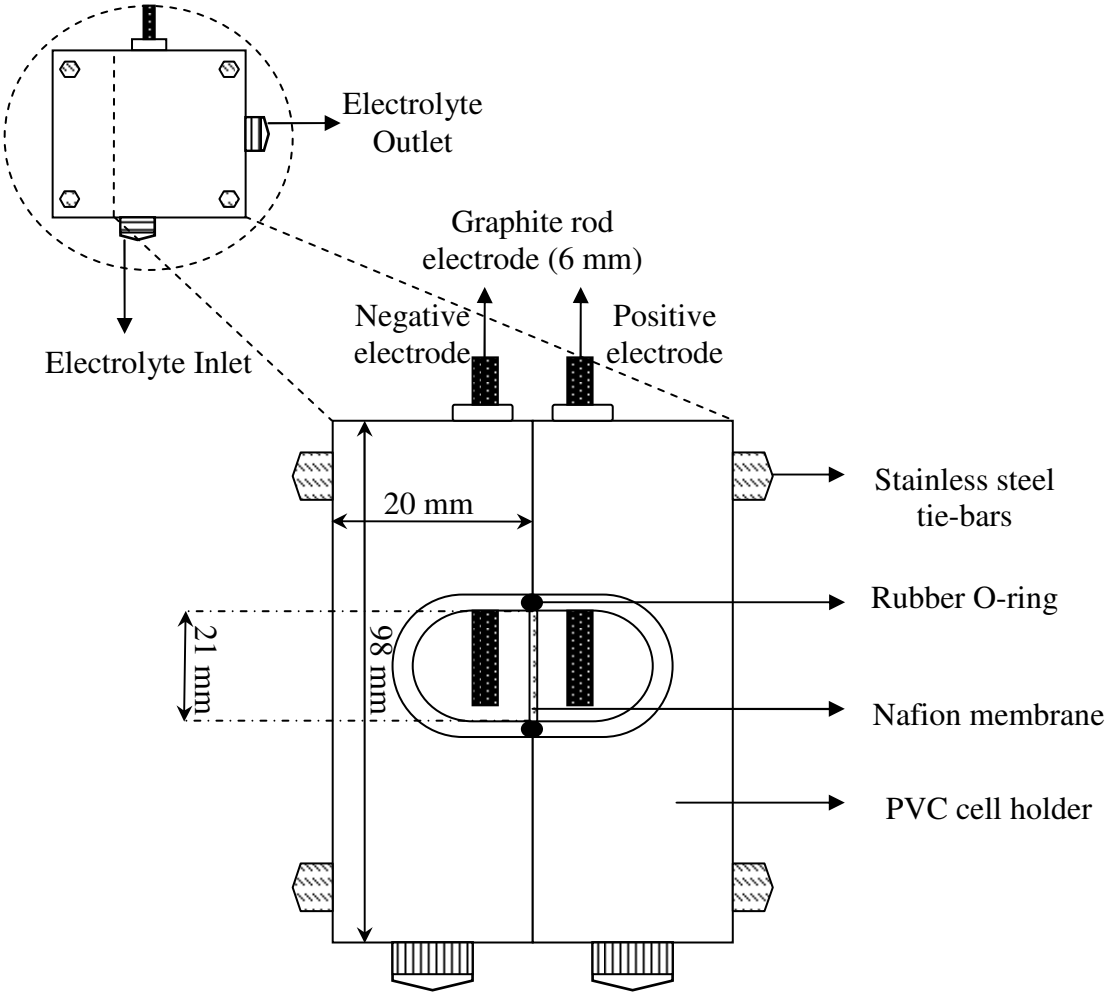

Fig 2.3: Cross-sectional view of the vanadium flow battery reference (OCV) cell (inset complete cell).

This (as shown in Fig 2.3) was used to monitor the open-circuit cell voltage (OCV) of the electrolyte solutions and provided a measure of the differential redox potential between the half-cell electrolytes leaving the cells, which was used as an indication of the open-circuit cell voltage (OCV) and, therefore, the state of charge (SoC). The unit cell (Fig 2.2) used two identical polyvinvylchloride outer plates (each 200 mm × 200 mm × 20 mm) and two copper end-plates (150 mm × 150 mm × 3 mm), held in place using two PTFE O-rings per plate. A GRAFOIL® flexible graphite foil (150 mm × 150 mm × 2 mm) was used to form a flexible interconnect to the copper end-plate.

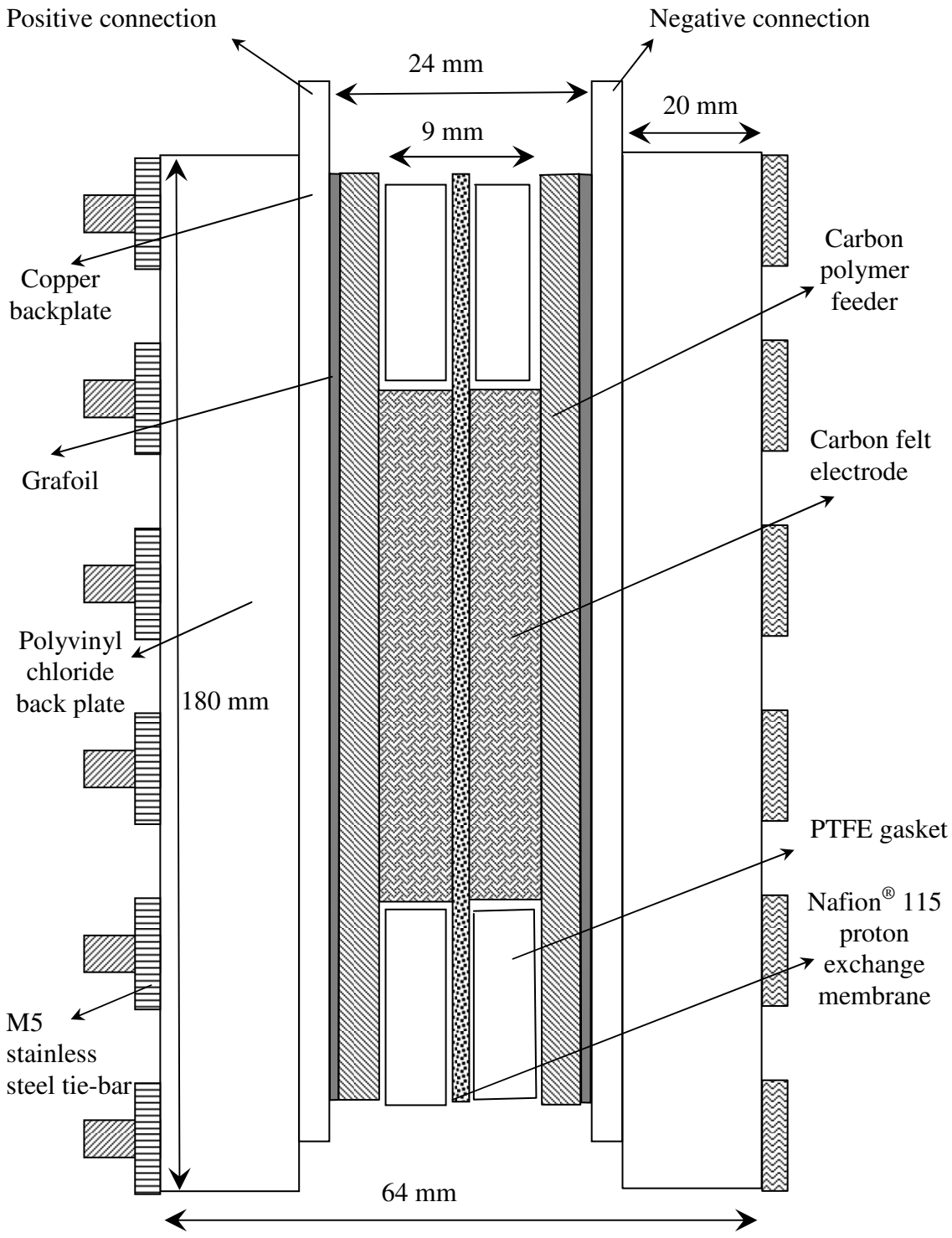

Fig 2.4: Vertical cross-sectional view of 100 cm^2 vanadium test cell.

Carbon feeder plates (150 mm × 150 mm × 5 mm) were placed on top of the graphite foil. PTFE gaskets (150 mm × 150 mm × 3 mm; active area of 100 mm × 100 mm) were positioned on top of the carbon plates and the Sigratherm®GFA5 type carbon felt electrodes (100 mm × 100 mm × 4 mm) were positioned within the gaskets. This carbon felt material is composed of carbon fibres with an average diameter of ca. 5–10 µm,

arranged in a random manner. The half-cell construction has been shown in Fig 2.5 and the complete cell in the Fig 2.2 and Fig 2.4. A sheet of Nafion® 115 (150 mm × 150 mm; dry thickness ca. 125 µm) was positioned between the half-cell compartments and the battery was compressed using M5 stainless steel tie-bolts. A thin film of silicone sealant was used to prevent electrolyte leakage during cell operation. The flow distribution was a rectangular open channel (10 mm × 100 mm) cut on both sides of the first PTFE gasket with inlet and outlet manifolds at the diagonal corners, shown in Fig 2.5. This open inlet/outlet design promoted the electrolyte to flood the reaction chamber filled with the carbon felt, enabling it to flow through the porous carbon felt.

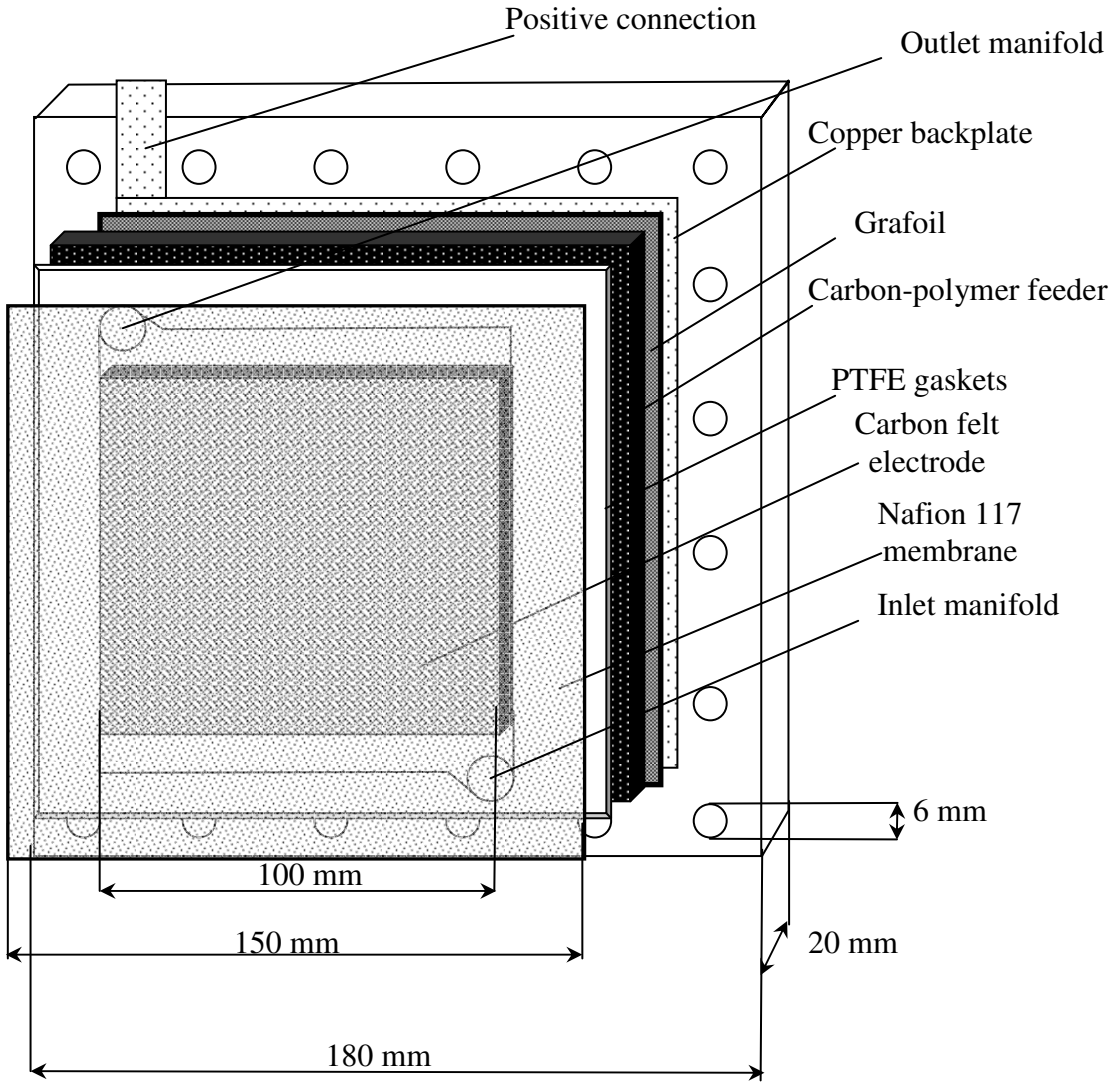

Fig 2.5: Half-cell view of 100 cm^2 vanadium flow battery test cell.

Experiments were also performed at different temperatures between 25 and 45 °C. The electrolyte temperature was controlled using a water bath consisting of a 10-inch diameter crystallization bowl where the electrolyte reservoir were immersed and a 1.5 cm diameter polyethylene hollow balls were used to reduce evaporation. The crystallization bowl was temperature-controlled by a hotplate (IKATHERM®). A temperature probe was inserted into the water to control and monitor the temperature of the bath. The water was continuously stirred to provide an even temperature distribution around the immersed electrolyte flasks. The water and electrolyte temperatures were monitored separately using thermometers inserted into the bath and electrolyte tanks. Before charge-discharge cycling, the electrolyte was circulated through the cell to avoid a temperature difference between the cell and electrolyte reservoir, as well as to raise or reduce the temperature to the required level. This process took between 2 and 10 min, depending on the temperature difference and whether heating or cooling was required. The error in the temperature measurement was estimated to be ± 0.5 °C.

In the charge-discharge experiments a constant current, typically in the range 2–10 A, corresponding to a current density of 20–100 mA cm^{-2} based on the projected area of each electrode, was used. The charge and discharge times were determined by the value of the open-circuit cell voltage as approximated by the potential difference across the monitoring cell 1.3 V at the end of each discharge and 1.5 V at the end of each charge. The cell was kept at open-circuit conditions for 2 min between each charge and discharge period. Typically, the charge and discharge parts of a cycle were each 30–40 min in duration. The cell was cycled up to 30 times. All experiments exhibited excellent reproducibility.

2.2.2. Cell voltage and sources of voltage loss

A brief review of the voltage losses in the cell is given below in order to facilitate the discussion that follows. Given an applied current density, j_{app}, the cell voltage (or cell potential difference), E_{cell} is calculated from the following formula[46]:

$$E_{\text{cell}} = E^0_{\text{cell}} - \sum_k (IR)_k - \sum_k |\eta| = E^0_{\text{cell}} - (IR)_m - (IR)_e - (IR)_c - \eta_a \tag{3}$$

in which E^0_{cell} is the equilibrium potential (since the outlet concentrations are used to calculate the OCV in the experimental monitoring of the cell, the state of charge definition is the same for both the model and experiments, though small differences exist between the true OCV and the OCV measured by the monitoring cell as discussed in section 2.2), η_a is the activation overpotential (with contributions from each electrode), $(IR)_m$ is the ohmic drop across the membrane, $(IR)_e$ is the ohmic drop associated with the electrolyte and $(IR)_c$ is the ohmic drop associated with the current collector (electrodes and electrical contacts). The OCV can be approximated using Nernst's equation (assuming unit activity coefficients) as follows[46]:

$$\begin{aligned} E^0_{\text{cell}} &= (E^0_2 - E^0_1) + \frac{RT}{F}\ln\left(\frac{c_{\text{V(II)}}c_{\text{V(V)}}[\text{H}^+]^2}{c_{\text{V(III)}}c_{\text{V(IV)}}}\right) \\ &= E^0 + \frac{RT}{F}\ln\left(\frac{c_{\text{V(II)}}c_{\text{V(V)}}}{c_{\text{V(III)}}c_{\text{V(IV)}}}\right) + \frac{4.6RT}{F}\log_{10}[\text{H}^+] \end{aligned} \tag{4}$$

where: E^0_1 and E^0_2 (both functions of temperature) are the formal potentials for the reactions at the negative and positive electrodes, respectively and $E^0 = E^0_2 - E^0_1$; R is the molar gas constant; T is the cell temperature; F is the Faraday constant; and c_i is the

molar concentration of (spatially distributed) species *i*, where *i* = $\mathrm{V(II), V(III), V(IV), V(V)}$. For low flow rates (< 1 $\mathrm{cm^3\ s^{-1}}$), a high degree of stratification in the reactant concentrations would develop between the inlet and outlet to the cell. The proton activity has been approximated by the concentration (mol $\mathrm{dm^{-3}}$) of protons, $[\mathrm{H^+}]$ in the positive electrode. Note that the final term in equation (4) could be written in terms of the pH of the positive electrode solution, $\mathrm{pH} = -\log_{10}[\mathrm{H^+}]$. The formal potentials depend on temperature[47]. The variations are, however, small and therefore neglected. The activation overpotentials can be approximated using Butler-Volmer equation to the transfer current densities in each electrode. In the negative electrode, for example:

$$j = Fk(c_{\mathrm{V(III)}})^{\alpha}(c_{\mathrm{V(II)}})^{1-\alpha}\left\{\exp\left(-\frac{\alpha F\eta_1}{RT}\right)-\exp\left(\frac{(1-\alpha)F\eta_1}{RT}\right)\right\} \tag{5}$$

where $j = I/A$ is the applied current density (A is the electrode area $\mathrm{cm^2}$), α is the cathodic charge transfer coefficient and k is a reaction constant.

The overpotentials associated with the activation barrier to the electrode reactions can be calculated individually by inverting the Butler-Volmer equation (assuming equal charge transfer coefficients of 0.5) as follows[46]:

$$-\text{ve electrode (charge)}:\ \eta_1 = -\frac{2RT}{F}a\sinh\left(\frac{j_{\mathrm{app}}}{2Fk_1\sqrt{c_{\mathrm{V(III)}}c_{\mathrm{V(II)}}}}\right) \tag{6}$$

$$+\text{ve electrode (charge)}:\ \eta_2 = \frac{2RT}{F}a\sinh\left(\frac{j_{\mathrm{app}}}{2Fk_2\sqrt{c_{\mathrm{V(IV)}}c_{\mathrm{V(V)}}}}\right) \tag{7}$$

where k_1 and k_2 are the reaction rate constants associated with the reactions at the positive and negative electrodes, respectively (they can be related to the reference exchange current densities and reference reactant concentrations). The reaction constants are temperature dependent, and can be expressed as follows[42]:

$$k_1 = k_{1,ref} \exp\left(-\frac{FE_1^0(T_{ref})}{R}\left[\frac{1}{T_{ref}} - \frac{1}{T}\right]\right) \tag{8}$$

$$k_2 = k_{2,\mathrm{ref}} \exp\left(\frac{FE_2^0(T_{\mathrm{ref}})}{R}\left[\frac{1}{T_{\mathrm{ref}}} - \frac{1}{T}\right]\right) \tag{9}$$

for known reference values, $k_{1,\mathrm{ref}}$ and $k_{2,\mathrm{ref}}$ (given in Table 2.2), measured at some reference temperature T_{ref}.

The concentrations in equations (4) and (6 & 7) are, strictly speaking, the concentrations of the respective species at the reaction sites in the porous electrodes (on the fibre surfaces). These concentrations are different from the bulk concentrations due to the development of a stagnant boundary layer. Details on how to incorporate the additional resistances to mass transport across the boundary layer are given by Shah *et al.*[33]; the surface concentrations are related to the bulk concentrations through diffusive mass transfer coefficients, γ_i for each reactant, which are inversely proportional to the thickness of the boundary δ_i layer for each reactant. In the limits $\delta_i \to 0$, the surface concentrations approach the bulk concentrations and the additional resistances vanish. The thickness of each boundary layer can be related to the mean electrolyte flow velocity (cm s^{-1}) through the electrode, v in the direction from the inlet to the outlet of the electrode[45]:

$$\delta_i = \frac{K}{\sqrt{v}} \tag{10}$$

where K is a constant of proportionality.

2.3. Results and discussion

Charge-discharge tests were performed at flow rates of 0.5, 1, 1.5, 2 and 3 $cm^3\ s^{-1}$ and vanadium concentrations of 1.5 mol dm^{-3} and 1.1 mol dm^{-3}, at 25 ^oC. The current during charging and discharging was set to 100 mA cm^{-2} and measurements of the working cell voltage, the open-circuit monitoring cell voltage (to estimate the OCV) and the current density were obtained for each experiment. The monitored cell voltage was used to control the state of charge (cycled between 1.3 V and 1.5 V) so that an equivalent state of charge was reached at the beginning and end of each charge and discharge cycle (separated by 120 s at the OCV), for all experiments conducted.

The performance characteristics of the VRFB at the various electrolyte flow rates and electrolyte concentrations are shown in Fig 2.6. There are significant differences between the values of voltage efficiency for the two concentrations. The difference in the average voltage efficiency between the two concentrations (56 ± 0.4 % for 1.1 mol dm^{-3} and 65 ± 0.4 % for 1.5 mol dm^{-3}) was 9 %, indicating that the 1.5 mol dm^{-3} solution provides significantly improved efficiency. Examples of the charge-discharge curves for each concentration, at a flow rate of 2 $cm^3\ s^{-1}$, are shown in Fig 2.7. In both cases, the reproducibility of the cycling was very good, with relaxation to a stable charge-discharge profile within the first few cycles. The charge and discharge times in Fig 2.7 (a) are approximately 10 min shorter than those in Fig 2.7 (b) (≈ 35 min *vs.* ≈ 45 min). The much lower cell voltage values at the end of the discharge for the 1.1 mol dm^{-3} case (hence the lower voltage efficiency) are also noticeable. Referring to equation (6) and (7), a lower

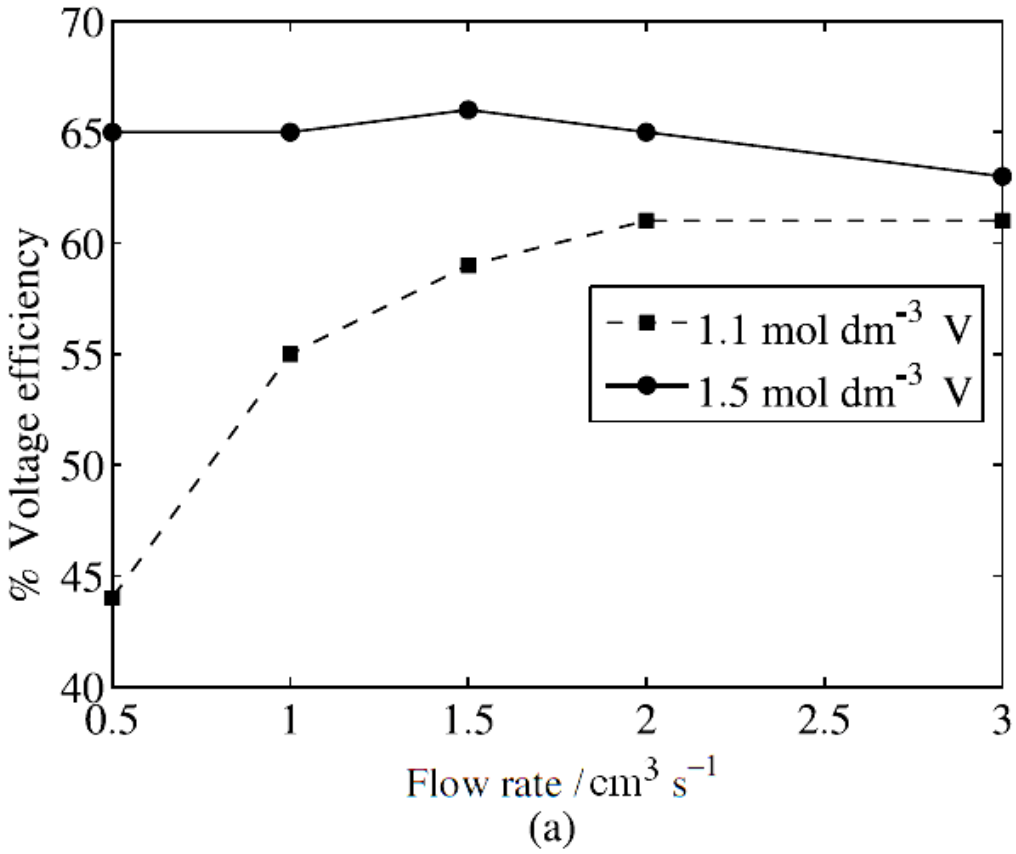

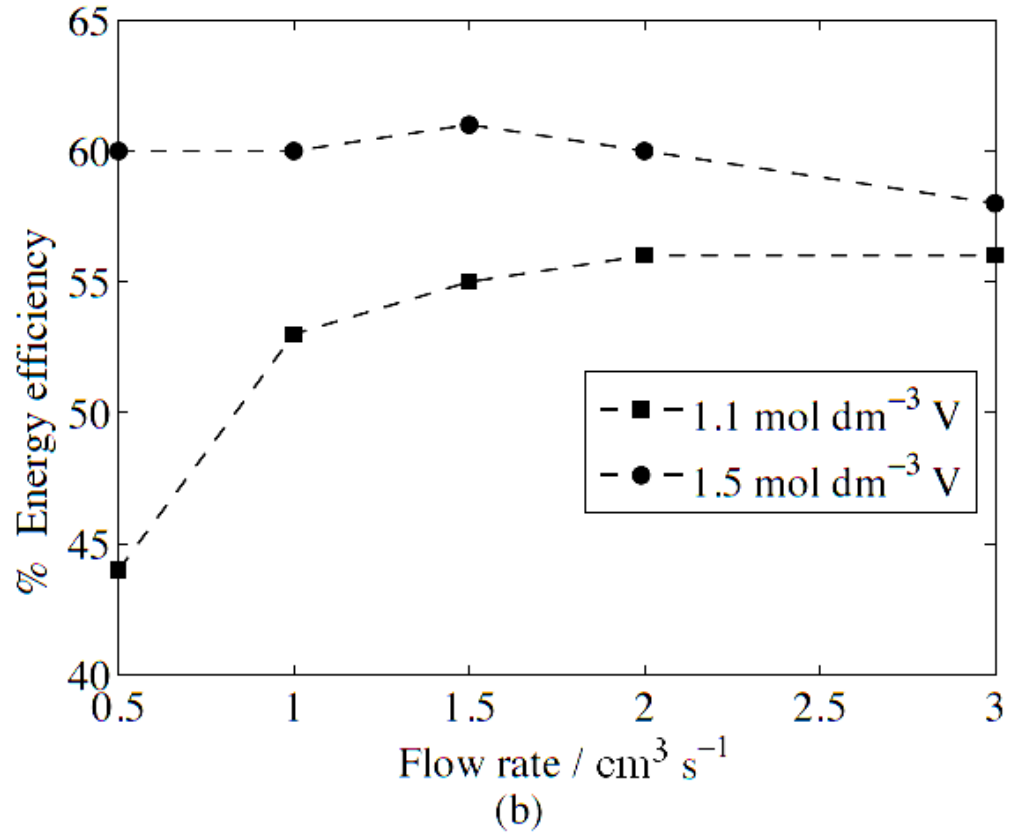

Fig 2.6: (a) Voltage and (b) energy efficiencies of a 100 cm^2 VRFB test cell charge-discharging at 10 A for concentrations: 1.1 mol dm^{-3} and 1.5 mol dm^{-3} of total vanadium ions in 4 mol dm^{-3} H_2SO_4 at 25°C for different mean linear electrolyte flow rates.

activation/concentration overpotential is attained for higher concentrations of the reactants, at an equivalent state of charge for a fixed current density. The time to charge is, therefore, longer. Note that the state of charge is determined by the ratios of the reactants, as indicated in equation (4), so that $c_{V(III)}$ and $c_{V(II)}$, for example, must be increased in proportion to achieve the same state of charge.

At a vanadium concentration of 1.1 mol dm^{-3}, the maximum voltage efficiency was seen at a flow rate of 2 cm^3 s^{-1} and higher, while at 1.5 mol dm^{-3} the maximum voltage efficiency was observed at 1.5 cm^3 s^{-1} (Fig 2.6). This finding indicates that when the vanadium concentration is lowered, an increased flow rate is required to maintain the same voltage efficiency. The higher electrolyte flow rate distributes the reactants more uniformly inside the electrode, leading to a reduced degree of concentration polarisation. According to equation (6) and (7), a higher flow rate also reduces the thicknesses of the stagnant boundary layers, lowering the resistance to mass transport.

In the case of a of 1.1 mol dm^{-3} concentration, the energy efficiency increased substantially as the flow rate was increased from 0.5 to 1.5 cm^3 s^{-1} (Fig 2.7 (a)). A peak energy efficiency of 56 % was attained for 2 cm^3 s^{-1}, with no further increase at 3 mL s^{-1}. It is notable that the improvements in the voltage and energy efficiencies were negligible when the flow rate was doubled from 1.5 cm^3 s^{-1} to 3 cm^3 s^{-1}. At this concentration, the optimal flow rate (to deliver the highest overall efficiency) is therefore in the range 1.5–3 cm^3 s^{-1}. In contrast, the performance of the system at 1.5 mol dm^{-3} did not vary significantly with flow rate, with the worst performance seen at 3 cm^3 s^{-1}.

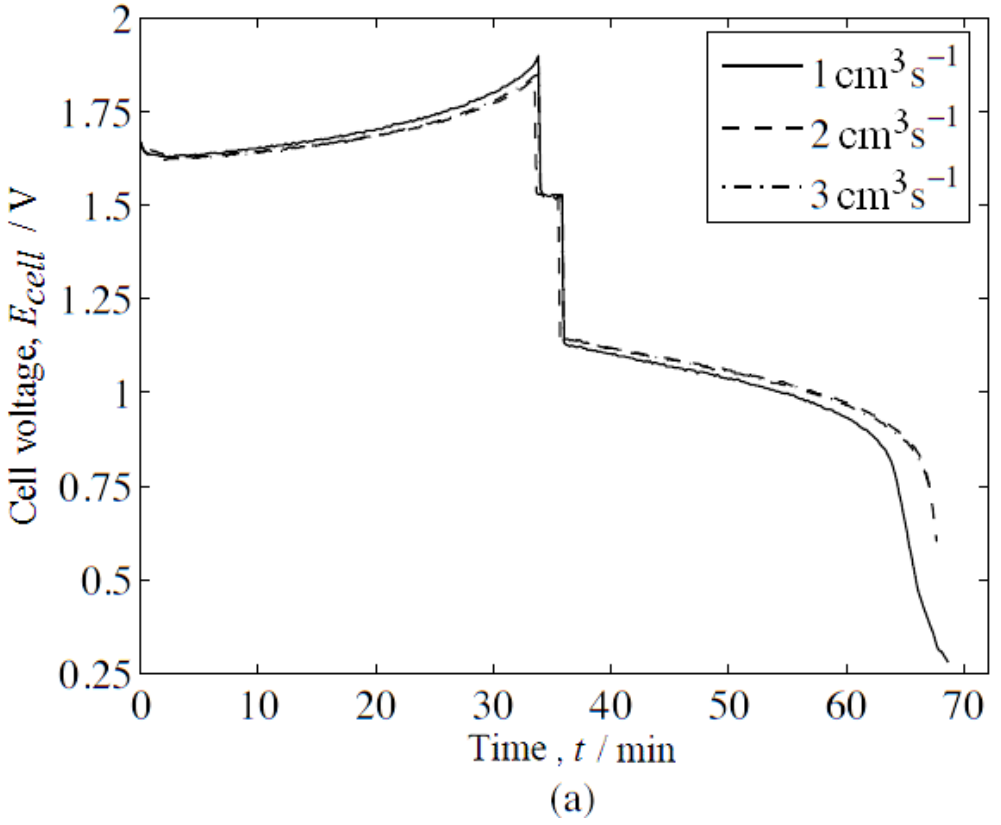

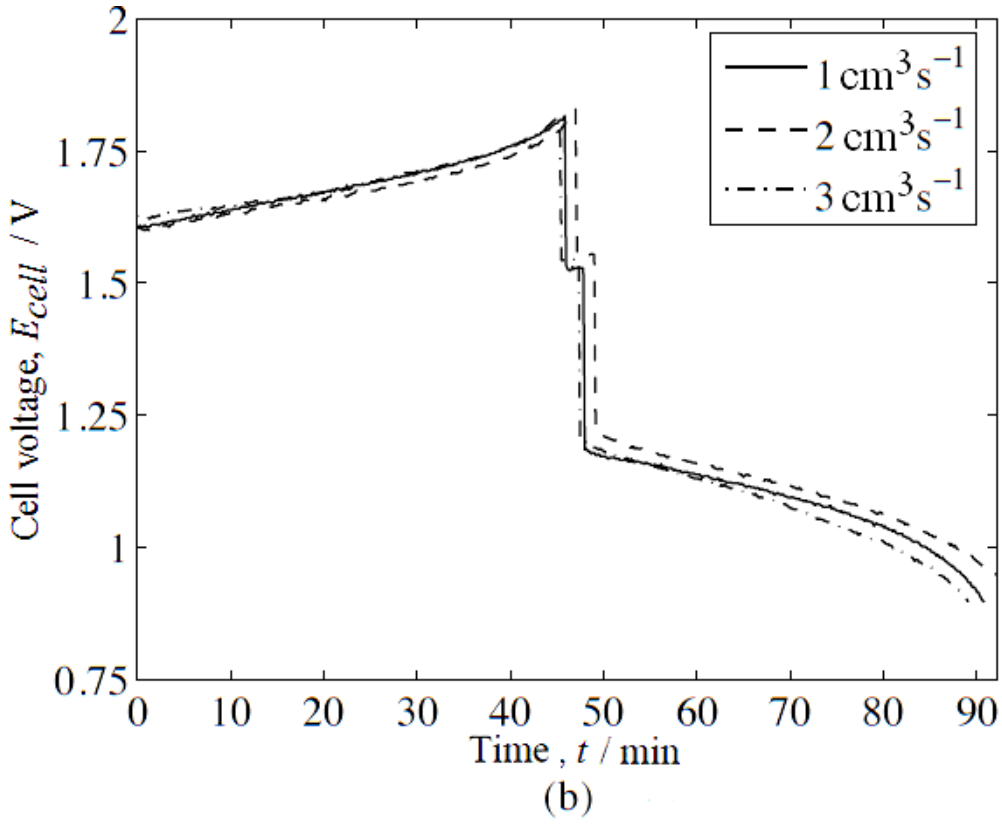

Fig 2.7: Charge-discharge performance at 10 A of 100 cm^2 VRFB test cell at different flow rates with electrolyte concentration of (a) 1.1 mol dm^{-3} and (b) 1.5 mol dm^{-3} of total vanadium ions in 4 mol dm^{-3} H_2SO_4 at 25 °C.

2.3.1. Effects of current density

In order to gauge the effect of the applied current (or current density), further charge-discharge experiments were conducted at 25 mA cm^{-2}, 50 mA cm^{-2} and 100 mA cm^{-2}, respectively, under the conditions described in the previous subsection (charge-discharge between 1.3 V and 1.5 V reference cell voltage), with a vanadium concentration of 1.1 mol dm^{-3} and an electrolyte flow rate of 1 cm^3 s^{-1}, at 25 ^oC.

Current density / mA cm^{-2}	**% Voltage efficiency**	**% Energy efficiency**
25	71.2	67.9
50	62.3	59.2
100	55.1	53.0

Table.2.1: Efficiencies of the VRFB at different charge/discharge currents, for a flow rate of 1 cm^3 s^{-1} and a total vanadium concentration of 1.1 mol dm^{-3} (in 4 mol dm^{-3} H_2SO_4) at 25 ^oC.

The calculated voltage and energy efficiencies are shown in Table 2.1. In all experiments, the charge efficiencies were $\cong 95$ %, indicating slow rates of oxygen and hydrogen evolution. The voltage efficiencies, on the other hand, decreased by approximately 16 % as the current was increased from 2.5 A to 10 A. As the current is increased, the ohmic drops across the resistive components will increase, resulting in a greater deviation of the cell voltage from the OCV. Equation (6) and (7) also shows that at fixed concentrations, a higher current density increases the activation/concentration overpotentials (at an equivalent state of charge). The increase in the ohmic drop across the electrolyte could be particularly pronounced since the resistivity of the electrolyte to ion transport is much higher than the electrical resistivity of the solid components. This is significant on discharge, since the reverse of reaction (1) is dependent on the proton concentration, so

that reaction in the positive electrode may be more confined to the membrane/positive-electrode interface as the current is increased.

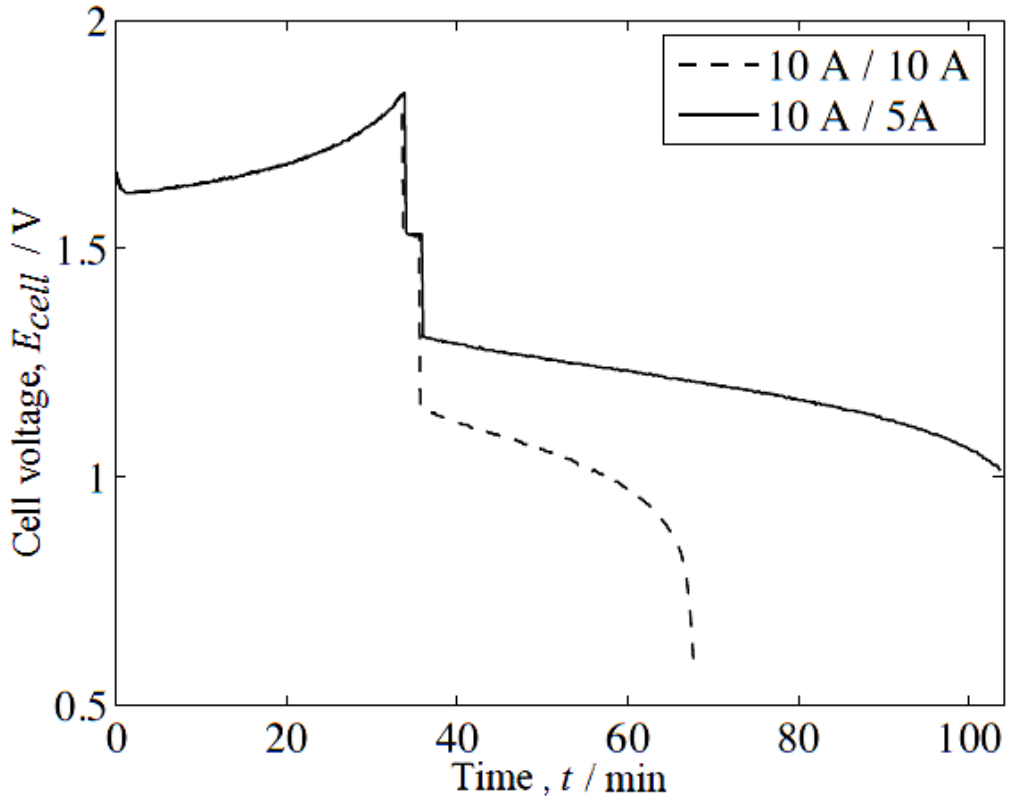

Fig 2.8: A comparative charge-discharge curve of a 100 cm^2 VRFB test cell with electrolyte 1 mol dm^{-3} of total vanadium ions in 4 mol dm^{-3} H_2SO_4 at a flow rate of 1 cm^3 s^{-1} (at 25 ^oC) charging at 10A with discharge at 10 A (100 mA cm^{-2}) and at 5 A (50 mA cm^{-2}).

The voltage efficiency was found to improve dramatically when the discharge current was halved. For example, Fig 2.8 shows a typical cycle with charging at 10 A (100 mA cm^{-2}) and discharging at 5 A (50 mA cm^{-2}) using an electrolyte with 1.1 mol dm^{-3} vanadium ions in 4 mol dm^{-3} H_2SO_4 supplied at a flow rate of 1 cm^3 s^{-1} at 25 ^oC. Cut-off values for the open-circuit cell voltage of 1.5 V during charge and 1.3 V during discharge were used to define the charge and discharge times, respectively. An equivalent cycle with charging and discharging at 10 A is shown for comparison. Similar improvements were observed under charging at 5A and discharging at 2.5 A, at flow rates between 1 cm^3 s^{-1} and 3 cm^3 s^{-1}, with highly reproducible cycles.

2.4. A control-oriented model for the unit-cell VRFB system

In the following section 2.4.1, a control oriented model is developed and is validated using parametric studies as shown in section 2.4.2.

2.4.1. Model equations

The electrochemical reactions included in the model are shown in equations (1) and (2). Under normal operating conditions, oxygen and hydrogen evolution kinetics are not favoured in the all-vanadium system given the values of the standard potentials for reactions (1) and (2). Furthermore, self discharge is neglected given the high charge and discharge currents considered.

The cell voltage can be calculated from equation (3) and the Nernst (theoretical open-circuit) voltage from equation (4). The ohmic losses associated with the current collector, membrane and the electrolyte can be modelled as follows:

$$(IR)_c = j_{\text{appl}} \frac{w_c}{\sigma_c}; \quad (IR)_m = j_{\text{appl}} \frac{w_m}{\sigma_m}; \quad (IR)_e = j_{\text{appl}} \frac{w_e}{\varepsilon^{3/2}\sigma_e} \tag{11}$$

respectively, where, σ_c, σ_m and σ_e are the conductivities and w_c, w_m and w_e are the widths of the current collector, membrane and the electrolyte, respectively. Note that a Bruggeman correction has been used in the case of $(IR)_e$ to obtain the effective conductivity $\varepsilon^{3/2}\sigma_e$. For a Nafion membrane, the following empirical relationship can be employed[48]:

$$\sigma_m = (0.5139\lambda - 0.326)\exp\left(1268\left[\frac{1}{303} - \frac{1}{T}\right]\right) \tag{12}$$

in S m^{-1}, where λ is the membrane water content (moles of H_2O to moles of SO_3^-). Since the membrane is in constant contact with the liquid electrolyte on both sides, it is reasonable to assume that it is fully saturated; that is[50], $\lambda = 22$.

The recirculation of the electrolytes through reservoirs alters the concentrations of all species entering the electrodes. To model recirculation, the concentration of species *i* in the appropriate reservoir, c_i^{res} is introduced. The outlet/inlet area of the electrodes is given by $A_{in} = b_e w_e$, where b_e and w_e are the breadth and width of the electrode, respectively (see default values are given in Table 2.3). Assuming a constant liquid density, conservation of volume demands that the net change per unit time in the number of moles of species *i* in the electrode due to recirculation is approximately equal to $\varepsilon A_{in} u(c_i^{res} - c_i)$, where ε is the porosity of the electrode and *u* is the electrolyte flow velocity (in m s^{-1}). Similarly, the net change in the reservoir concentration is approximately $-\varepsilon A_{in} u(c_i^{res} - c_i)$. Therefore, the mass balance of species *i*, in the reservoirs is:

$$\frac{dc_i^{res}}{dt} = -\frac{\varepsilon A_{in} u}{V_r}(c_i^{res} - c_i) = -\frac{\varepsilon \delta u}{h_e}(c_i^{res} - c_i) \tag{13}$$

where εA_{in} is the actual area of the electrode, h_e is the height of the electrode, $V_e = b_e w_e h_e$ is the volume of the electrode, V_r is the volume of the reservoir and $\delta = V_e / V_r$ (see Table 2.3 for typical values). Note that the relationship $A_{in} = V_e / h_e$ was used above.

The mass balance for species *i* in the electrode incorporates recirculation and electrochemical reaction:

$$\varepsilon V_e \frac{dc_i}{dt} = \varepsilon A_{in} u(c_i^{res} - c_i) - A_s \frac{j_{\text{app}}}{F} \qquad i = \text{V(III), V(IV)} \tag{14}$$

$$\varepsilon V_e \frac{dc_i}{dt} = \varepsilon A_{in} u(c_i^{res} - c_i) + A_s \frac{j_{\text{app}}}{F} \qquad i = \text{V(II), V(V)} \tag{15}$$

where A_s is the active surface area for reaction, which can be written as $A_s = SV_e$, where S is the specific surface area (per unit volume of the bulk electrode). Eliminating the recirculation terms in equations (13) and (14) yields:

$$\frac{d}{dt}\left(\varepsilon\delta c_i + c_i^{res}\right) = -\frac{\delta S}{F} j_{\text{app}} \tag{16}$$

which can be integrated, assuming a constant charge/discharge current, to give:

$$c_i^{res} = (\varepsilon\delta + 1)c_i^0 - \frac{\delta S}{F} j_{\text{app}} t - \varepsilon\delta c_i \qquad i = \text{V(III), V(IV)} \tag{17}$$

subject to the initial conditions $c_i = c_i^{res} = c_i^0$. Equation (14) can now be recast as follows:

$$\frac{dc_i}{dt} + \tilde{\varepsilon} c_i = \tilde{\varepsilon} c_i^0 - \frac{S j_{\text{app}}}{\varepsilon F}\left(1 + \frac{\varepsilon\delta}{\tau} t\right) \tag{18}$$

in which:

$$\tau = \frac{h_e}{u} \quad \text{and} \quad \tilde{\varepsilon} = \frac{1}{\tau}(\varepsilon\delta + 1) \tag{19}$$

The ratio $\tau = h_e / u$ is a direct measure of the residence time for reaction. The solutions to equations (18), together with the initial conditions are:

$$c_i = c_i^0 + \frac{S j_{\text{app}}}{\varepsilon \tilde{\varepsilon} F}\left(\frac{\varepsilon\delta + e^{-\tilde{\varepsilon} t}}{1+\varepsilon\delta} - 1 - \frac{\varepsilon\delta}{\tau} t \right) \qquad i = \text{V(III), V(IV)} \tag{20}$$

A similar procedure for equations (13) and (15) results in the solutions:

$$c_i^{res} = (\varepsilon\delta + 1) c_i^0 + \frac{\delta S}{F} j_{\text{app}} t - \varepsilon\delta c_i \qquad i = \text{V(II), V(V)} \tag{21}$$

and:

$$c_i = c_i^0 - \frac{S j_{\text{app}}}{\varepsilon \tilde{\varepsilon} F}\left(\frac{\varepsilon\delta + e^{-\tilde{\varepsilon} t}}{1+\varepsilon\delta} - 1 - \frac{\varepsilon\delta}{\tau} t \right) \qquad i = \text{V(II), V(V)} \tag{22}$$

To derive equations for the concentrations of water and protons, $c_{\text{H}_2\text{O}}$ and c_{H^+}, respectively, electrochemical reaction (according to equations (1) and (2)), recirculation and osmotic drag through the membrane are considered. The molar flux of water through the membrane from the positive to negative electrode on charge can be approximated by $N_{\text{H}_2\text{O}}^{drag} = n_d j_{\text{app}} / F$, where n_d is the so-called drag coefficient in the empirical model of Springer *et al.* for water transport through Nafion[48]. The water mass balances for each electrode are, therefore, as follows:

$$-\text{ve electrode (charge)}: \ \varepsilon V_e \frac{dc_{H_2O}}{dt} = \varepsilon A_{in} u(c_{H_2O}^{res} - c_{H_2O}) + A_e n_d \frac{j_{app}}{F} \tag{23}$$

$$+\text{ve electrode (charge)}: \ \varepsilon V_e \frac{dc_{H_2O}}{dt} = \varepsilon A_{in} u(c_{H_2O}^{res} - c_{H_2O}) - (A_e n_d + A_s) \frac{j_{app}}{F} \tag{24}$$

and the mass balances for the protons are:

$$-\text{ve electrode (charge)}: \ \varepsilon V_e \frac{dc_{H^+}}{dt} = \varepsilon A_{in} u(c_{H^+}^{res} - c_{H^+}) + A_e \frac{j_{app}}{F} \tag{25}$$

$$+\text{ve electrode (charge)}: \ \varepsilon V_e \frac{dc_{H^+}}{dt} = \varepsilon A_{in} u(c_{H^+}^{res} - c_{H^+}) - (A_e - 2A_s) \frac{j_{app}}{F} \tag{26}$$

The reservoir concentrations are given by (for both electrodes):

$$\frac{dc_{H_2O}^{res}}{dt} = -\frac{\varepsilon\delta}{\tau}(c_{H_2O}^{res} - c_{H_2O}) \tag{27}$$

$$\frac{dc_{H^+}^{res}}{dt} = -\frac{\varepsilon\delta}{\tau}(c_{H^+}^{res} - c_{H^+}) \tag{28}$$

Eliminating the recirculation terms in equations (by adding) (23)/(27) and equations (24)/(27), followed by integration yields:

$$c_{\mathrm{H_2O}}^{res} = (\varepsilon\delta+1)c_{\mathrm{H_2O}}^{0} - \varepsilon\delta c_{\mathrm{H_2O}} + \begin{cases} -\dfrac{j_{\mathrm{app}}}{F}\delta t\left(S+\dfrac{n_d}{w_e}\right) & +\text{ve electrode} \\ \dfrac{n_d}{w_e}\dfrac{j_{\mathrm{app}}}{F}\delta t & -\text{ve electrode} \end{cases} \tag{29}$$

in which $c_{\mathrm{H_2O}}^{0} = c_{\mathrm{H_2O}}^{res}(0) = c_{\mathrm{H_2O}}(0)$. Substituting (29) into equations (23) and (24) and solving the resulting equations leads to:

$$c_{\mathrm{H_2O}} = c_{\mathrm{H_2O}}^{0} + \begin{cases} -\dfrac{j_{\mathrm{app}}}{\varepsilon\tilde{\varepsilon}F}\left(S+\dfrac{n_d}{w_e}\right)\left(\dfrac{\varepsilon\delta+e^{-\tilde{\varepsilon}t}}{1+\varepsilon\delta}-1-\dfrac{\varepsilon\delta}{\tau}t\right) & +\text{ve electrode} \\ -\dfrac{j_{\mathrm{app}}}{\varepsilon\tilde{\varepsilon}F}\dfrac{n_d}{w_e}\left(\dfrac{\varepsilon\delta+e^{-\tilde{\varepsilon}t}}{1+\varepsilon\delta}-1-\dfrac{\varepsilon\delta}{\tau}t\right) & -\text{ve electrode} \end{cases} \tag{30}$$

A similar procedure for the proton concentrations yields:

$$c_{\mathrm{H^+}}^{res} = (\varepsilon\delta+1)c_{\mathrm{H^+}}^{0} - \varepsilon\delta c_{\mathrm{H^+}} + \begin{cases} \dfrac{j_{\mathrm{app}}}{F}\dfrac{\delta}{w_e}t\left(2Sw_e-1\right) & +\text{ve electrode} \\ \dfrac{j_{\mathrm{app}}}{F}\dfrac{\delta}{w_e}t & -\text{ve electrode} \end{cases} \tag{31}$$

where $c_{\mathrm{H^+}}^{0} = c_{\mathrm{H^+}}^{res}(0) = c_{\mathrm{H^+}}(0)$, and:

$$c_{\mathrm{H^+}} = c_{\mathrm{H^+}}^{0} + \begin{cases} \dfrac{j_{\mathrm{app}}}{\varepsilon\tilde{\varepsilon}w_eF}\left(2Sw_e-1\right)\left(\dfrac{\varepsilon\delta+e^{-\tilde{\varepsilon}t}}{1+\varepsilon\delta}-1-\dfrac{\varepsilon\delta}{\tau}t\right) & +\text{ve electrode} \\ \dfrac{j_{\mathrm{app}}}{\varepsilon\tilde{\varepsilon}w_eF}\left(\dfrac{\varepsilon\delta+e^{-\tilde{\varepsilon}t}}{1+\varepsilon\delta}-1-\dfrac{\varepsilon\delta}{\tau}t\right) & -\text{ve electrode} \end{cases} \tag{32}$$

2.4.2. Model validation and results

2.4.2.1 General observations and formulae

Before presenting the simulations, it is worthwhile making some general observations regarding the solutions derived above, in the context of a typical test cell. Formulae are derived to provide useful guidelines for the operation of VRFB cells under practical operating conditions.

In the realistic limit $\delta \to 0$, i.e., $V_r \gg V_e$, the term $Sj_{\text{app}}/(\varepsilon\tilde{\varepsilon}F)$ in the solutions (20) for the V(II)/V(III) concentrations can be approximated by $h_e\, Sj_{\text{app}}/(\varepsilon u F)$. The practical range for $u/h_e = 1/\tau$ in a test cell is 0.1–0.01 (higher values can lead to leaking of the electrolyte and lower values to low charge efficiencies). Returning to equations (20), it can be seen that for $t \ll 1/\tilde{\varepsilon} = O(\tau)$, the asymptotic form of the concentrations is given by:

$$c_i \sim c_i^0 - \frac{Sj_{\text{app}}}{\varepsilon F} t\left(1 - \frac{t}{2\tau}\right) \qquad (t \ll \tau) \tag{33}$$

For $t \gg \tau$, the exponential term in (20) can be disregarded and the asymptotic forms are:

$$c_i \sim c_i^0 - S\frac{j_{\text{app}}}{\varepsilon F}(\tau + \varepsilon\delta t) \qquad (t \gg \tau) \tag{34}$$

Likewise, the proton concentration in the positive electrode (required below) can be approximated as:

$$c_{\text{H}^+} \sim c_{\text{H}^+}^0 - \frac{j_{\text{app}}}{\varepsilon w_e F}(2Sw_e - 1)(\tau + \varepsilon\delta t) \qquad (t \gg \tau) \tag{35}$$

Thus, there are distinct stages in the charge cycle: an initial stage of $O(\tau)$ (about 1 min using the parameter values in Tables 2.2–2.4) during which the electrode concentrations of V(II) and V(III) decrease at a linear rate $Sj_{\text{app}}/\varepsilon F$ in t, followed by an intermediate stage with $t = O(\tau)$; in a final stage, defined by $t \gg \tau$ (the majority of the charge cycle), the rate of depletion reduces considerably to $\delta Sj_{\text{app}}/\varepsilon F$, again linearly in t. During the intermediate stage, the variation in the concentrations is quadratic, as is seen by passing to the limit $t \to \tau$ in equation (33). For low initial concentrations or high currents, the first two stages will dominate by virtue of the short charge time. Such scenarios exist only under extreme conditions and are not representative of the experiments presented in this section. The asymptotic behaviour described above is verified in section 2.4.2.2 (Figure 2.10)

To estimate the time taken to fully charge, t_{fc}, it is defined as the time taken to reach a zero concentration of the V(III) reactant in the negative electrode ($c_{\text{V(III)}} = 0$) or of the V(IV) reactant in the positive electrode ($c_{\text{V(IV)}} = 0$). Equation (15) show that these conditions are equivalent if the initial concentrations of V(IV) and V(III) are equal. Making the approximations $\delta \to 0$ and $e^{-\tilde{\varepsilon}t} = 0$ in equation (20), for the reasons outlined above, the condition $c_{\text{V(III)}} = 0$ leads to:

$$t_{fc} \approx \frac{V_r}{V_e}\left(\frac{Fc^0_{\text{V(III)}}}{Sj_{\text{app}}} - \frac{h_e/u}{\varepsilon}\right) \tag{36}$$

Equation (35) shows that the charge time can be controlled by several means. It can be increased by increasing the reservoir volume, V_r or decreasing the electrode volume, V_e, with all other parameters in equation (36) fixed in each case. It is interesting to note that

while $t_{fc} \propto V_r$, it is inversely proportional to V_e. In the first case, the total vanadium content is increased and in the latter case the residence time for reaction is decreased, both of which lead to longer charge times (to an equivalent SoC). Alternatively, the initial concentration of vanadium, $c^0_{\mathrm{V(III)}}$ can be increased or the volumetric current density, Sj_{app} decreased in order to increase t_{fc}. In the latter scenario, the available surface area for reaction or the bulk reaction rates are decreased. The ratio $h_e/u = \tau$, measuring the residence time for reaction, can also be used to control the charge time; clearly a decrease in h_e or an increase in u, both of which will lead to a decrease in τ, will increase t_{fc}.

The state of charge of the cell is a key parameter for ensuring the operation remains with a safe range, particularly with regard to gas-evolving reactions. There are several methods for estimating the SoC of a battery, with one of the most common methods based on the open-circuit voltage (OCV). For certain ranges of the SoC, the relationship between the OCV and SoC can be approximated as linear: $\mathrm{SoC} = \alpha_1 + \alpha_2 \mathrm{OCV}$, for constants α_1 and α_2 that are determined by the OCV values at full and zero capacity[49]. These extreme values of the OCV, which can be measured, are denoted $E_{\max}$ and $E_{\min}$, corresponding respectively to $\mathrm{SoC} = 1$ and $\mathrm{SoC} = 0$. Inserting these values into the expression for SoC gives $\alpha_1 = -E_{\min}/(E_{\max} - E_{\min})$ and $\alpha_2 = 1/(E_{\max} - E_{\min})$. Subsequently inserting these expression and equations (20) and (22) into equation (4) leads to (converting the proton concentration to mol dm^{-3}):

$$\mathrm{SoC}(t) = -\frac{E_{\min}}{E_{\max} - E_{\min}} + \frac{E^0}{E_{\max} - E_{\min}} + \frac{2RT}{F(E_{\max} - E_{\min})} \ln\left(\frac{c^0_{\mathrm{V(III)}} + \xi(t)}{c^0_{\mathrm{V(II)}} - \xi(t)} \right) + \frac{4.6RT}{F(E_{\max} - E_{\min})} \left\{ \log_{10}\left(c^0_{\mathrm{H^+}} + \left[\frac{2Sw_e - 1}{Sw_e} \right] \xi(t) \right) - 3 \right\} \tag{37}$$

since $c^0_{\mathrm{V(IV)}} = c^0_{\mathrm{V(III)}}$ and $c^0_{\mathrm{V(II)}} = c^0_{\mathrm{V(V)}}$.(that last term includes the factor of 10^{-3} that is introduced when converting $c_{\mathrm{H^+}}$ to units of mol dm^{-3}, noting that $\log_{10}(10^{-3}) = -3$). The function $\xi(t)$ is given by:

$$\xi(t) = \frac{Sj_{\mathrm{app}}}{\varepsilon\tilde{\varepsilon}F}\left(\frac{\varepsilon\delta + e^{-\tilde{\varepsilon}t}}{1+\varepsilon\delta} - 1 - \frac{\varepsilon\delta}{\tau}t\right) \tag{38}$$

For $\delta \ll 1$ and $t \gg \tau$, equation (37) can be simplified to:

$$\begin{aligned}\mathrm{SoC}(t) \sim & -\frac{E_{\min}}{E_{\max}-E_{\min}} + \frac{E^0}{E_{\max}-E_{\min}} + \frac{2RT}{F(E_{\max}-E_{\min})}\ln\left(\frac{c^0_{\mathrm{V(III)}} - \varsigma(t)}{c^0_{\mathrm{V(II)}} + \varsigma(t)}\right) \\ & + \frac{4.6RT}{F(E_{\max}-E_{\min})}\left\{\log_{10}\left(c^0_{\mathrm{H^+}} - \left[\frac{2Sw_e - 1}{Sw_e}\right]\varsigma(t)\right) - 3\right\}\end{aligned} \tag{39}$$

since $c_{\mathrm{V(V)}} = c_{\mathrm{V(II)}} \sim c^0_{\mathrm{V(II)}} + Sj_{\mathrm{app}}\left(\tau + \varepsilon\delta t\right)/F$ for $t \gg \tau$. In equation (39), $\varsigma(t)$ is given by:

$$\varsigma(t) = \frac{Sj_{\mathrm{app}}}{\varepsilon F}\left(\tau + \varepsilon\delta t\right) \tag{40}$$

Equation (39), which is a function only of time, is valid for the majority of a typical charge cycle. It provides a convenient first-order approximation to the SoC under practical conditions. Alternatively, the more complex, but still relatively straightforward expression (37) can be used.

2.4.2.2 Simulations

The charge/discharge curves for the experiments described in section 2.2.1 were simulated using the analytical solutions derived above. The default parameters are given in Tables 2.2–2.4. The initial concentrations of the vanadium species (Table 2.4) i.e. at the beginning of charge, were such that a 5 % of the total vanadium concentration was considered to be in the V(II) state in the negative electrode and in the V(V) state in the positive electrode. Equation (4) was used to control the charge and discharge time; as in the experiment, the OCV with respect to the cell reactant concentrations was cycled between 1.3 V (beginning of charge/end of discharge) and 1.5 V (end of charge).

Symbol	Description	Value
E_1^0	Reference potential for reaction (1)	–0.26 V
E_2^0	Reference potential for reaction (2)	1.004 V
$k_{1,ref}$	Reference rate constant at for reaction (1) at 293 K[†]	3.56×10^{-6} m s^{-1}
$k_{2,ref}$	Reference rate constant for reaction (2) at 293 K[50]	3×10^{-9} m s^{-1}
σ_c	Electronic conductivity of the graphite current collector	9.1×10^{4} S m^{-1}
σ_e	Ionic conductivity of the electrolyte (both half cells)[†]	100 S m^{-1}

Table 2.2: Default values for the electrochemical parameters and conductivities.

[†]Fitted parameter

The initial concentrations were estimated from the experimental conditions, along with the assumption that sulphuric acid dissociates completely in water (based on the value of the dissociation constant). In the discussion below, the electrolyte flow rate, ω is specified rather than the velocity. The conversion is given by $\omega = \varepsilon u A_{in}$.

As with all models, it was necessary to fit certain parameters in order to match the experimental results. The fitting parameters (kept to a minimum) were (i) the specific surface area *S*, (ii) the electrolyte conductivities σ_e, and the rate constant $k_{1,ref}$, given in equation (8). The first of these parameters is very difficult to determine and the estimates can vary by orders of magnitude. The electrolyte conductivities for the particular system were not known, so were used as free parameters for fitting purposes. For simplicity, the values were set equal for both half cells. The final fitting parameter is also unknown for the present system. The fitted value is, however, consistent with previous reports[41-44]. We point out that the fitting of parameters was performed only once, using the base-case parameter values in Tables 2.2 to 2.4

Symbol	Description	Value
w_m	Width of the membrane	1.25×10^{-4} m (125 μm)
w_e	Width of the electrode	0.004 m
w_c	Width of the current collector	0.005 m
b_e	Breadth of the electrode	0.1 m
h_e	Height of the electrode	0.1 m
ε	Porosity of the electrode	0.67
V_r	Volume of electrolyte in the reservoir	2.232×10^{-4} m^3
S	Specific surface area for reaction†	420 m^{-1}

Table 2.3: Default values for the structural and geometric parameters.

†Fitted parameter

Fig 2.9 shows the result of simulations at two different concentrations of vanadium, with other parameters as in Table 2.2. A comparison to experimental data is also provided. The

analytical solutions capture the charge-discharge behaviour well, particularly with respect to the trends observed. The best fit over all parameter variations (see also Fig 2.11) could not eliminate all quantitative discrepancies, although theses discrepancies are relatively small. The model does not consider gas evolving reactions and self discharge, which lower the charge efficiency in the real case. Furthermore, as seen in Fig 2.9, there is a small discrepancy of approximately 0.03 V between the potential difference across the monitoring cell and the true OCV (≈ 1.53 V) in both cases. The model charge time is controlled by the attainment of an OCV of 1.5 V, which leads to the small discrepancy between the model and experimental cell-voltage curves at open-circuit conditions.

Symbol	**Description**	**Value**
T	Temperature	300 K
$c^0_{V(II)}$	Initial V(II) concentration	0.06 mol dm^{-3}
$c^0_{V(III)}$	Initial V(III) concentration	1.140 mol dm^{-3}
$c^0_{V(IV)}$	Initial V(IV) concentation	1.140 mol dm^{-3}
$c^0_{V(V)}$	Initial V(V) concentration	0.060 mol dm^{-3}
j_{app}	Current density	100 mA cm^{-2}
$c^0_{H^+}$	Initial concentration of protons	4.2 mol dm^{-3}
$c^0_{H_2O}$	Initial concentration of water	4.23 mol dm^{-3}
ω	Linear flow rate of the electrolyte	1 cm^3 s^{-1}

Table2.4: Default values for the operating parameters.

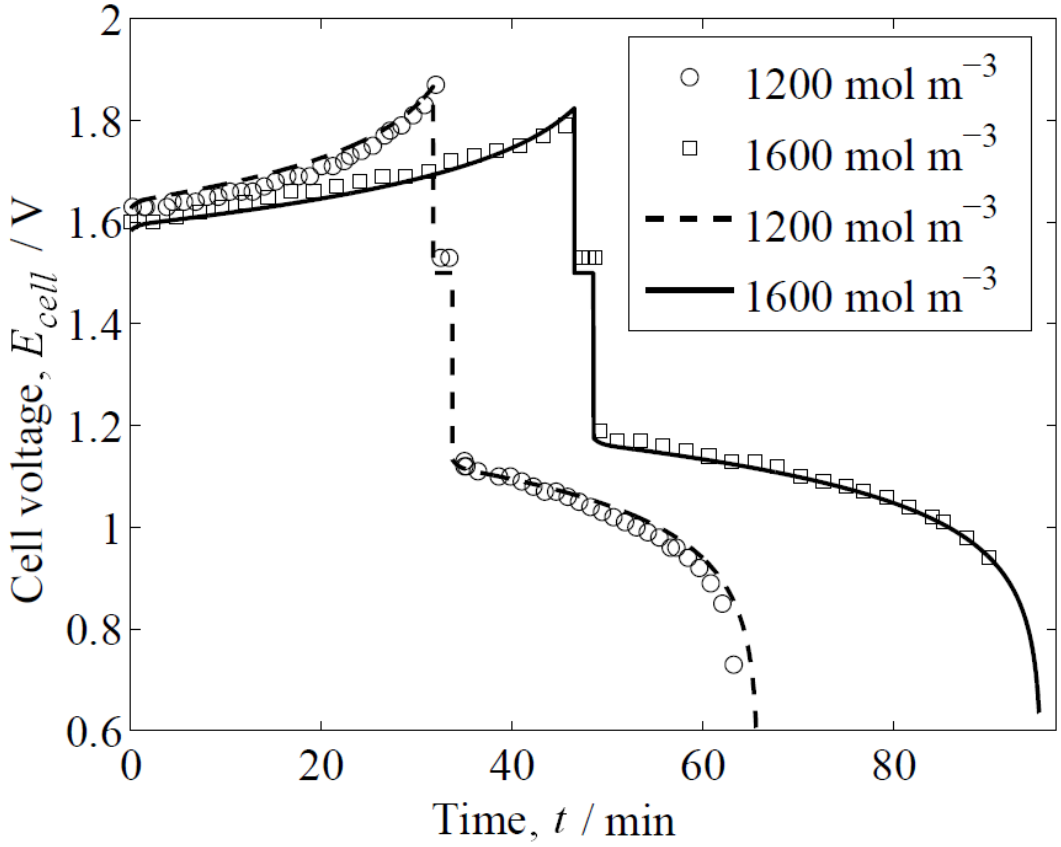

Fig 2.9: Comparison between experimental and analytical charge/discharge curves at two different vanadium concentrations using a 100 cm^2 VRFB test cell at 300 K with a flow rate of 1 $cm^{-3}s^{-1}$ and at 100 mA cm^{-2}current density.

A comparison of the full analytical solution for the V(III) concentration (equation (20)) and the asymptotic solutions given by equations (33) and (34) is provided in Fig 2.10. The time is truncated at 14 min of charging in order that a clear comparison can be made. The asymptotic solutions predict the full solution accurately. The full solutions also exhibit the three-stage process described in section 2.4.2.1, with equations (33) and (34) capturing the first and last of the stages.

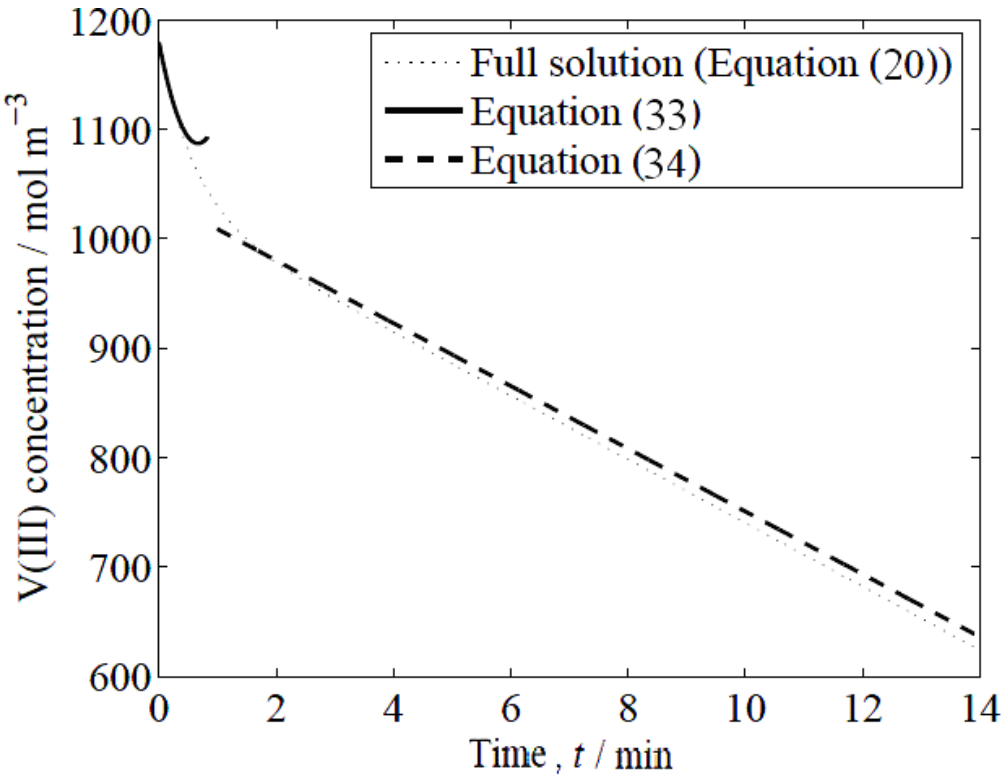

Fig 2.10: A comparison of the full analytical solution for the V(III) species concentration (equation (20)) and the asymptotic solutions given by equations (33) and (34). The cell temperature was 300 K, the vanadium concentration was 1.2 mol dm^{-3}, the flow rate was 1 cm^{3}s^{-1} and the current density was 100 mA cm^{-2}.

The effects of variations in the flow rate ω can be seen in Fig 2.11. In both simulations, each electrode/reservoir possessed a total vanadium concentration of 1.2 mol dm^{-3}. Experimental charge-discharge curves are provided for comparison. The simulated and experimental curves are again in good agreement, with a longer charge time and higher terminal cell voltage on charge (to the equivalent SoC) for the higher flow rate of 2 cm^{3}s^{-1}. The longer charge time is a direct result of the decreased residence time for reaction, as discussed in the previous section.

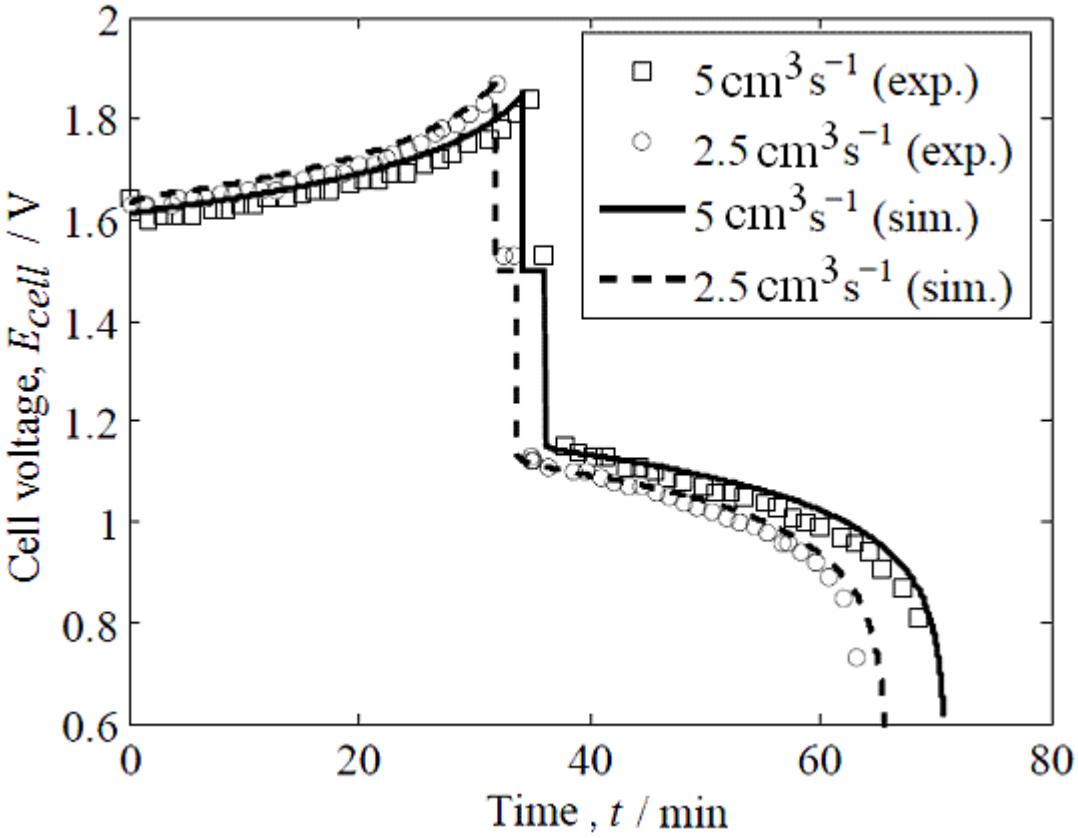

Fig 2.11: Comparison between experimental and analytical charge/discharge curves at two different volumetric electrolyte flow rates using a 100 cm^2 VRFB test cell at 300 K with total vanadium concentration was 1.2 mol dm^{-3} and at a of current density 100 mA cm^{-2}.

The final result is depicted in Fig 2.12, which shows simulated charge/discharge curves for three system temperatures. In all cases the vanadium concentration was 1.2 mol dm^{-3}, the flow rate was 1 cm^3s^{-1} and the current density was 100 mA cm^{-2}. The deviation of the cell voltage from the equilibrium value decreases as the temperature is increased. The capacity of the battery (proportional to time since the discharge current is constant) increases mildly with increased temperature. An increased temperature increases the rate constants (7) and (15), which leads to decreases in the magnitudes of the overpotentials (12) and (6); note that these decreases dominate any increases due to the algebraic factor. Moreover, the membrane conductivity, which is given by equation (11), increases exponentially with temperature. Therefore, as the temperature is increased, the ohmic loss across the membrane decreases, which in turn decreases the deviation from the OCV.

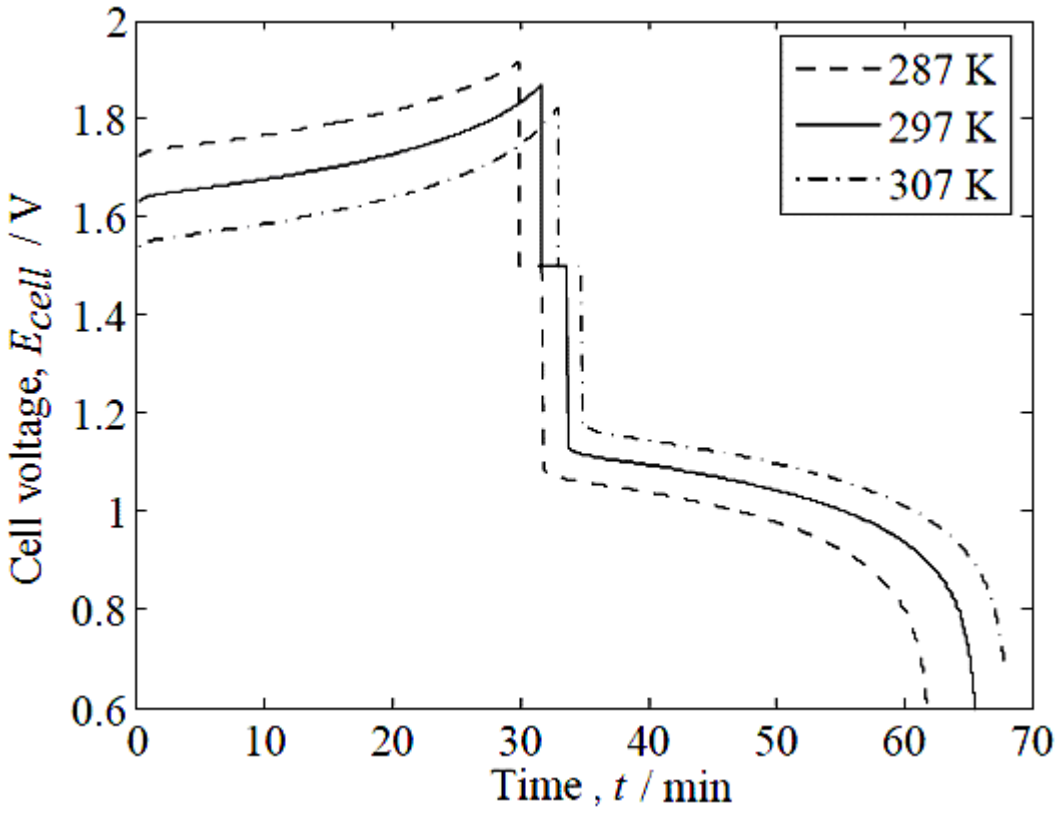

Fig 2.12: Simulated charge/discharge curves for a range of system temperatures where the vanadium concentration was 1.2 mol dm^{-3}, the flow rate was 1 cm^3s^{-1} and the current density was 100 mA cm^{-2}, in all cases.

2.5. Conclusions and further work

The effects of flow rate, vanadium concentration and current density on the performance of a VRFB have been investigated. Charge-discharge experiments at a variety of flow rates and applied currents in solutions containing 1.1 mol dm^{-3} and 1.5 mol dm^{-3} vanadium concentrations demonstrated that extremely high charge efficiencies are possible (approaching 95 % in most cases). A minimum of 10 cycles and a maximum of 30 cycles were performed in each test, with no decreases in the cell efficiencies all cases reported.

At a vanadium concentration of 1.1 mol dm^{-3}, the best flow rate was found to be in the range 1.5–3 cm^3s^{-1}, while at 1.5 mol dm^{-3}, the best performance (highest overall efficiency) was found to be at 1.5 cm^3s^{-1}. Higher flow rates had a slightly detrimental

effect on the efficiencies. In fact, the differences in the efficiency values between 0.5 and 1.5 cm^3s^{-1} were small, implying that operating the system at 0.5 cm^3s^{-1} would be cost effective when the total power consumption is considered. The 1.1 mol dm^{-3} solution also exhibited significantly higher activation/concentration polarisation up to a reasonably high flow rate. Operating with this concentration therefore requires more power to achieve good performance and to avoid component degradation as a result of high local potentials. The charge and discharge currents can greatly affect the efficiency of the cell. One noteworthy result is the ability of the system to establish stable cycling when the current is changed.

The development of practical modelling tools for RFBs is an important consideration for the design, control and monitoring of systems. Hence, in this chapter a control-oriented model for the all-vanadium flow battery has been developed, based on the major components of voltage loss and taking into account the electrode kinetics and recirculation of the half-cell electrolytes. The model is able to relate important characteristics of performance (such as the time to charge/discharge and the state of charge) to key system properties. Simulations have demonstrated that the model is able to capture the performance in practical systems to a high degree of accuracy. The model developed can readily be extended to other vanadium RFBs (e.g. vanadium-bromide). It can also be used as the basis for a stack model of these systems. The present model can also be extended to include temperature effects and coupling between cells arranged in parallel and series, with further validation against experimental data.

References:

[1]. M. Skyllas-Kazacos, "A*n Historical Overview of the Vanadium Redox Flowbattery Development at the University of New South Wales, Australia*", University of New South Wales, NSW, Australia 2052.

[2]. E. Sum, M. Rychcik, M. Skyllas-Kazacos, *J. Power Sourc.*, **16** (1985) 85.

[3]. E. Sum, M. Skyllas-Kazacos, *J. Power Sourc.*, **15** (1985) 179.

[4]. Ch. Fabjan, J. Garche, B. Harrer, L. Jörissen, C. Kolbeck, F. Philippi, G. Tomazic, F. Wagner, *Electrochim. Acta*, **47** (2001) 825.

[5]. L. Joerissen, J. Garche, Ch. Fabjan, G. Tomazic, *J. Power Sourc.*, **127** (2004) 98.

[6]. S. Eckroad, H. Kamath, S. Rajagopalan *Vanadium Redox Flow Batteries - An In-Depth Analysis (Technical Update)*, Electric Power Research Institute, Palo Alto, California, March 2007.

[7]. Y. Nakayama, S. Takahashi, K. Hirakawa, Y. Yamaguchi, *J. Power Sourc.,***125** (2004) 135.

[8]. M. Skyllas-Kazacos, F. Grossmith, *J. Electrochem. Soc*., **134** (1987) 2950.

[9]. M. Gattrell, J. Park, B. MacDougall, J. Apte, S. McCarthy, C.W. Wu, *J. Electrochem. Soc.*, **151** (2004) 123.

[10]. T. D. J. Hennessy, *US Patent 7265456*, VRB Power systems Inc. http://www.patentstorm.us/patents/7265456.html, accessed on April 24, 2011.

[11]. M. Chris, H. DunRui, M. Kazacos, M. Skyllas-Kazacos, "*Vanadium Battery Solar Demonstration House*". http://www.vrb.unsw.edu.au/solar.htm, accessed on April 24, 2011.

[12]. L. Joerissen, G. Juergen, Ch. Fabjan, G. Tomazic, *J. Power Sourc.*, **127** (2004) 98.

[13]. J. Davis, "*Advantages of using Vanadium Redox Batteries in Telecommunications Prime Power Sites"*, VRB Power Systems, Inc., Vancouver B.C. V7Y1C6 Canada. http://www.vrbpower.com/docs/whitepapers, accessed on April 24, 2011

[14]. B.T. Sun, M. Skyllas-Kazacos, *Electrochim. Acta*, **36** (1991) 513.

[15]. M. Kazacos, M. Cheng, M. Skyllas-Kazacos, *J. Appl. Electrochem.* , **20** (1990) 463.

[16]. M. Skyllas-Kazacos, C. Menictas, M. Kazacos, *J. Electrochem. Soc.* , **143** (1996) 86.

[17]. M. Skyllas-Kazacos, M. Rychcik, R.G. Robins, A.G. Fane, M. Green, *J. Electrochem. Soc.* , **133** (1986) 1057.

[18]. S. Zhong, M. Skyllas-Kazacos, *J. Power Sourc.*, **39** (1992) 1.

[19]. T. Mohammadi, M. Skyllas-Kazacos, *J. Appl. Electrochem.*, **27** (1996) 153.

[20]. B.T. Sun, M. Skyllas-Kazacos, *Electrochim. Acta*, **37** (1992) 1253.

[21]. M. Skyllas-Kazacos, M. Rychcik, *J. Power Sourc.*, **19** (1987) 45.

[22]. B. Tian, C. W. Yan, F.H. Wang, *J. Membr. Sci.* , **234** (2004) 51.

[23]. B. Tian, C. W. Yan, F.H. Wang, *J. Appl. Electrochem.* , **34** (2004) 1205.

[24]. J. Xi, Z. Wu, X. Qiu, L. Chen, *J. Power Sourc.*, **166** (2007) 531.

[25]. M. Skyllas-Kazacos, F. Grossmith, *J. Electrochem. Soc.* , **134** (1987) 2950.

[26]. T. Mohammadi, M. Skyllas-Kazacos, *J. Membr.Sci.*, **98** (1995) 77.

[27]. T. Sukkar, M. Skyllas-Kazacos, *J. Appl. Electrochem.*, **34** (2004) 137.

[28]. G. Oriji, Y. Katayama, T. Miura, *Electrochim. Acta*, **49** 2004) 3091 .

[29]. M. Kazacos, M. Skyllas-Kazacos, *J. Electrochem. Soc.*, **136** (1989) 2759.

[30]. X. Lu, *Electrochim. Acta*, **46** (2001) 4281.

[31]. S. Zhong, M. Kazacos, R.P. Burford, M. Skyllas-Kazacos, *J. Power Sourc.*, **36** (1991) 29.

[32]. V. Haddadi-Asl, M. Kazacos, M. Skyllas-Kazacos, *J. Appl. Electrochem.*, **25** (1995) 29.

[33]. A.A. Shah, M.J. Watt-Smith, F.C. Walsh, *Electrochim. Acta*, **53** (2008) 8087.

[34]. H. Al-Fetlawi, A.A. Shah, F.C. Walsh, *Electrochim. Acta*, **55** (2009) 78.

[35]. A.A. Shah, H. Al-Fetlawi, F.C. Walsh, *Electrochim. Acta*, **55** (2010) 1125.

[36]. H. Al-Fetlawi, A.A. Shah, F.C. Walsh, *Electrochim. Acta* **55** (2010) 3192.

[37]. A.A. Shah, F.C. Walsh, *J. Power Sourc.*, **185** (2008) 287.

[38]. A.A. Shah, T.R. Ralph, F.C. Walsh, *J. Electrochem Soc.*, **156** (2009) B465.

[39]. C.Y. Wang, W.B. Gu, B.Y. Liaw, *J. Electrochem. Soc.*, **145** (1998) 3407.

[40]. T. I. Evans, T. V. Nguyen, R.E. White, *J. Electrochem. Soc.*, **136** (1989) 328.

[41]. M. Li, T. Hikihara, *IEICE Trans. Fundamentals*, **E91-A(7)**, (2008) 1741.

[42]. D.P. Scamman, G.W. Reade, E.P.L. Roberts, *J. Power Sourc.*, **189** (2009) 1220.

[43]. D.P. Scamman, G.W. Reade, E.P.L. Roberts, *J. Power Sourc.*, **189** (2009) 1231.

[44]. S.G. Bratsch, *J. Phys. Chem. Ref. Data,* **18** (1989) 1.

[45]. C.V. Chrysikopoulos, P.Y. Hsuan, M.M. Fyrillas, K.Y. Lee., *J. Hazard Mater.*, **97** (2003) 245.

[46]. J. Newman *Electrochemical Systems*; Prentice Hall: Engelwood Cliffs, NJ (1991).

[47]. S.G. Bratsch, *J. Phys. Chem. Ref. Data*, **18** (1989) 1.

[48]. T. Springer, T. Zawodzinski, S. Gottesfeld, *J. Electrochem. Soc.* , **138** (1991) 2334.

[49]. *Handbook of Batteries*; 3rd ed.; D. Linden, T.B. Reddy, Eds.; McGraw-Hill: NY, 2002.

[50]. T.A. Zawodzinski, C. Derouin, S. Radzinski, R.J. Sherman, V.T. Smith, T.E. Springer, S. Gottesfeld, *J Electrochem. Soc.*, **140** (1993) 1041.

Chapter -III

The Soluble Lead-Acid Flow Battery

3.1. Introduction

Traditional lead-acid batteries are used in automobiles due to their reliability and ability to deliver a high current for short periods of time. They are also used in stationary power applications as secondary batteries and as large-scale energy storage systems[1]. Metallic lead is used in the electroplating industry and for the manufacture of lead-tin, lead-cobalt, lead-nickel and lead-copper[2]. It is also used in the semiconductor industry for the deposition of PbS[3], as well in PCB (printed circuit board) manufacture[2].

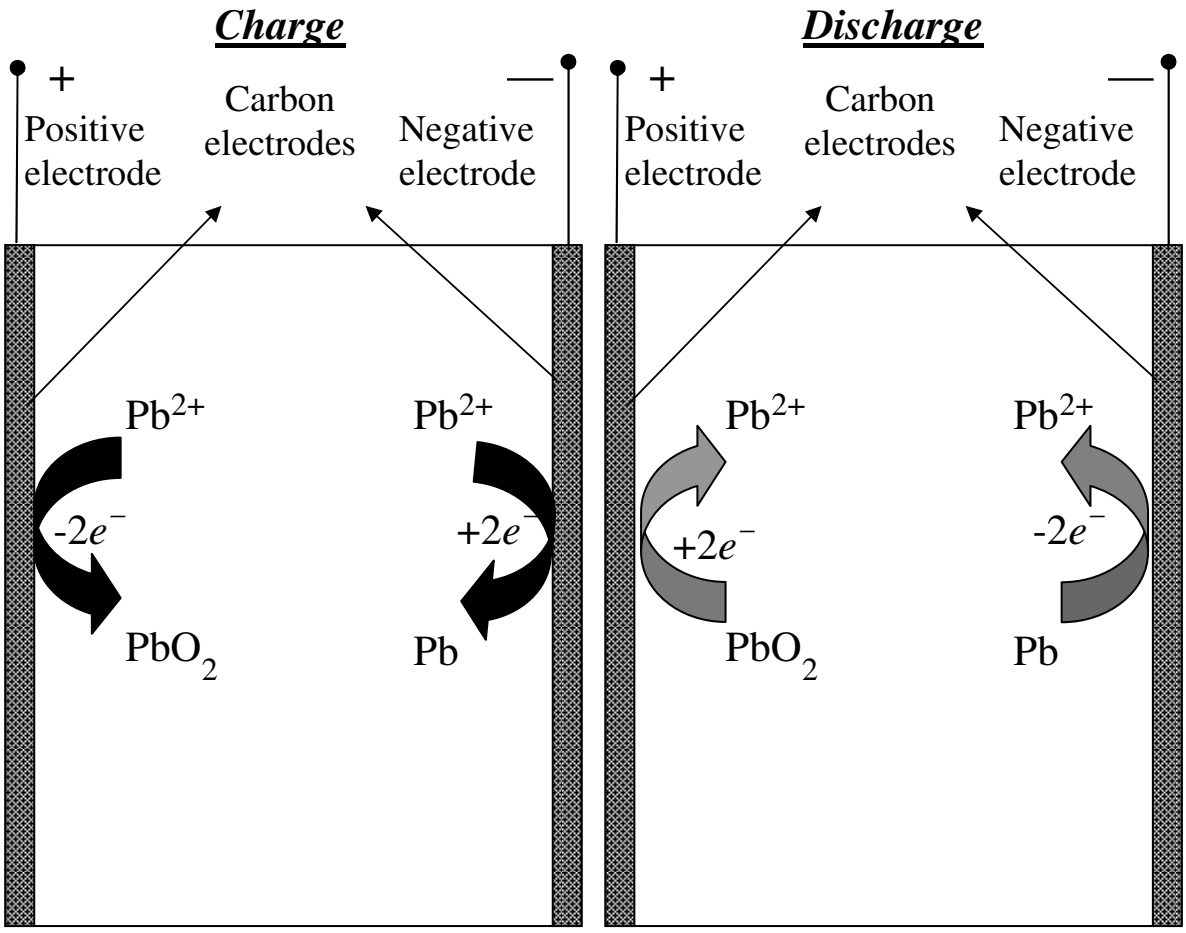

Fig 3.1: Schematic diagram showing the charge-discharge of an undivided soluble lead-acid cell.

The open circuit voltage of the traditional lead acid battery (per cell at full charge) is around 2.10 V[5]. The acidic medium for these lead acid batteries is sulfuric acid (H_2SO_4)[4]; the cell reaction is:

$$Pb + PbO_2 + 2H_2SO_4 \underset{\text{discharge}}{\overset{\text{charge}}{\rightleftharpoons}} 2PbSO_4 + 2H_2O \quad (1)$$

Due to its environmental friendly nature and the solubility of the lead ions (2 mol dm^{-3})[2,6] in methanesulfonic acid (MSA), in this chapter the concept of lead (II) in methanesulfonic acid[7] (as the electrolyte) was investigated for use in a soluble lead-acid flow battery. The positive and negative electrode reactions respectively can be written as:

$$Pb^{2+} + 2H_2O - 2e^- \underset{\text{discharge}}{\overset{\text{charge}}{\rightleftharpoons}} PbO_2 + 4H^+ \qquad E^0 = +1.70\ V\ vs.\ \text{SHE} \quad (2)$$

$$Pb^{2+} + 2e^- \underset{\text{discharge}}{\overset{\text{charge}}{\rightleftharpoons}} Pb \qquad E^0 = -0.13\ V\ vs.\ \text{SHE} \quad (3)$$

Lead and lead dioxide are deposited on the positive and negative electrodes, respectively, during charge (as shown Fig 3.1). Hence the active materials are converted from soluble chemical species to solid electrodeposits. This principle was initially tested and proven by Pletcher and Wills et al.[7-13] in a series of experiments conducted from the fundamental electrochemical level to the level of a small-scale cell (2 cm^2). The initial experiments also showed that the electrode kinetics of the Pb^{2+}/PbO_2 couple were slow compared to the Pb^{2+}/Pb kinetics. The overpotential associated with the positive electrode is also large [13]. Towards the end of charge, the electrolyte is depleted of the lead ions and secondary reactions take place, namely electrolysis of water. This reaction causes the production of hydrogen and oxygen at the negative and positive electrodes, respectively, which lead to inefficiencies in the cell.

$$2H^+ + 2e^- \rightarrow H_2 \uparrow \qquad E^0 = -0.83\ V\ vs.\ \text{SHE} \quad (4)$$

$$H_2O - 2e^- \rightarrow \frac{1}{2}O_2 \uparrow + 2H^+ \qquad E^0 = +1.23\ V\ vs.\ \text{SHE} \quad (5)$$

3.2 Experimental arrangement

3.2.1. Test cell construction

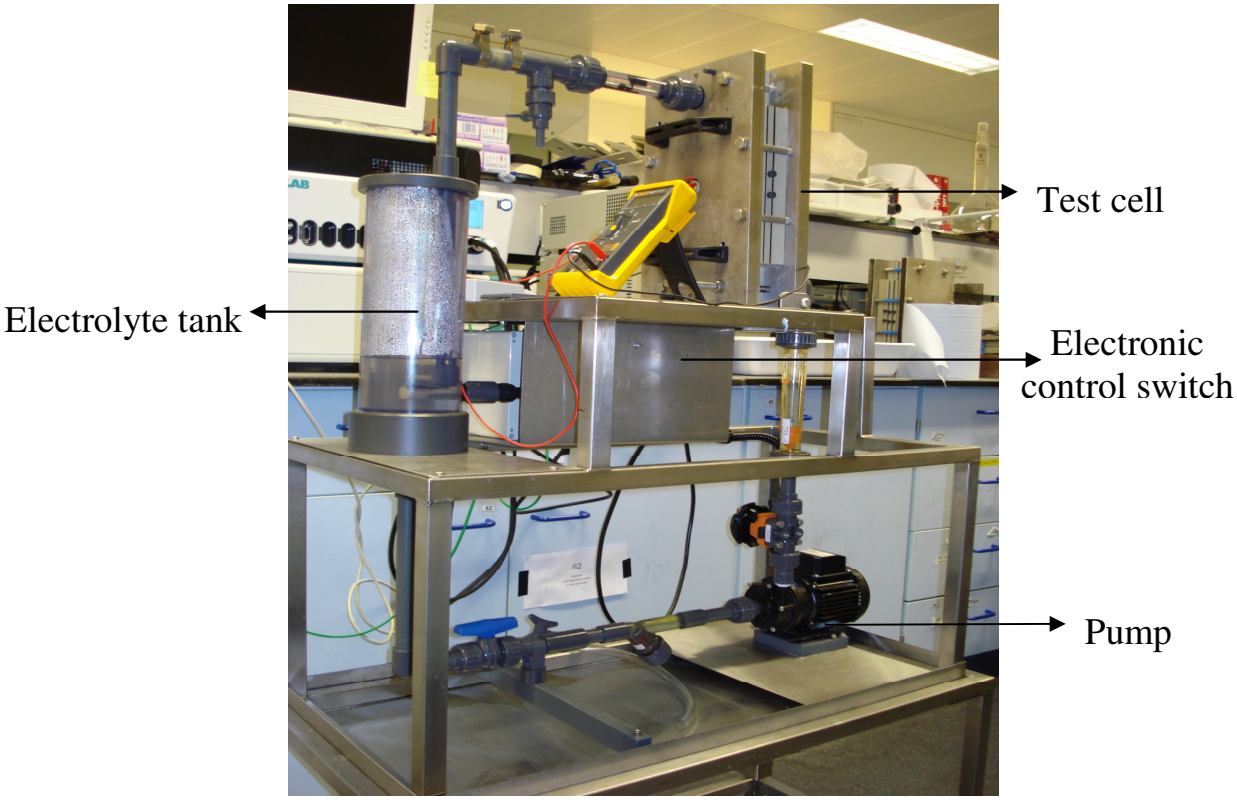

Fig 3.2: Photograph showing the overall construction of the flow system for soluble lead-acid battery studies.

All the experiments reported in this chapter were performed using a custom-made flow rig. The flow circuit (Fig 3.2) was interconnected using a 25 mm diameter polypropylene pipe from a 3.5 dm^3 cylindrical reservoir via a magnetically coupled pump (Totton Pumps, type T113095), a flow meter (100–1000 dm^3 h^{-1}) and a flow control valve (Georg Fischer GmbH). The motor connected to the power source was controlled by a safety relay in the reservoir, which automatically switches off the pump in the case of a drop in the reservoir electrolyte volume.

The test cell was fabricated from a series of polypropylene blocks (360 mm × 170 mm × 10 mm). The outer blocks had copper plates acing as (100 mm × 100 mm × 3 mm) current

collectors embedded into them so that the surface was level with the surface of the polymer block. The next blocks housed the electrode materials. Both electrodes were 130 mm × 130 mm plates (of carbon, nickel or graphite), which were housed in polypropylene frames with internal dimensions of 130 mm × 130 mm and the same thicknesses as the electrode plates, whilst the active areas were restricted to 100 mm × 100 mm by the frames. Insulating self-adhesive tape (polyester tape, Cole Parmer®) was used to ensure that the copper current contacts were not exposed to the acidic electrolyte. The electrolyte chamber frame had dimensions of 360 mm × 170 mm × 10 mm and the reaction chamber itself was 180 mm × 100 mm × 12 mm. The design allowed inlet and outlet flow distributors (made of polypropylene) to be slotted into the electrolyte frame (Fig 3.3 and Fig 3.4).

This arrangement allowed testing of various designs of flow distributor, including variations in the shape of the inlet/exit zones, inclusion of turbulence promoters, vanes and current shields. The size of the cell stacks could also be varied. Holes were drilled into the sides of the electrolyte flow distributor frames in order to allow a Luggin tube to be inserted for monitoring the individual electrode potentials *vs.* a reference electrode. An EPDM (Klinger) gasket (360 mm × 170 mm × 1 mm) was placed between the electrode frame and the electrolyte compartment with 100 mm × 100 mm sections (with inlet/outlet ports) or 180 mm × 100 mm sections (without inlet/outlet ports) cut from the centre. This formed a total inter-electrode gap of 12 mm.

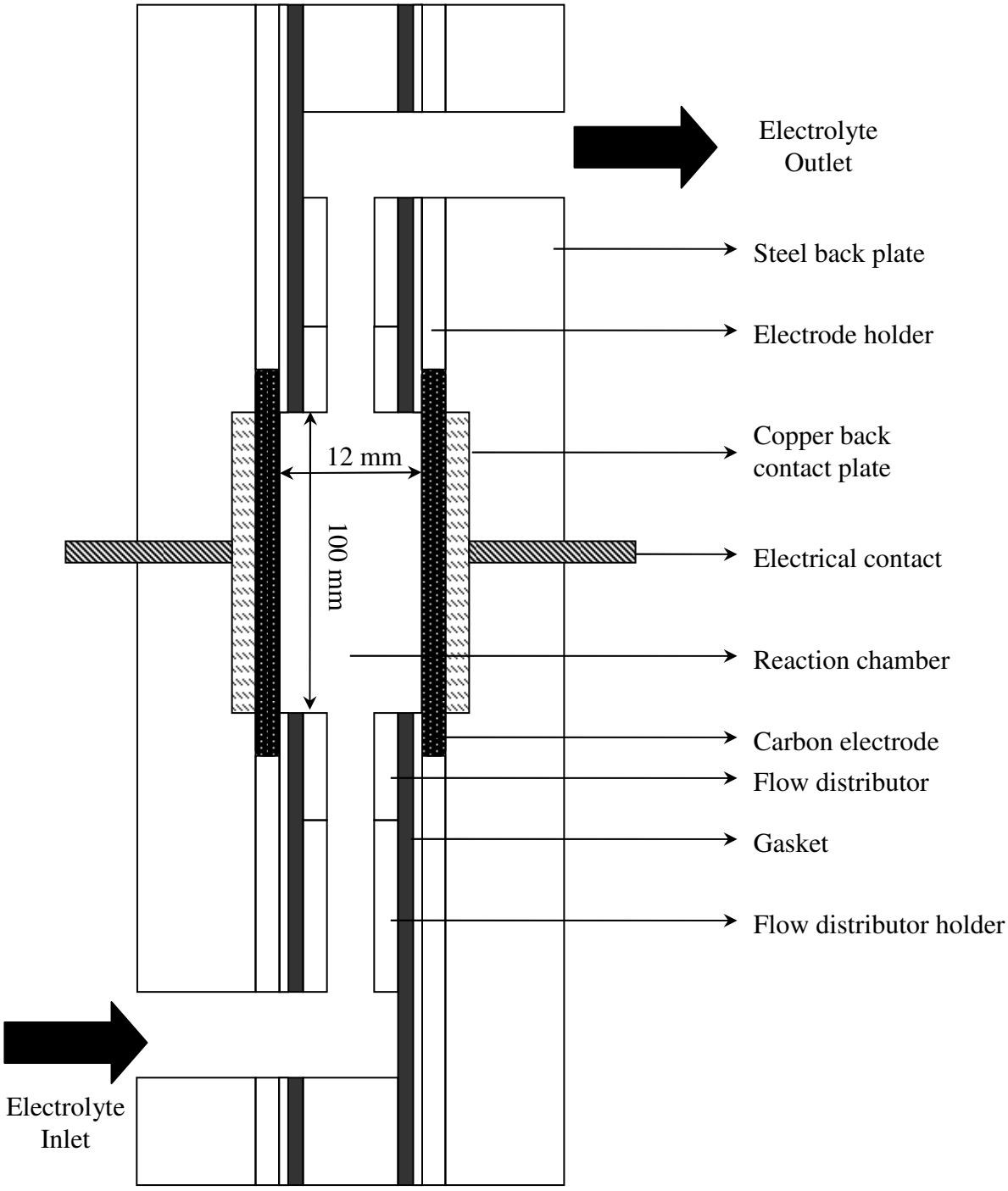

Fig 3.3: Figure showing the cross-sectional view of the 100 cm^2 soluble lead acid flow battery test cell.

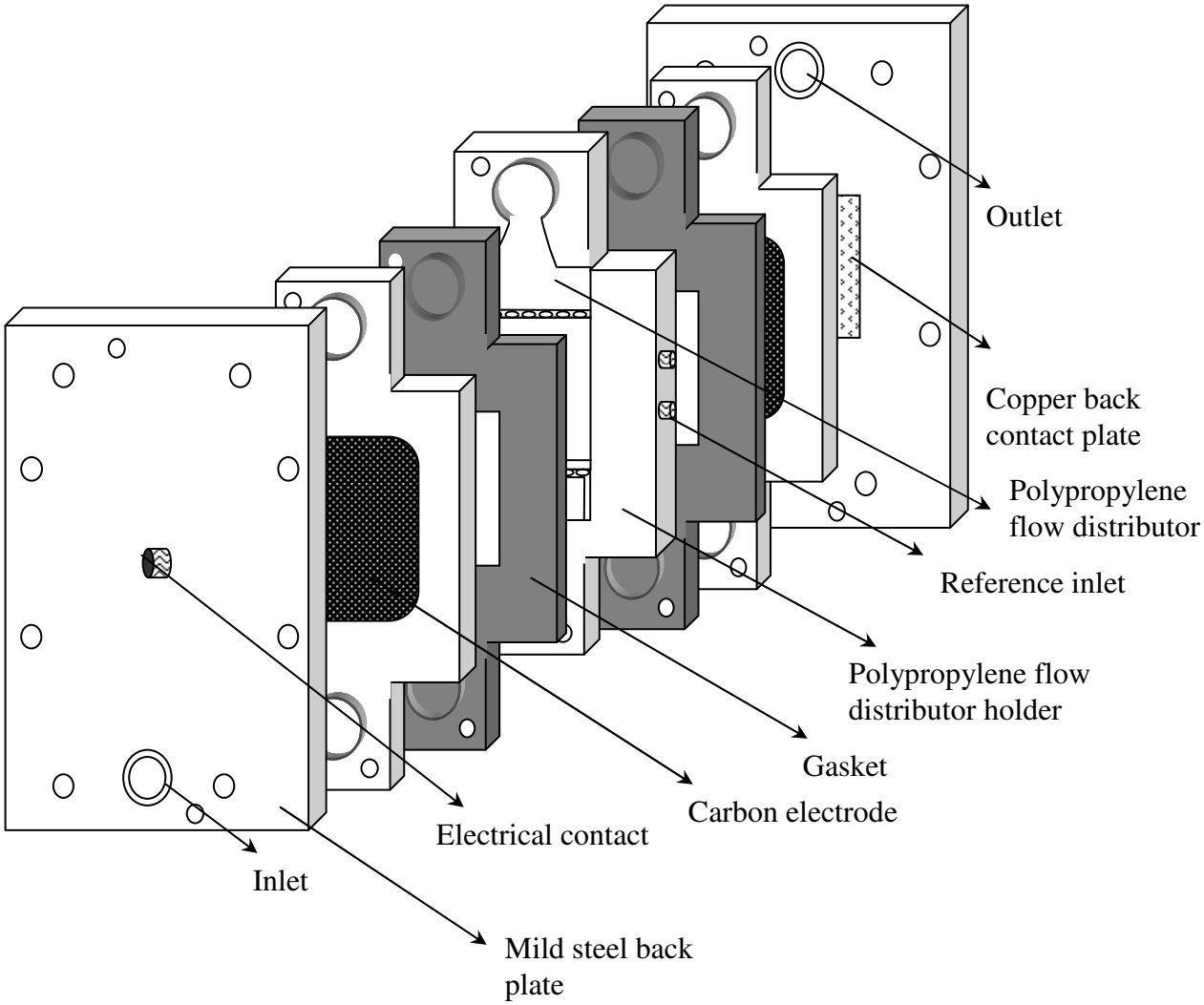

Fig 3.4: An exploded view of the 100 cm^2 soluble lead acid flow battery test cell.

The positive electrode was a carbon polymer composite that was either carbon/polyvinyl-ester (Entegris) or carbon/polyvinyldene difluoride (PVDF) (Eisenhuth). The negative electrode was made of nickel (Goodman Alloys) although initially carbon composites were used. The cell was clamped between two steel end plates (365 mm × 21 mm × 2 mm) with 8 steel tie-bars. The test cell could be tilted to a horizontal position onto the steel frame support, which allowed rapid and convenient dismantling and reassembly (Fig 3.2).

3.2.2. Control and data-logging instrumentation

Initial charge-discharge experiments within were carried out single cell using a Metrohm© Autolab PGSTAT302N along with 20 A booster instrumentation. A battery test station was designed and built for the automated testing of up to four flow cells simultaneously.

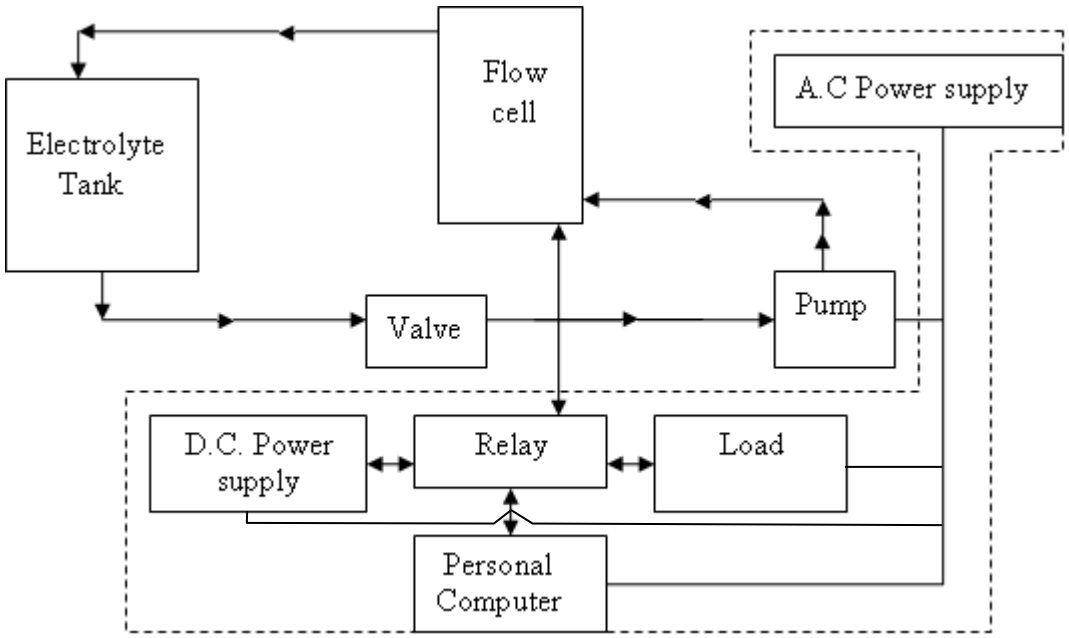

Fig 3.5: The flow system for soluble lead-acid battery (electrical circuit enclosed by dotted lines and free area is electrolyte circuit).

A personal computer and a USB data acquisition device (National Instruments USB-6225) were used for control and data-logging. The control software was written in the LabVIEW 8.2 (National Instruments™) graphical programming language. Fig 3.5 and Fig 3.6 show schematics of the electrical and electronic circuit layout of the flow cell and the automated testing setup.

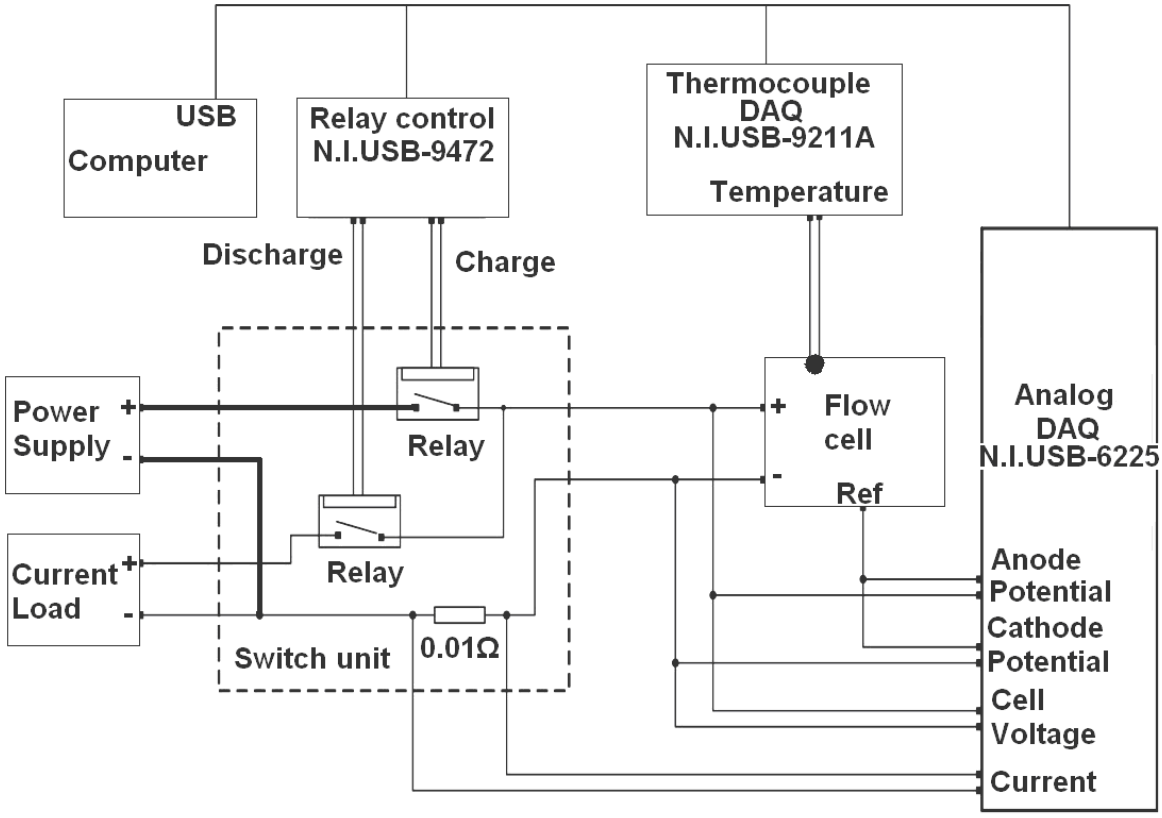

Fig 3.6: A circuit diagram of the automation shown considering with respect to all the parameters measured from the flow cell.

Each cell had a dedicated DC power supply (Thurlby Thandar Instruments TSX3510p programmable PSU 35 V, 18 A) and an electronic load (Thurlby Thandar Instruments LD300 DC Electronic Load 80 V, 80 A) for charging and discharging the battery at constant current. The power supply and electronic load were manually set to the required values before the start of each test and were switched on and off as required by a pair of electromechanical relays. These were controlled by the LabVIEW programme using a USB digital output device (National Instruments USB-9472) connected to the PC. The experimental data, including the current, cell voltage, anode and cathode potentials, redox potential and pH, were acquired and stored in the computer via an analogue national instruments USB Data Acquisition carrier (National Instruments USB-6225). A temperature acquisition was also set-up using a thermocouple USB Data Acquisition carrier (National Instruments USB-9211A), but never used. This equipment was shared by

all the four cells. Logged data was processed using standard software (Excel and SigmaPlot).

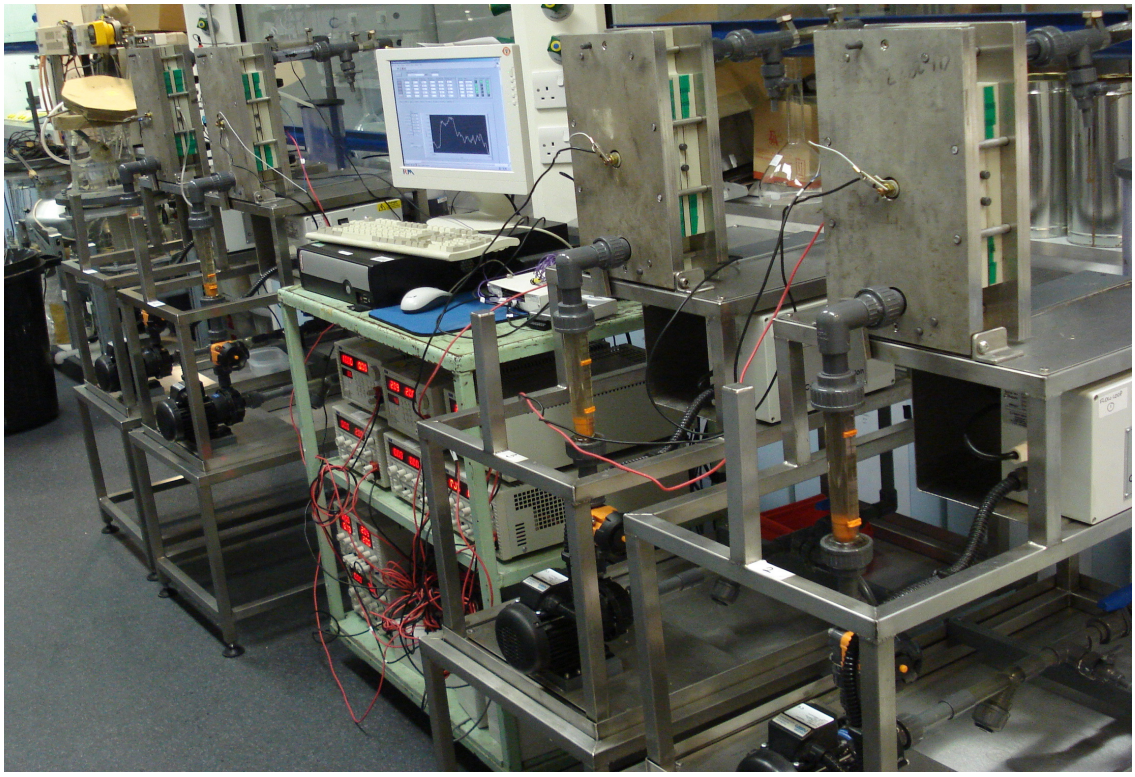

Fig 3.7: Four soluble lead-acid unit cells completely automated and under operation, flow cell assemblies each cell is approximately 1.5 m in width

3.3. Results and discussion

The electrolyte used was a combination of the following commercially available solutions:

(a). Lead (II) methanesulfonate solution ($Pb(CH_3SO_3)_2$ (50 wt % solution in water, Aldrich®), as the electrolyte solution.

(b). An additive, Hexadecyltrimethylammonium hydroxide (HDTMAH) (Puriss: 10 % in water, Fluka®), to improve plating characteristics.

(c). Methanesulfonic acid (CH_3SO_3H, 70 wt %, Sigma-Aldrich®), as free acid to maintain electrolyte conductivity and plating characteristics.

The actual volume of electrolyte used was 1.5 dm^3. The mean linear electrolyte velocity range was varied between 1 and 4 cm s^{-1} (70-150 dm^3 h^{-1}). Prior to each experiment the electrode surfaces were manually abraded using silicon carbide paper (grade 240 and 1200) to activate the surface or remove the left over deposits. This was followed by a quick rinse using either acetone or isopropanol (Laboratory grade). Fig 3.8 shows the two main flow distributor construction procedures used for the experiments.

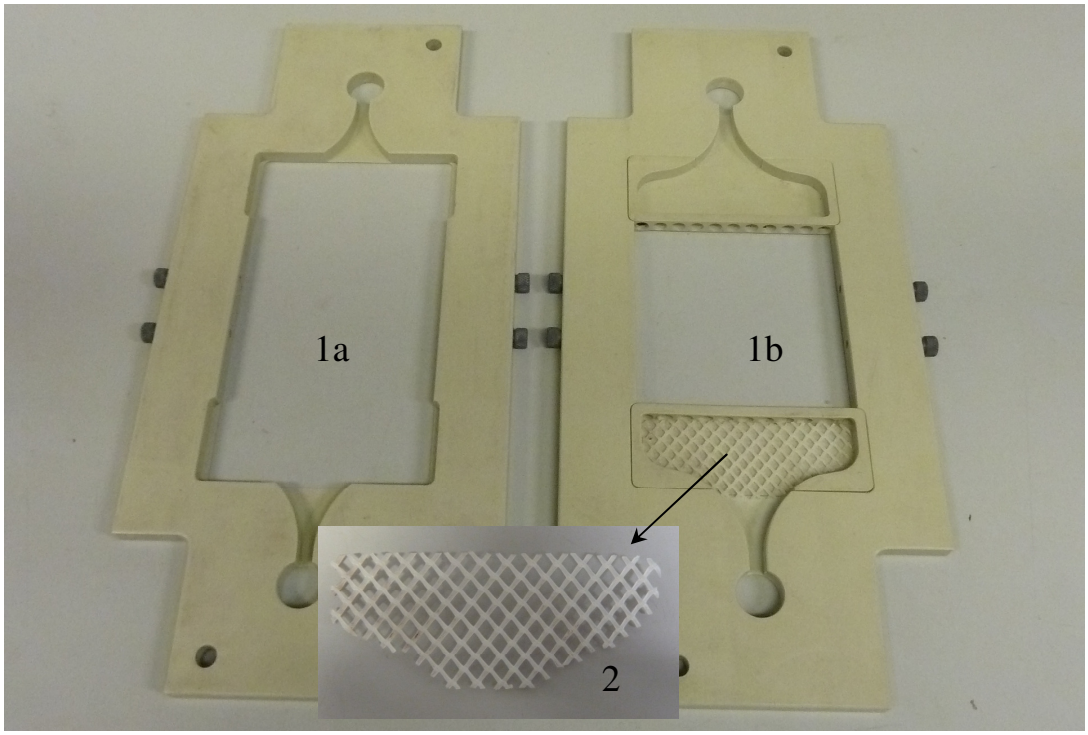

Fig 3.8: The important variations in the construction the experimental test cell in this thesis (1a) no inlet/ outlet slot and turbulence promoters, (1b) inclusion of inlet/outlet slots but turbulence promoters only at inlet and (2) a 2.1 mm thick polypropylene mesh (inset).

Table 3.1 gives the concise details of the preliminary experiments undertaken using different combinations of the operational parameters and electrolyte compositions. The effects of changes in the cell constructions, electrode materials and electrolyte filtration are also shown. The combined effect of one or more parameters was measured in terms of the charge, voltage and energy efficiencies (as defined in section 1.3.4), which are also provided in table 3.1, for each experiment.

Electrolyte				Mean linear flow velocity	Current density / mA cm^{-2}		Discharge cut-off cell voltage / V	Charge time / h	Total number of cycles	Flow distribution	Carbis® filtration / µm	Electrodes		% η_C	% η_E	% η_V
Pb^{2+} / mol dm^{-3}	MSA / mol dm^{-3}	HDTMAH / mol dm^{-3}	Volume / dm^3	cm s^{-1}	Charge	Discharge						−ve	+ve			
0.5	0.3	0.005	1.5	4	20	20	0.5	1	failed after 6 cycles	Complete with mesh	none	Carbon	Carbon	81	47	58
1.2	0	0.005	1.5	4	20	20	1.1	1	15(short circuit after 10 cycles)	Removed	none	Carbon	Carbon	63	41	67
1.1	0.03	0.005	1.5	2	10	10	1.1	1	35 (shorting after 22 cycles)	Removed	5	Carbon	Nickel	80	59	73
0.5	0.05	0.005	1.5	2	10	10	1.1	0.5	62(shorting after 60 cycles)	Removed	5	Carbon	Nickel	45	32	70
0.5	0.05	0.005	1.5	2	30	30	1.1	0.5	100 (filter blocked after 12 cycles)	Removed	5	Carbon	Nickel	17	12	67
0.5	0.05	0.005	1.5	2	10	10	1.1	0.5	121(shorting after 118 cycles)	Removed	5	Carbon	Nickel	57	40	68
0.5	0.05	0.005	1.5	2	20	20	1.1	0.5	117(shorting after 101 cycles)	Removed	5	Carbon	Nickel	67	49	73

Table 3.1: Table showing the list of initial experiments with the soluble lead-acid flow battery

Table 3.1 also gives in detail the transition of the experimental planning towards achieving higher number of operational cycles by altering initially the electrolyte concentration followed by the change of electrode materials. These variations in the initial experiments concluded the usage of a refined electrolyte concentration of 0.5 mol dm^{-3} Pb^{2+} in 0.05 mol dm^{-3} MSA and 5 mmol dm^{-3} HDTMAH, with a filter cloth (Carbisfiltration®) of 5 µm at 20 mA cm^{-2}. The transition towards this conclusion is given in further detail in the following discussion.

A single charge cycle test using an Autolab PGSTAT302N with a 20 A booster at 20 mA cm^{-2} with 0.5 mol dm^{-3} Pb^{2+} in 0.3 mol dm^{-3} MSA and 5 mmol dm^{-3} HDTMAH at a flow rate of 4 cm s^{-1} was run to observe the preliminary deposition with a complete cell construction (with flow distributors and turbulence promoters on both sides intact as in Fig 3.8 (1(b)) using Entegris® carbon polymer electrodes. This showed that the initial deposits were smooth and non-dendritic, as shown in Fig 3.9 (a) & (b). These deposits were highly adhesive to the electrode surface (without any cracks). The artefacts of the flowing solution due to the flow distributor can be seen on the lead dioxide deposition in Fig 3.9 (b) (those on the lead deposit in Fig 3.9 (a) are water marks).

(a) (b)

Fig 3.9: Photographs showing the initial deposition of (a) lead and (b) lead dioxide on Entegris® carbon polymer electrodes of 100 cm^2, at 20 mA cm^{-2} with 0.5 mol dm^{-3} Pb^{2+} in 0.3 mol dm^{-3} MSA and 5 mmol dm^{-3} HDTMAH at a flow rate of 4 cm s^{-1}.

The maximum cell voltage during charge was observed to be around 1.9 V. Upon further cycling, however, the cell went into severe short-circuit and failed (after 6 cycles). The cause being insufficient adhesion of the PbO_2 deposits to the positive electrode. It was observed that flakes of PbO_2 deposits detached from the electrode and collected towards the bottom of the cell (Fig 3.10). Further experiments with Entegris® carbon polymer electrodes and the same electrolyte combination yielded similar results, together with a further problem of heavy dendritic lead deposits. A filter cloth (Carbisfiltration®) of 5 µm was also used initially to reduce the lead dioxide particulate (sludge) in the electrolyte, which was more prevalent as the applied current density increased. This was later abandoned due to the persistence of sludge formation and stalling of the motor (Table 3.1). The impact of this effect was a reduction in the overall efficiency of the battery, although the cycle life was extended by more than 40 cycles.

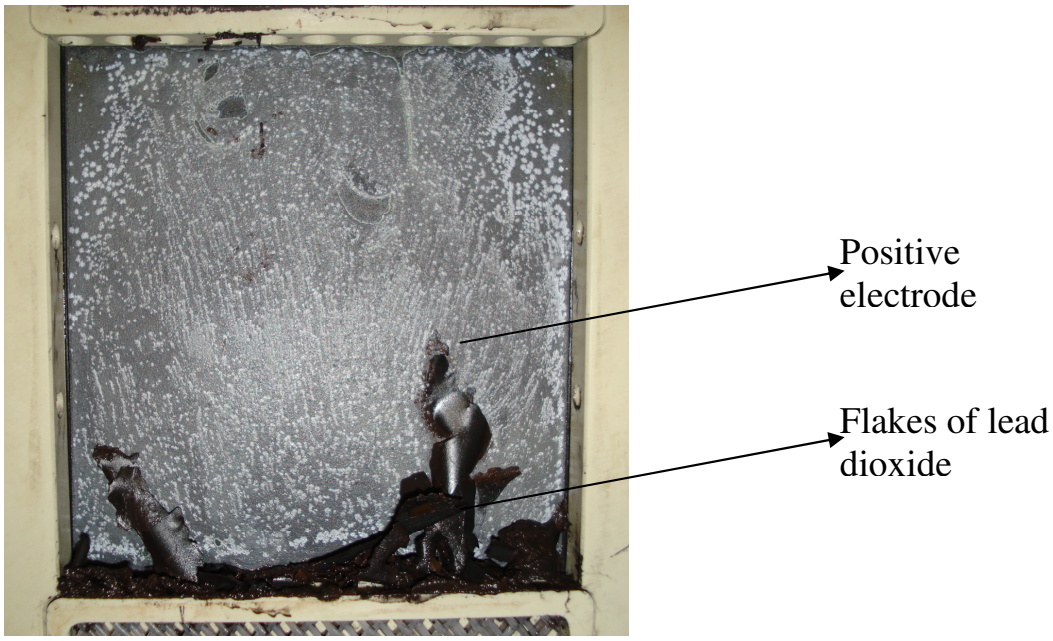

Fig 3.10: Photograph of the reaction chamber with the lead dioxide falling off as flakes.

Due to the difficulties described above, the electrode materials were changed to a Nickel (Ni) (99.9% Goodman Alloys) and Entegris® carbon (C) polymer for the negative and positive electrodes, respectively. The flow distributor and the turbulence promoters were

also completely removed form the cell construction (as shown in Fig 3.8(1(a))), where the accumulation of lead dioxide accumulation has caused the failure of the battery as well as loss in the charge efficiency. The automated operational set-up for the four flow systems was completed and the LabVIEW ® programming software was used to control the operation of each cell dynamically. The programme was set-up to measure the open-circuit cell voltage before and after each charge.

In the following investigations (Table 3.2), the composition of the electrolyte was modified with a 10 fold increase in the MSA concentration to 0.5 mol dm^{-3} Pb^{2+} in 0.5 mol dm^{-3} MSA and 5 mmol dm^{-3} HDTMAH, and the cell was operated at a linear flow velocity of 2 cm s^{-1}, with a discharge cell voltage limit of 1.1 V. These changes in the electrolyte parameters resulted in noticeable improvement in the operation of the battery: an increase in the overall efficiency (by nearly 20 %) and an extended operational cycle life (by more than 50 %), as shown in Table 3.2.

The cell using Ni-C electrodes was charge and discharged for more than 100 cycles at 10 mA cm^{-2}, resulting in an overall energy efficiency of 68 %, with the above stated operational conditions. The mode of construction and the electrolyte combination used also enabled the testing of the soluble lead acid RFB at different current densities, length of charge time period, surface preparation techniques, electrode materials and regenerative techniques, as described in Table 3.2. The influence of these parameters on the test cell was reflected in the variation of the number of operational cycles achievable as well as the resulting charge, voltage and overall efficiency values.

Experimental conditions		Total number of operated cycles	% Efficiency			Experimental parameters			
			$\% \eta_C$	$\% \eta_V$	$\% \eta_E$	j / mA cm^{-2}	Charge time / h	Electrolyte	Electrode
Variable current density		187	94	79	75	10	1	0.5 mol dm^{-3} Pb^{2+}/ 0.5 mol dm^{-3} MSA/ 5 mmol dm^{-3} HDTMAH	Nickel (-ve) / Entegris carbon (+ve)
		43	90.5	78.8	71.3	20	1		
		20	86	72.4	62.4	30	1		
Grit blasted carbon electrode surface	yes	25	75	71	53	20	2	0.5 mol dm^{-3} Pb^{2+}/ 0.5 mol dm^{-3} MSA/ 5 mmol dm^{-3} HDTMAH	
	no	25	81	77	63	20	2		
Electrode materials *(details in Table 3.3)*		51	80	70	56	20	2	0.9 mol dm^{-3} Pb^{2+}/ 0.3 mol dm^{-3} MSA/ 5 mmol dm^{-3} HDTMAH	Graphite (-ve) / PVDF carbon (+Ve)
Regenerative recycling with H_2O_2	H_2O_2 additions	Cycle no	η_C %	H_2O_2 volume / mL		20	2	0.5 mol dm^{-3} Pb^{2+}/ 0.5 mol dm^{-3} MSA / 5 mmol dm^{-3} HDTMAH	Nickel (-ve) / Entegris carbon (+ve)
	Total - 5	Total-77		Total - 380					
	1st	18	86	56 + (50 % excess)					
	2nd	14	83	64 + (50 % excess)					
	3rd	15	80	70 + (50 % excess)					
	4th	15	77	90 + (50 % excess)					
	5th	15	75	100 + (50 % excess)					

Table 3.2: Table showing the list of experiments for the performance measurements of soluble lead-acid flow battery.

3.3.1. Effect of current density

The modified cell design (Fig 3.8(1(a))) with the electrolyte combination, 0.5 mol dm^{-3} Pb^{2+} in 0.5 mol dm^{-3} MSA and 5 mmol dm^{-3} HDTMAH at a mean linear flow rate of 2 cm s^{-1}, was used to conduct the experiments at current densities of 10, 20 and 30 mA cm^{-2}. The number of operational cycles along with the values of the charge, voltage, and energy efficiencies were calculated and are presented in Table 3.2. These experiments were run on identical cells using the automated control setup, designed for parallel operation at a 1 h constant-current charge and discharge, until failure. In these tests, the cell operating at the lowest current density i.e.,10 mA cm^{-2}, was charged and discharged for more than 150 cycles, significantly more than the other two test cells operating at 20 mA cm^{-2} (43 cycles) and 30 mA cm^{-2} (20 cycles). As the current density increased the number of operational cycles quickly decreased, this was due to the accumulation of charge via inefficiency of the system for total charge conversion. Hence the experiment was automatically stopped when the battery was declining into failure mode or inefficient operation.

The cell operating at 10 mA cm^{-2} exhibited good cyclability and good charge (94 %) and voltage (79 %) efficiencies upto 162 cycles, after which the charge voltage at the end of charge began to rise slowly (Fig 3.11(a)) and the cell showed signs of a decrease in the Pb^{2+} ion concentration. This is also reflected in the charge and the voltage efficiencies, which began to decline. This type of uniform and steady charge-discharge performance is not observed at higher current densities in which depletion of Pb^{2+} concentration took place more rapidly as the cycles progressed. A lower number of operational cycles (Table 3.2) attained with the increasing current density before total failure of the battery also reflects this behaviour.

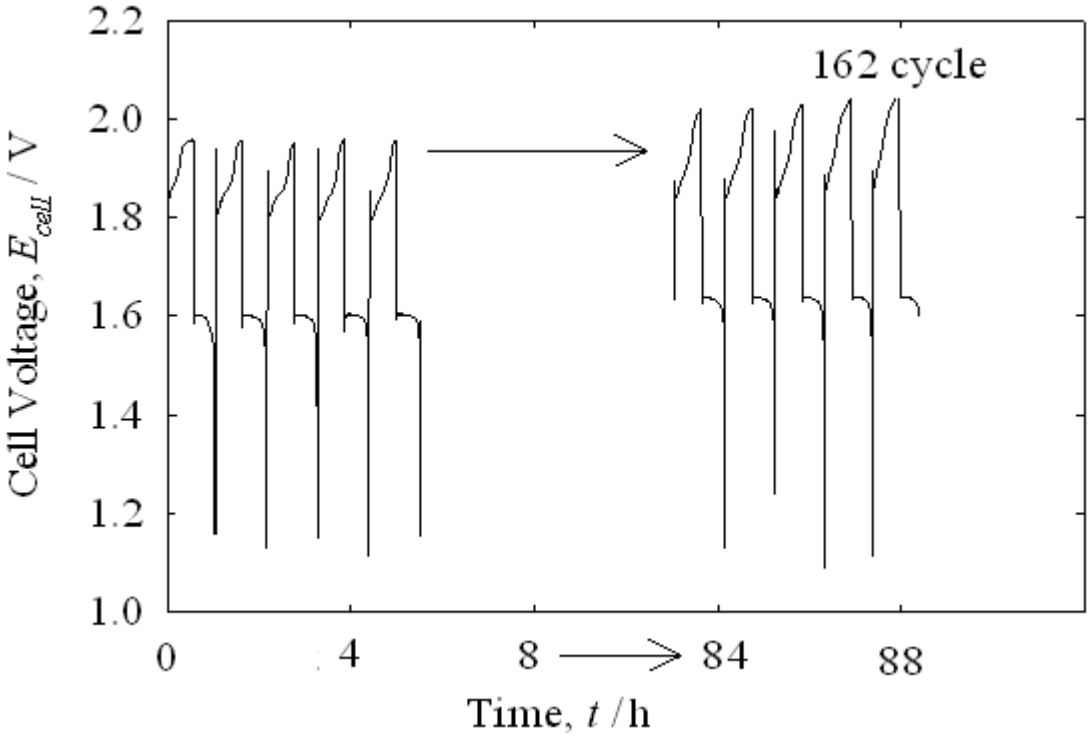
162 cycle
Cell Voltage, E_{cell} / V
2.2
2.0
1.8
1.6
1.4
1.2
1.0
0
4
8
84
88
Time, t / h

(a)

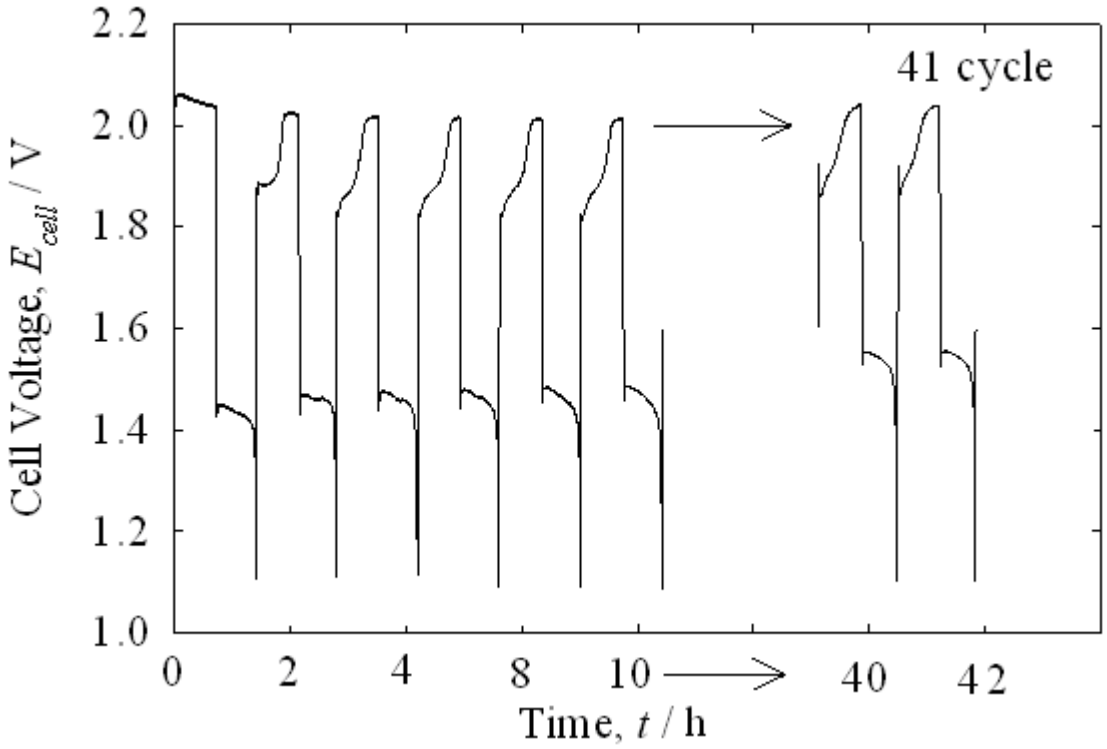
41 cycle
Cell Voltage, E_{cell} / V
2.2
2.0
1.8
1.6
1.4
1.2
1.0
0
2
4
8
10
40
42
Time, t / h

(b)

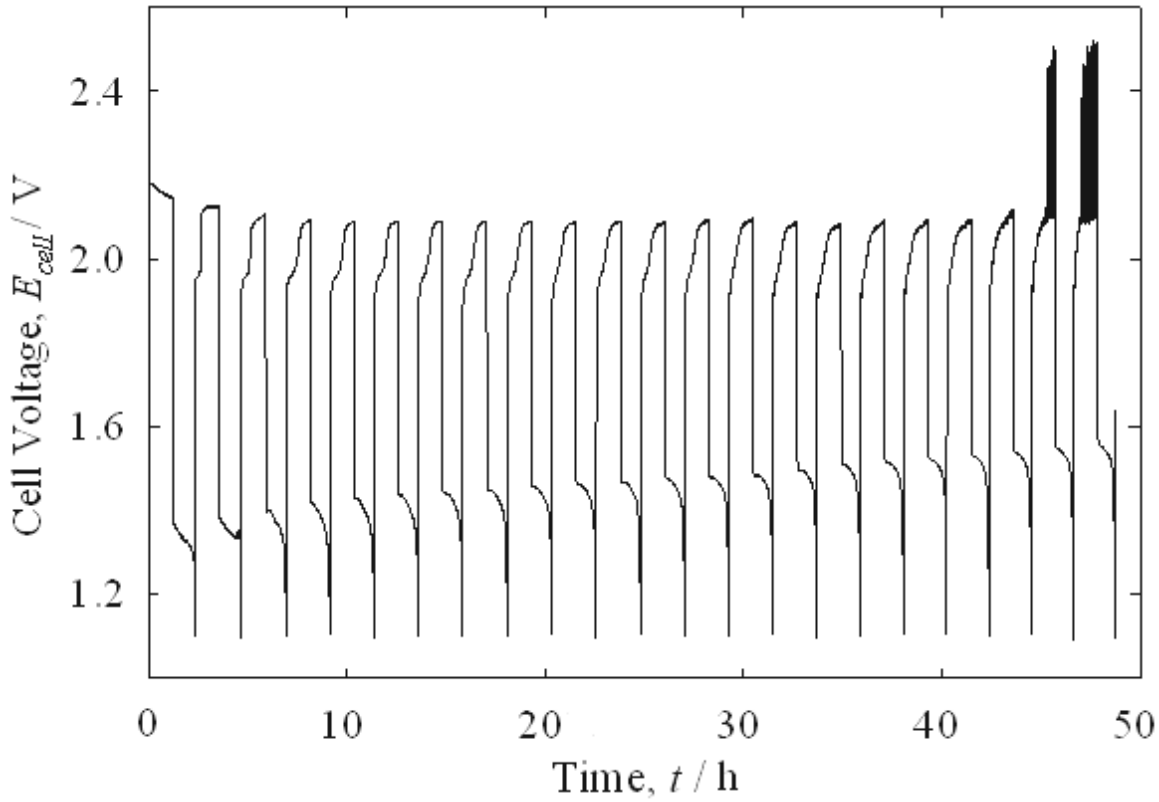

(c)

Fig 3.11: Charge-discharge performance graphs of soluble lead acid flow battery at various current densities of (a) 10 mA cm^{-2}, (b) 20 mA cm^{-2} and (c) 30 mA cm^{-2} for an electrolyte of 0.5 mol dm^{-3} Pb^{2+} in 0.5 mol dm^{-3} MSA with 5 mmol dm^{-3} HDTMAH at 2 cm s^{-1}.

This rise in the charge and discharge voltages can be attributed to the increasing thicknesses of the lead and lead-dioxide deposits at the end of successive charge cycles. The deposits also tended to be thicker, rougher and more uneven as the current density was increased. Increased sludge formation resulting in a subsequent decrease in the Pb^{2+} ions concentration in the solution was also observed. These factors also influence the voltage efficiency through an increase in the ohmic drop and the overpotentials associated with the individual electrodes (due to the build up of electrodeposits)[14].

3.3.2. Effect of surface preparation

The adhesion of lead dioxide to the electrode surface was investigated using a different surface preparation. An equivalent layer (< 0.5 mm) to that of the hand polished electrode was sand blasted, using a grit of alumina particles of 20 µm from a compressed air gun. The electrode was then washed and ultrasonicated to remove the excess particles and loose carbon powder. The resulting electrode surface was coarser than that obtained by manual abrasion using silicon carbide paper.

Two test cells were prepared, one with the grit-blasted carbon electrode and one with a manually abraded electrode. For both cells, 2 h charge-discharge experiments at 20 mA cm^{-2} using the electrolyte of 0.5 mol dm^{-3} Pb^{2+} in 0.5 mol dm^{-3} MSA and 5 mmol dm^{-3} HDTMAH at mean linear flow rate of 2 cm s^{-1} for 25 cycles at 23ºC, were carried out. The resulting performance was characterised in terms of charge and voltage efficiencies (Table.3.2). Heavy shedding of the lead-dioxide deposit was observed in the cell with a sand-blasted electrode, which exhibited lower charge (75%) and voltage (71%) efficiencies in comparison to those of the manually abraded electrode (81 % charge efficiency and 77 % voltage efficiency) following the same number of cycles. This demonstrates that the surface preparatory techniques effects the efficiency of the cell and that the adhesion of PbO_2 depends on operational conditions and the phase composition of the PbO_2 being deposited, which was also shown by X.Li et al[14].

It can also be observed from Fig 3.12(a) that towards the 20^{th} cycle the cell with the grit-blasted electrode showed signs of shedding eventually causing shorting, observed in the form of ripples in the cell voltage during the charge cycle. This was not observed in the case of the manually abraded electrode (Fig3.12 (b)), which remained stable after 25 cycles. Upon dismantling the cells after 25 cycles, the grit blasted electrode deposits were seen to be rough and uneven, with heavy shedding of PbO_2 compared to the manually

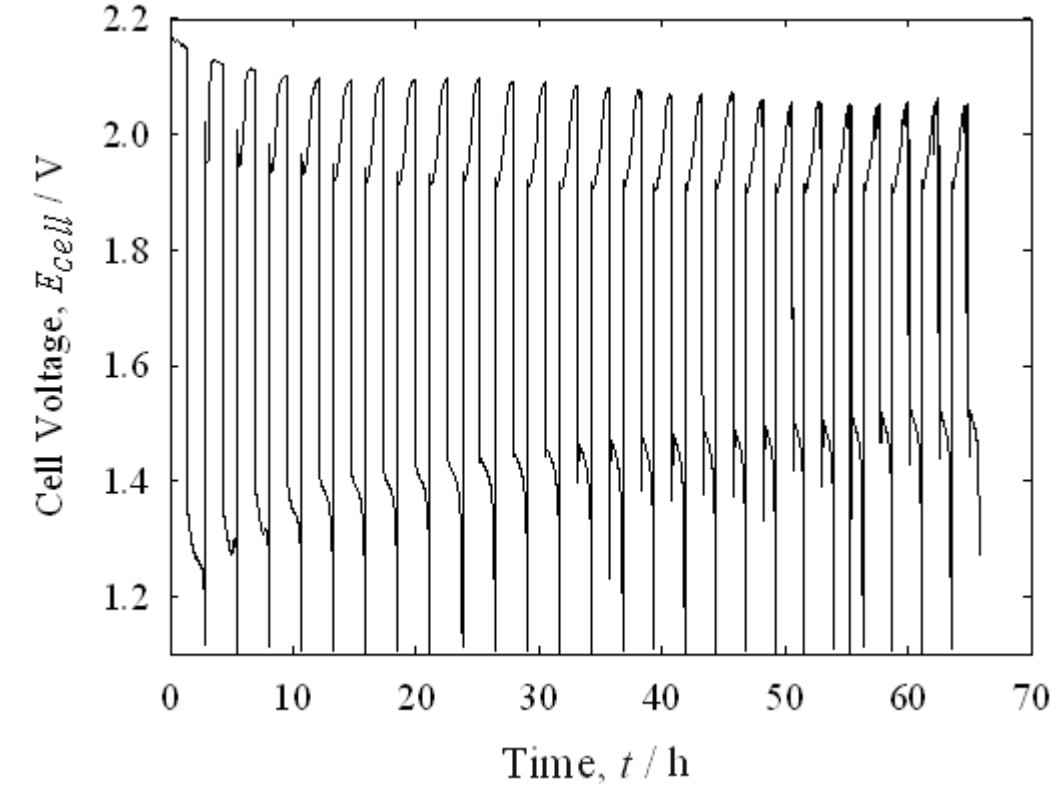

(a)

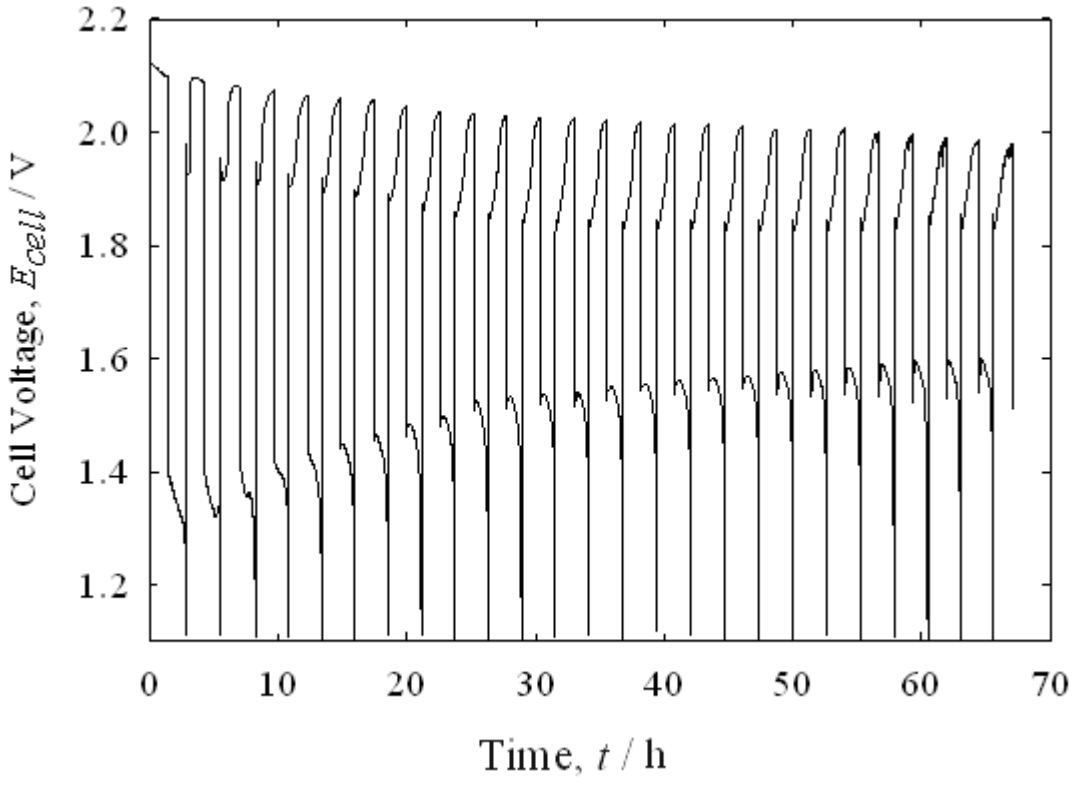

(b)

Fig 3.12: The charge discharge performance of the battery for 25 cycles with an electrolyte of 0.5 mol dm^{-3} Pb^{2+} in 0.5 mol dm^{-3} MSA with 5 mmol dm^{-3} HDTMAH having (a) blasted and (b) non-blasted surface of the electrode.

abraded electrode surface. The latter was compact with very little shedding of the PbO_2 electrodeposits. The poor performance of to the grit-blasted electrode could be due to the incomplete removal of the non-conducting polymer layer by the procedure followed during the electrode preparation.

3.3.3: Effect of electrode materials

Electrode material	Manufacturer	Dimensions (l ×b× t)/ mm
Carbon/polyvinyldene difluoride (PVDF)	Eisenhuth GmBH	130× 130 × 6.35
Expanded graphite	SGL carbon	130× 130 × 1.6
Nickel	Goodman Alloys	130× 130 × 1.12
Carbon/polyvinyl-ester	Entegris	130× 130 × 3.65

Table 3.3: Table showing the various commercially available electrode materials used for testing in the 100 cm^2 test cell

Two new electrode materials were tested to confirm any further possibility of using low-cost industrial electrodes to replace the costly Nickel electrodes. The materials tested were (as shown in Table 3.3) tested in pair combinations of PVDF/graphite, PVDF/PVDF, graphite/graphite and graphite/PVDF, and compared with Ni-C. A 2 h charge-discharge experiment with 0.9 mol dm^{-3} Pb^{2+} in 0.3 mol dm^{-3} MSA with 0.005 mol dm^{-3} HDTMAH[14] electrolyte concentration was used to test the electrodes at a current density of 20 mA cm^{-2} and a flow rate of 2 cm s^{-1}. A similar experiment with the Ni-C pair gave a charge-discharge performance of 47 cycles at a charge efficiency of 90 % and a voltage efficiency of 68 %. Of the tested combinations only the graphite/PVDF pair gave a successful charge-discharge performance (Fig 3.13), which was slightly better than that using the Ni-C (by only 3 cycles). In comparison, the efficiencies were lower by 8 %. The PVDF electrode became brittle after repeated cycling. A soft powdery surface in the area

of electrodeposition was found. It was also noticed that mechanical treatment cannot be used on the graphite electrode. This showed that the graphite/PVDF pair was not suitable for cycling in this flow battery, although very good for singular coatings.

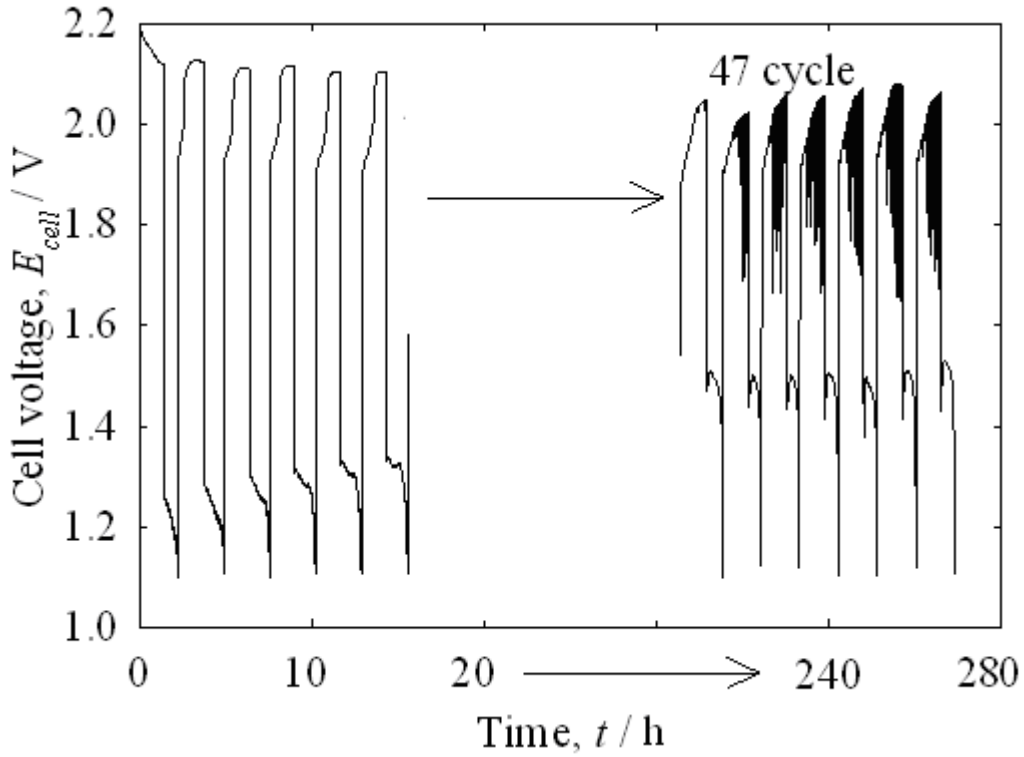

Fig 3.13: Cell performance using PVDF/graphite electrodes at 20 mA cm^{-2} with an electrolyte of 0.9 mol dm^{-3} $Pb^{2+}$and 0.3 mol dm^{-3} MSA with 5 mmol dm^{-3} HDTMAH, at 2 cm s^{-1}.

3.3.4: Regenerative recycling

From the previous experimental results and from the open literature related to the soluble lead-acid flow battery it has been demonstrated that the cell performance is affected by the following factors:

1. A progressive build–up of deposits on the electrode surfaces, due to inefficiencies in the charge-discharge reactions of Pb and PbO_2

2. Changes in the deposition structure (dendrites) and the formation (phase of PbO_2) and adhesion (particles of PbO_2) of the electrode deposits over-time.

The use of manual cleaning methods can lead to cracks and uneven electrode surfaces (especially carbon), and is not therefore advised for stack maintenance. Hence a cleaning method was required to restore the electrodes to their initial state without damaging the electrode surfaces. Hence a simple chemical procedure was proposed to revive the charge-discharge performance of the cell by using hydrogen peroxide (H_2O_2) (Fisher® scientific, Lab grade, Hydrogen peroxide 100 volumes > 30% w/v) for dissolution of the electrode deposits. Hydrogen peroxide is a very strong reductant, hence it spontaneously reduces lead dioxide deposits[15-17] but oxidising the lead deposit to Pb^{2+} ions is a slow reaction. The reactions associated with each electrode upon addition of H_2O_2 (at OCV) are given below:

Positive: $$PbO_2 + H_2O_2 + 2H^+ \rightarrow Pb^{2+} + 2H_2O + O_2 \uparrow \quad (6)$$

Negative: $$Pb + H_2O_2 + 2H^+ \rightarrow Pb^{2+} + 2H_2O \quad (7)$$

From equations (6) and (7), it can also be seen that a total of 4 moles of water are produced upon reaction. Heavy foaming can be observed due to the production of oxygen, with a slight temperature change that subsides soon after, without further problems.

An experiment was conducted using Ni-C electrodes, with a solution of 0.5 mol dm^{-3} Pb^{2+} and 0.5 mol dm^{-3} MSA with 0.005 mol dm^{-3} of HDTMAH at a flow rate of 2 cm s^{-1}. The cell was charged and discharged at a constant current of 20 mA cm^{-2}, with a charge period of 2 h. After 18 cycles, the cell was stopped and the open circuit cell voltage (E_{cell}^{oc}) was measured as 1.69 V. The charge efficiency of the cell was calculated as 86 % and was used to estimate the amount of H_2O_2 required. Similar experiments previously showed that adding the stochiometric amount of H_2O_2 is insufficient to completely dissolve both

deposits. Due to the continuous circulation of the solution, H_2O_2 decomposes before it completely dissolves the deposits:

$$2H_2O_2 + O_2 \rightarrow 2H_2O + 2O_2 \uparrow \quad (8)$$

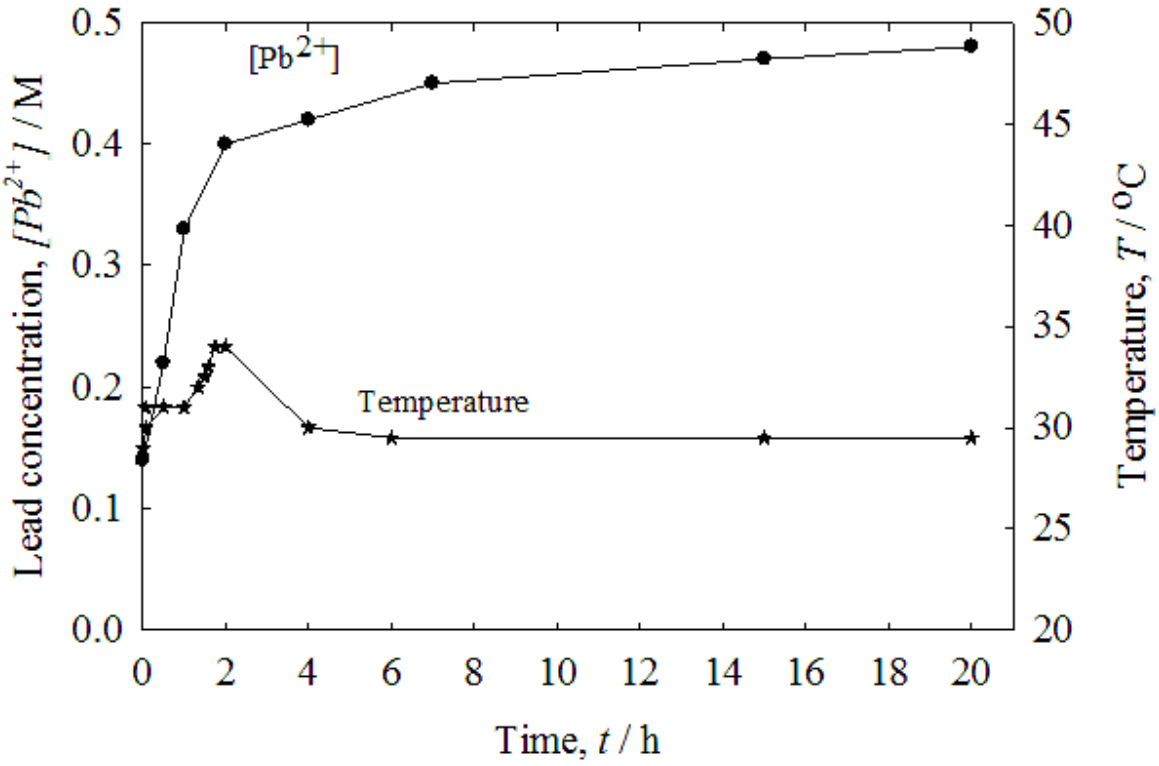

Fig 3.14: Plot showing the concentration of the lead ions and temperature of the electrolyte upon the addition of hydrogen peroxide.

It was found that 50% excess H_2O_2 was the ideal quantity to dissolve the deposits, to balance the rate of decomposition[18]. Hence, an excess amount (50 %) of H_2O_2 was required to sustain the reaction until complete dissolution of the electrodeposits, particularly lead. The change in the concentration of Pb^{2+} ions can be determined by taking samples at regular intervals and diluting the samples in 1 mol dm^{-3} $NaNO_3$ to run voltammetric experiments using a glassy carbon electrode of 0.126 cm^2 geometric area. Figure 3.14 shows the evolution of the concentration of lead ion and the temperature *vs.* time in the electrolyte. It can be seen that with the addition of H_2O_2 there is a slight rise in

the temperature of the electrolyte by 4 ºC over the first 2 hours. The temperature of the electrolyte eventually returns to room temperature after approximately 6 hours. The electrolyte also starts to bubble and a foam forms following the addition of H_2O_2. Hence smaller volumes were added at 15 min intervals to prevent loss of the additive via excessive foam formation.

Cycle no	$\% \ \eta_C$	$\% \ \eta_V$	$\% \ \eta_E$	**H_2O_2 additions**	**H_2O_2 volume / mL**
18	91	72	66	1st	56 + (50 % excess)
14	83	72	60	2nd	64 + (50 % excess)
15	80	72	58	3rd	70 + (50 % excess)
15	77	71	55	4th	90 + (50 % excess)
15	77	70	54	5th	100 + (50 % excess)

Table 3.4: Table showing the efficiencies and the quantities of the systematic amounts of H_2O_2 addition after each cycle.

Fig 3.15(a) shows the charge-discharge performance of the cell with the fresh electrolyte during the initial cycles. Towards the 18th cycle, the electrolyte changes colour as shown in Fig 3.16 (a), and the lead dioxide particles in the flow circuit accumulated in locations where poor convection exists. This is reflected as a spike in the voltage during charge (Fig 3.15(a)). After the addition of H_2O_2, a transition of the electrolyte solution from black/brown to a relatively clear colour can be observed through the transparent acrylic pipeline and the reservoir, as shown in Fig 3.16(b) and Fig 3.16(c). The electrolyte was left to rest until it was clear of any residual foam or bubbles at a low flow rate (< 1cm s^{-1}). Hence, H_2O_2 cleans the electrode surfaces by replenishing the electrolyte with Pb^{2+} ions by dissolving the electrolyte sludge that has been accumulated in the flow circuit as well as the electrodeposits, which is a very efficient regeneration method without the need for dismantling or manual cleaning of the cell.

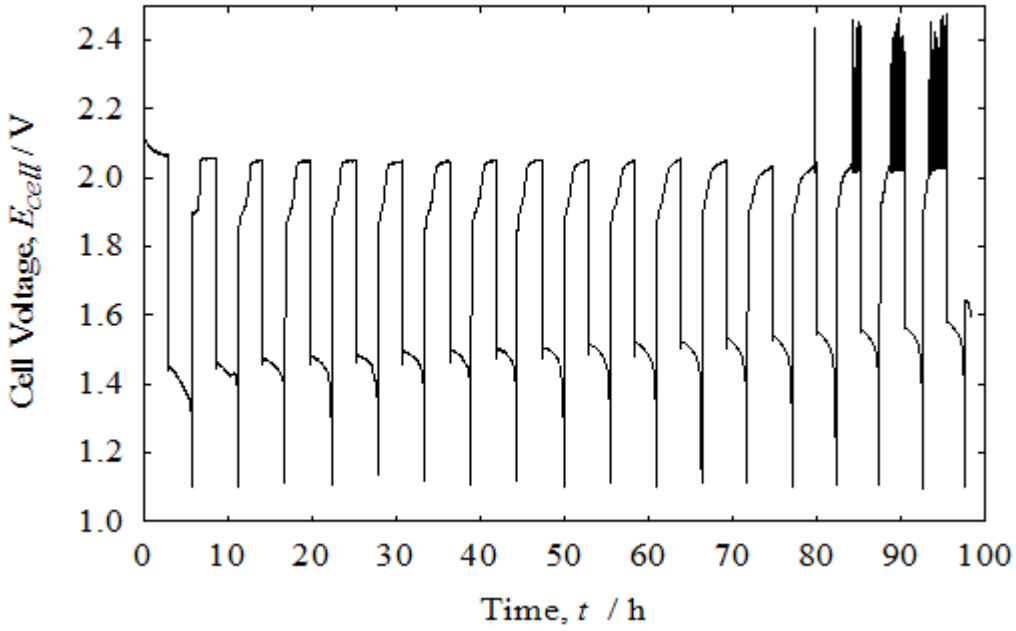

(a)

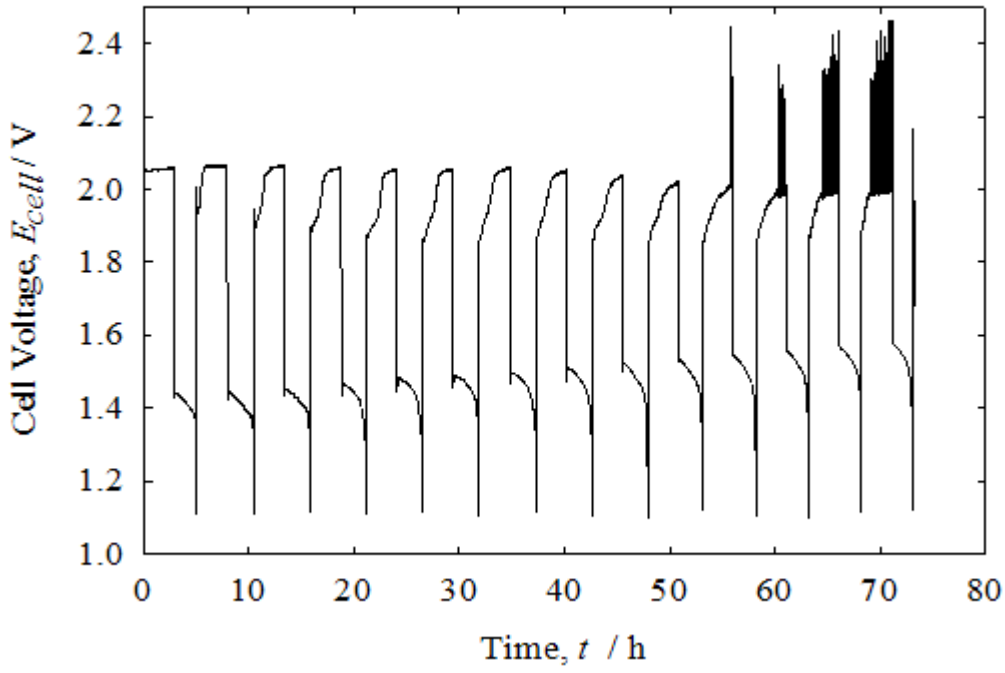

(b)

Fig 3.15: The charge–discharge performance of 100 cm^2 cell at a mean linear flow velocity of 2 cm s^{-1} with an electrolyte consisting of 0.5 mol dm^{-3} mol dm^{-3} Pb^{2+} in 0.5 mol dm^{-3} MSA with 5 mmol dm^{-3} of HDTMAH at 20 mA cm^{-2} (a) fresh electrolyte and (b) after first addition of H_2O_2.

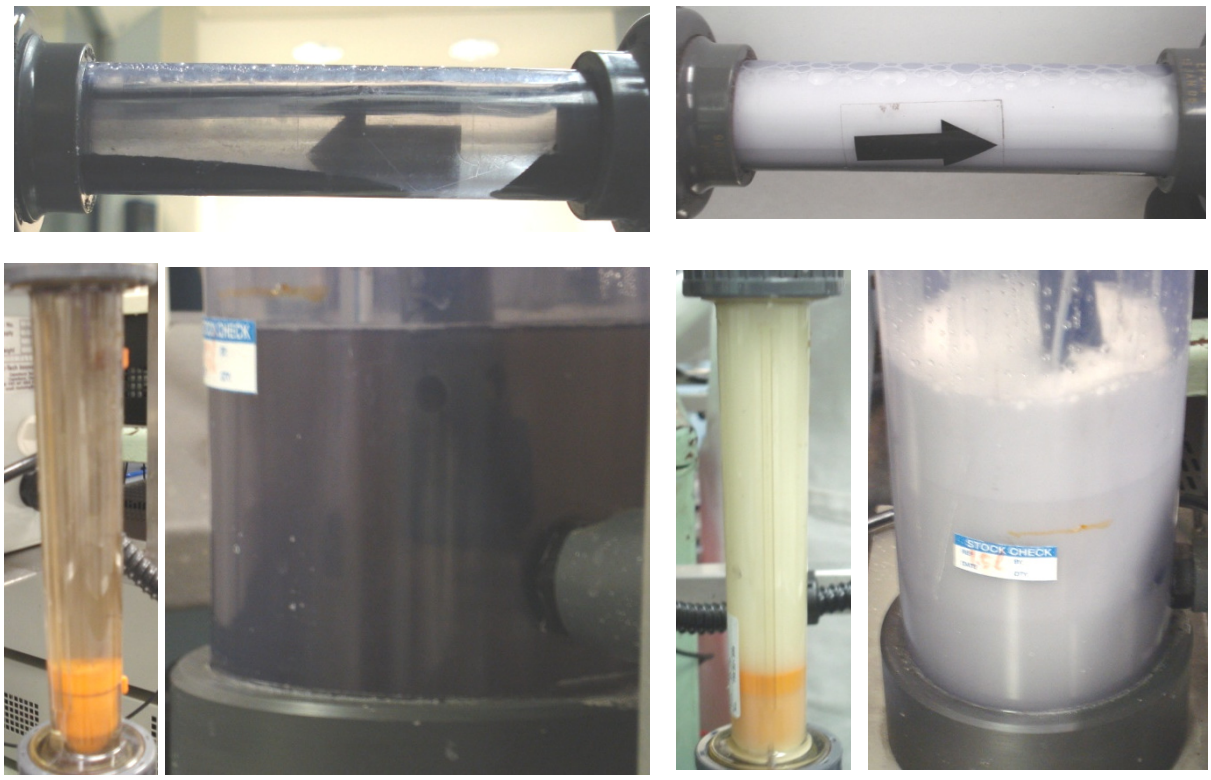

Fig 3.16: The inlet and outlet pipelines and the tank of the flow system (clockwise) showing the transition of the electrolyte from (a) heavy shedding, (b) addition of hydrogen peroxide and (c) a clear electrolyte solution.

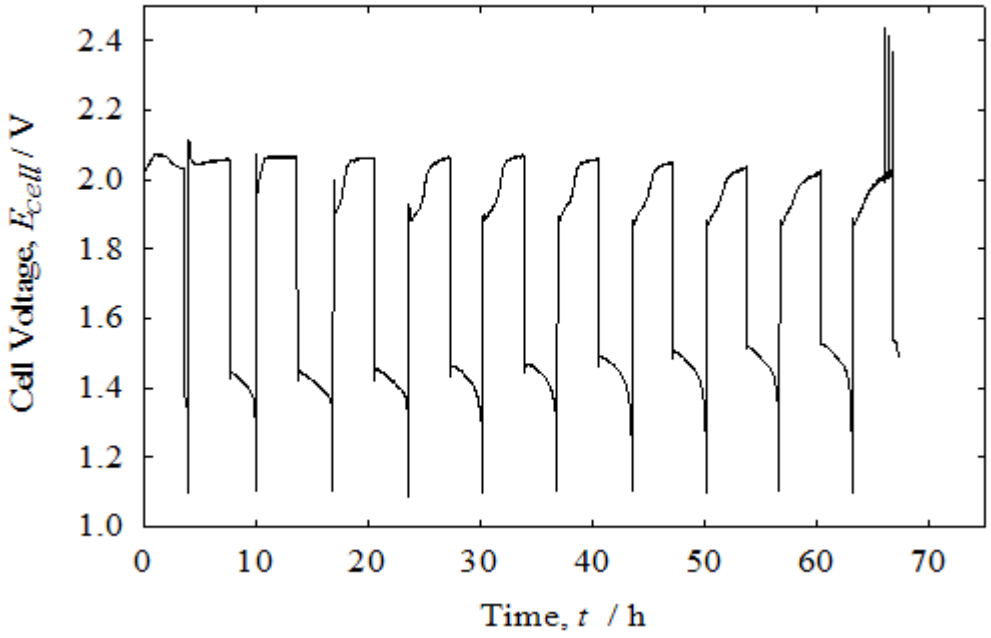

(a)

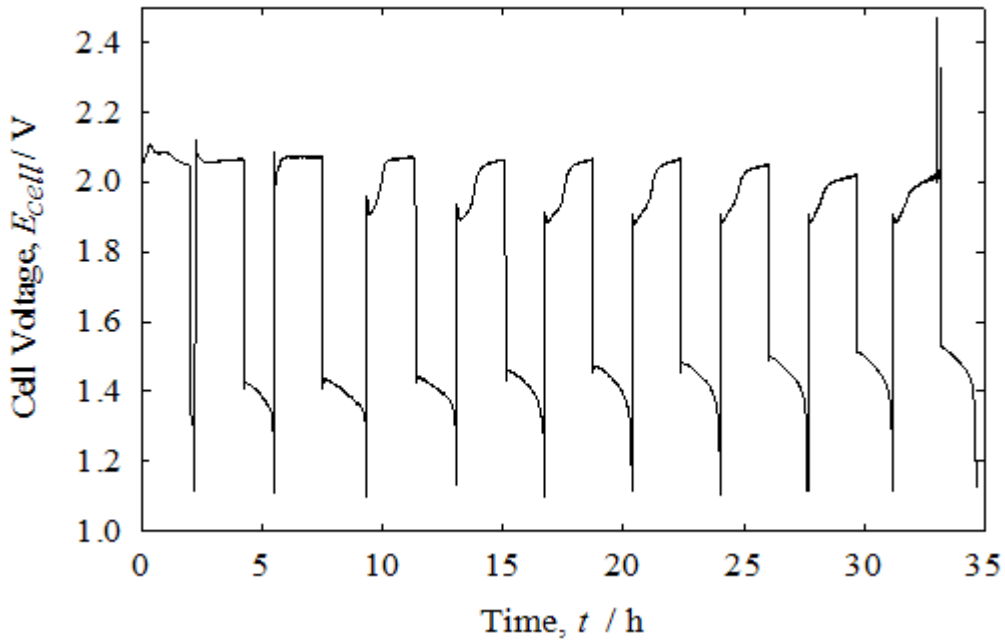

(b)

Fig 3.17: The charge–discharge performance of 100 cm^2 cell at a mean linear flow velocity of 2 cm s^{-1} with an electrolyte consisting of 0.5 mol dm^{-3} Pb^{2+} in 0.5 mol dm^{-3} MSA with 5 mmol dm^{-3} of HDTMAH at 20 mA cm^{-2} after(a) second and (b) third addition of H_2O_2.

The open-circuit potential measured before and after the addition of H_2O_2 provides a clear indicator of the amount of accumulated deposits. Hence, when the OCV dropped to 1.62 V after H_2O_2 addition, the cell was restarted. The cell was cycled for another 15 cycles and the performance was poor in terms of the average charge (83 %) and voltage (72 %) efficiency compared to that of the initial performance. This procedure was repeated 3 times, after which the experiment was stopped. The cell performance after the first addition was shown in the Fig 3.15(b). The performance for the further additions of H_2O_2 can be seen in Fig 3.17(b). The efficiencies (Table 3.1) associated with of these cell cycles exhibit a constant fall after every addition. This is due to the residual (unreacted) H_2O_2 left over after each addition. Hence, the first cycles do not give good discharge performance after the second and third additions. It was also observed that after the fourth addition the solution slightly turned pale green, suggesting a possible contamination with dissolved nickel (from the electrode plate). Other problems associated with these continuous additions of peroxide are pitting, corrosion and subsequent softening of the carbon polymer electrode.

3.3.5. Effect of self discharge

The effect of self discharge was measured via open-circuit voltage monitoring. A 1h charge-discharge experiment at 10 mA cm^{-2} using Ni-C electrodes with an electrolyte of 0.5 mol dm^{-3} Pb^{2+} and 0.5 mol dm^{-3} MSA with 0.005 mol dm^{-3} of HDTMAH with a cut-off cell voltage of 1.1V and a linear flow velocity of 2 cm s^{-1} was run for 100 cycles. An open circuit potential of 1.68 V was measured immediately after the cell was stopped (after charge cycle 101) using a digital voltmeter. This experimental set-up was left to stand undisturbed (no electrolyte flow) for 360 h. After this period, the open-circuit voltage was recorded as 1.64 V, a 40 mV drop. Upon restarting the cell was discharged and then was charge-discharge with the same operating conditions. A normal charge-discharge performance was obtained for 57 cycles. This confirms the ability of the soluble lead-acid

battery to retain charge (i.e. the electrodeposits) for prolonged periods of open–circuit time.

3.3.6. Failure mode analysis

The experiments reported in the previous sections yield information about the battery performance until failure. The two main causes of cell failure were identified as described below:

(***a). Dendritic lead deposits***. This was the most common cause of failure found during battery operation. The dendritic electro-deposition at the electrode edges, also known as the *edge effect* (circled in Fig 3.18(a)), was the most predominant characteristic at high current densities (beyond 30 mA cm^{-2}). This could also be due to an imbalance in the concentrations of the Pb^{2+} ions and MSA. Hence, a suitable concentration (between 0.5-1 mol dm^{-3}) of both was required to obtain smooth and uniform deposits.

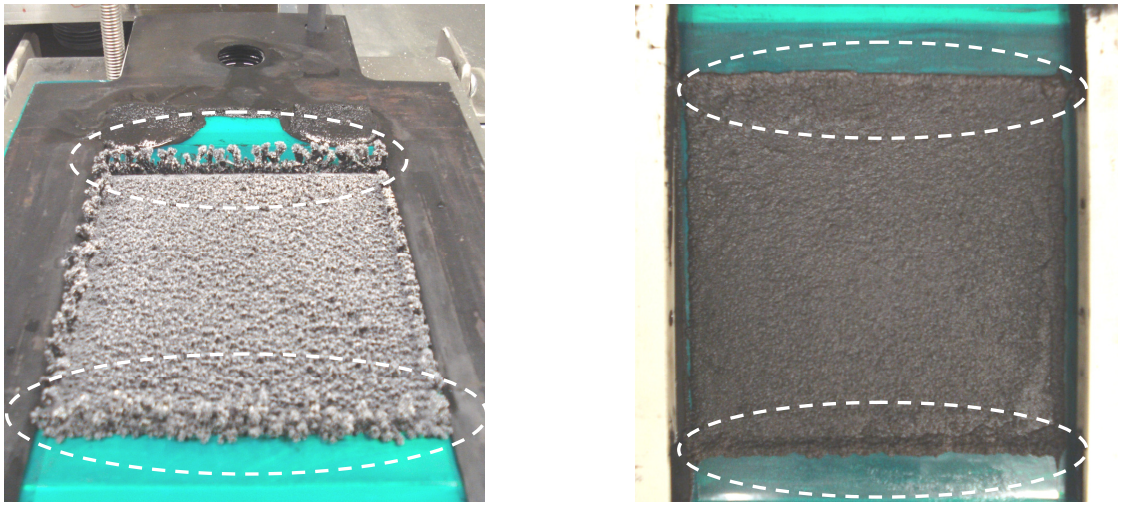

(a) (b)

Fig 3.18: Photographs showing the edge effect (circled) for (a) lead (negative) and (b) lead dioxide (positive) electrode deposits at 40 mA cm^{-2} for 2 h charge using 1 mol dm^{-3} Pb^{2+} and 0.5 mol dm^{-3} MSA with 0.005 mol dm^{-3} of HDTMAH at a linear flow velocity of 2 cm s^{-1}.

The positive electrode (PbO_2) also formed thick electro deposits (circled white in Fig 3.18(b)) towards the edge of the electrode, with less deposition towards the middle. The growth of these deposits was greater at the inlet and the outlet of the cell electrolyte compartment, where the concentration of lead ions is at its highest. In all cases the dendrite growths bridged the inter-electrode gap, resulting in electrical shorting.

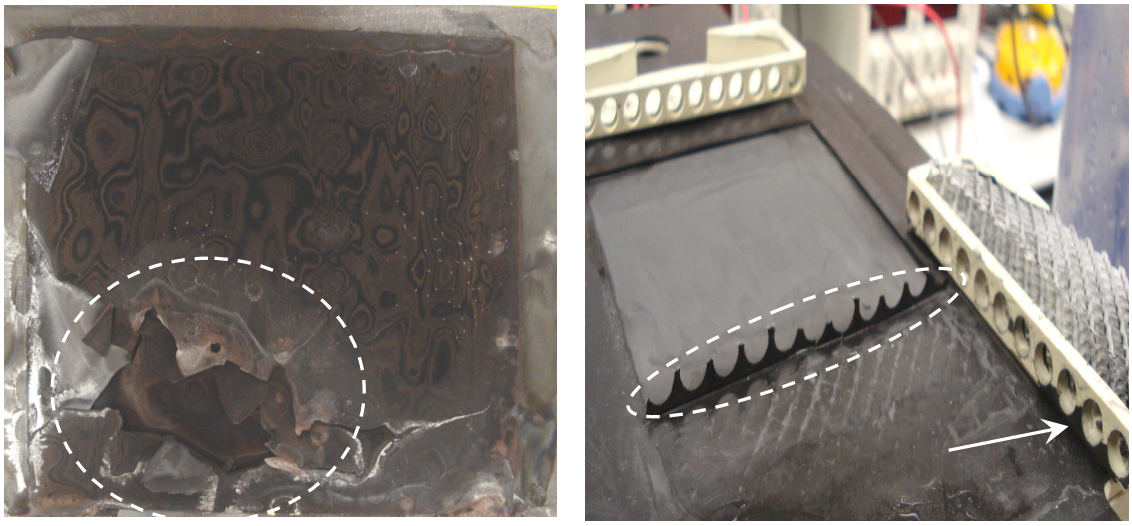

(a) (b)

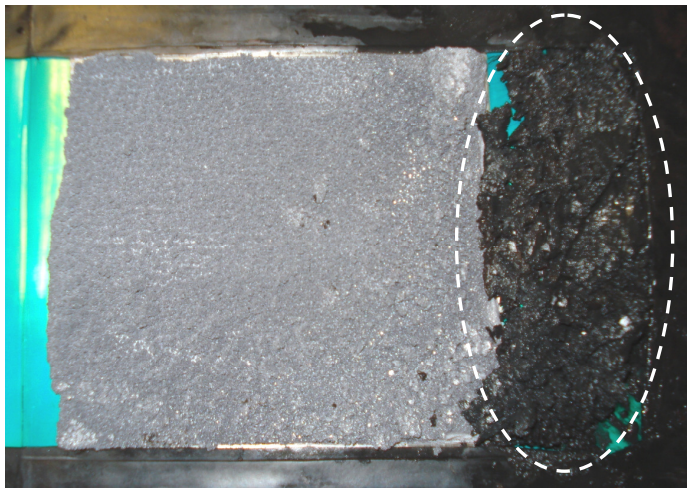

(c)

Fig 3.19: Photographs showing the lead dioxide deposits formed during operation by (a) cracks in the deposit, (b) creeping on to non-conducting surfaces and (c) sludging to the bottom of the electrolyte channel.

(b) Inefficient lead dioxide electrodeposits, are caused by factors ranging from the surface preparation technique to operational conditions. Uneven PbO_2 deposits were seen in different forms.

(a). The most common were seen in the initial stages of the development as cracks and were due to internal stress or a trapped gas bubble (Fig 3.19(a)). The number of such cracks was decreased by using an electrolyte additive (5 mmol dm^{-3} of HDTMAH) and by pumping the electrolyte at lower flow rates to reduce the formation of bubbles before the start of the experiments.

(b). The second form of powdery particulate PbO_2 deposits, produced during cell operation, crept onto the non-conducting surfaces, such as the inlet manifolds, to create a compact conducting deposit (identified in Fig 3.19(b)), which could not be dissolved into the electrolyte. This caused an electrical short-circuit. This problem was avoided by completely removing the inlet manifold.

(c). Longer operational periods resulted in a PbO_2 deposit in the form of an insoluble particulate sludge of oxides of PbO_2, which settled in the bottom of the reservoir and in areas with poor convection. This sludge formation was studied by X. Li et.al[14]. It was due to the phase change of PbO_2 from α to β, during the charge-discharge cycling to form a mixed deposit. The causes were identified as the lower lead concentrations and the overpotential associated with the positive electrode. The authors were able to avoid these deposits using chemical treatment methods with H_2O_2 to recover this undissolved PbO_2 and recycle the electrolyte to achieve normal operation[18,19].

3.4. Further work and conclusions

3.4.1. Conclusions

The preliminary studies with the 100 cm^2 test cell with the flow rig set-up have yielded successful results towards the operation of the cell for a complete pilot-scale setup. This has been started at the facilities of the project partners, C-tech Innovation Ltd., namely a

1200 cm^2 electrode-area test cell. The main results in this chapter are: modifications to the flow distribution system, optimization of the electrolyte compositions and optimisation of the control parameters. These were achieved by improved depositions through investigation of the charge-discharge performance with the 100 cm^2 flow cell set-up. Also in this work, problems associated with the cell geometry and electrode deposits were investigated.

(a). Dendritic lead deposits can form upon the application of high current densities (> 30 mA cm^{-2}) and low flow rates (≤ 2 cm s^{-1}), with an imbalanced chemistry of the Pb^{2+} ion and MSA concentrations.

(b). Creeping of particulate PbO_2 deposits onto flow distributors and the cell geometry, can cause electrical short-circuit and lead to failure of the battery. Furthermore sludge formation (insoluble phase-transformed PbO_2 deposits) during operation reduces flexibility in the operating conditions of the system.

3.4.2. Further work

Demonstration of the successful operation of a 100 cm^2 soluble lead-acid battery has provided a basis for further investigation into the use of this battery for large-scale as well as stand–alone applications. However, the following areas need a considerable degree of further research to consolidate the position of this system towards commercialisation.

(a). Testing of a stable bipolar electrode material for use in the bipolar stack assembly, without recurring problems associated with lead and lead dioxide electrode deposits.

(b). Further investigation into the cell chemistry with the use of H_2O_2 for prolonged cycling, without decreasing the concentration of lead.

(c). Investigations into the effects of current density, length of charge-discharge cycles, inter-electrode-gap, leakage current and mean linear flow rate on the cycle life using regenerative cycling with H_2O_2.

(d). Finally, the ability of the bipolar electrode stack or cell to maintain electrode deposits for prolonged periods after successive cycling with H_2O_2 should be explored further.

References

[1]. "*Review of Electrical Energy Storage Technologies and Systems and of their Potential for the UK*"**,** report carried out under DTI Technology Programme: New and Renewable Energy by EA technology first published 2004. www.berr.gov.uk/files/file15185.pdf., accessed April 24, 2011.

[2]. M. Schlensinger and M. Paunovic, "*Modern Electroplating*", 4th edition, John Wiley and Sons. Inc.© 2000.

[3]. M. Sharon, K.S. Ramaiah, M. Kumar, M. Neumann-Spallart, C. Levy-Clement, *J. Electroana. Chem*., **436** (1997) 49.

[4]. D. Brendt, *J. Pow. Sou*., **100** (2001) 29.

[5]. C.A. Vincent, B. Scrosati, "*Modern batteries: An Introduction to Electrochemical Power Sources*", Edward Arnold Ltd., London, UK, 1984.

[6]. A.L. Portela, M.L. Teijolo and G.I. Lacconi, *Electrochim. Acta*, **51** (2006) 3261.

[7]. A. Hazza, D. Pletcher and R.G.A. Wills, *J. Phy. Chem*., **6** (2004) 1773.

[8]. D. Pletcher and R.G.A. Wills, *J. Phy. Chem*., **6** (2004) 1779.

[9]. D. Pletcher and R.G.A. Wills, *J. Power Sourc.*, **149** (2005) 96.

[10]. A. Hazza, D. Pletcher and R.G.A. Wills, *J. Power Sourc.*, **149** (2005) 103.

[11]. D. Pletcher, H. Zhou, G. Kear, C.T.J. Low and F.C. Walsh, *J. Power Sourc.*, **180** (2008) 621.

[12]. D. Pletcher, H. Zhou, G. Kear, C.T.J. Low and F.C. Walsh, *J. Power Sourc.*, **180** (2006) 630.

[13]. R.G.A. Wills, J. Collins, D. Stratton-Campbell, C.T.J. Low, D. Pletcher, F.C. Walsh, *J. Appl. Chem.,* **40** (2010) 955.

[14]. X. Li, D. Pletcher, F.C. Walsh, *Electrochim. Acta*, **54**(2009) 4688.

[15]. J.P. Carr, N.A. Hampson, *Chem. Rev.*, **72** (1972) 679.

[16] H. Chang, D.C. Johnson, *J. Electrochem. Soc*., **136** (1989) 17.

[17] D. Devilliers, M.T. Dinh Thi, E. Mahé, V. Dauriac, N. Lequeux, *J. Electroanal. Chem*., **573** (2004) 227.

[18]. J. Collins, G. Kear, X. Li, C.T.J. Low, D. Pletcher, R.C. Tangirala, D.S. Campbell, F.C. Walsh, C. Zhang, *J. Power Sourc.*, **195** (2010) 2975.

[19]. J. Collins, G. Kear, X. Li, C.T.J. Low, D. Pletcher, R.C. Tangirala, D.S. Campbell, F.C. Walsh, C. Zhang, *J. Power Sourc.*, **195** (2010) 1731.

Chapter-IV

The Copper-Lead dioxide Flow Battery

4.1. Introduction

The electrochemical depositions of copper and lead are important for a wide range of applications, such as in integrated circuits, the production of bearings, electrowinning, electrically conductive tracks and decorative coatings[1,2].

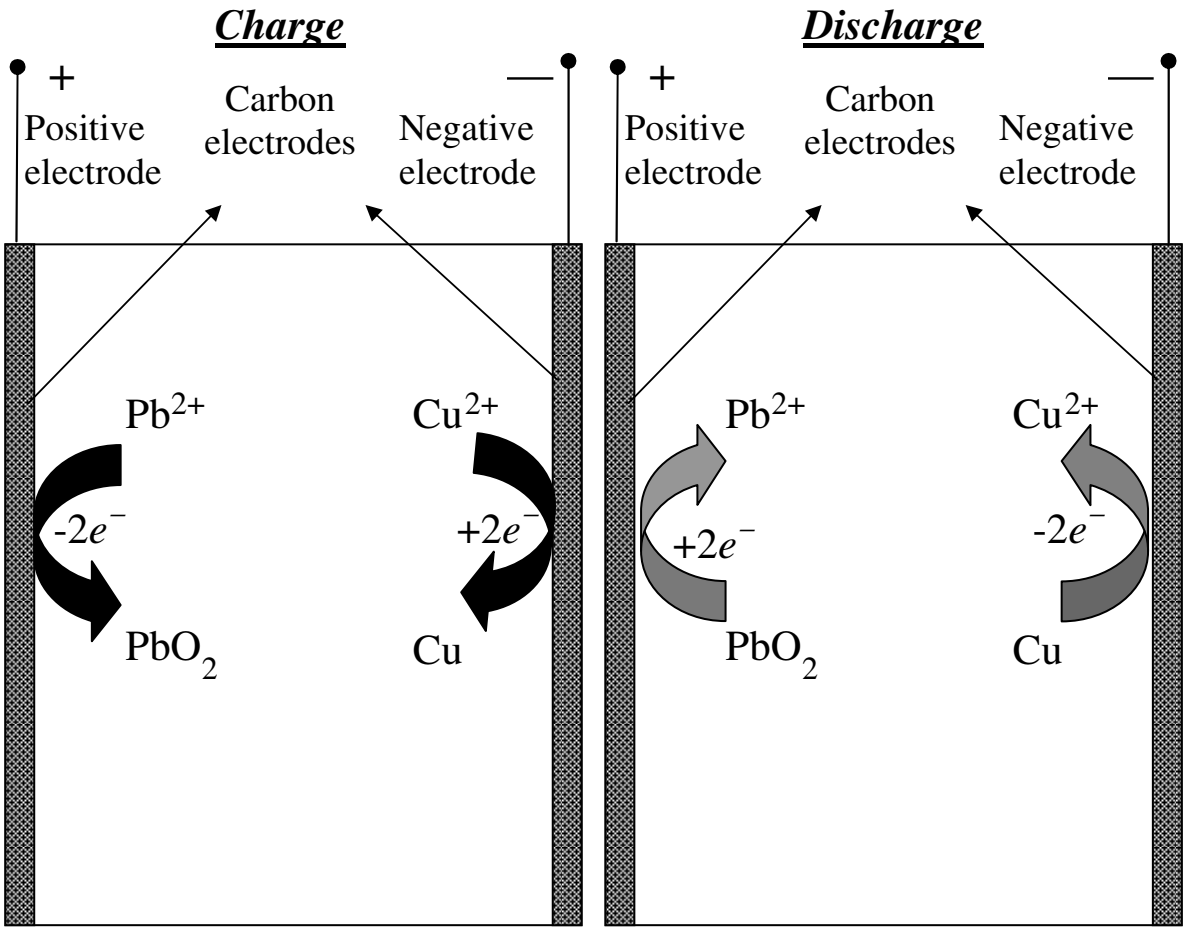

Fig 4.1: A schematic diagram showing the charge-discharge of an undivided copper-lead dioxide cell.

In industry, copper is used in copper-based solders as a replacement for lead, in copper-tin alloys, as a current collector in lithium batteries, as an anti-microbial surface protective coating and in copper-based bronzes for aesthetic surface finishes. Copper and lead are also among the most common elements recovered from effluents in the electroplating and semiconductor manufacturing industries, along with tin, cobalt and zinc[3,4]. This show that copper occupies similar status as that of lead i.e., cheap, easy availability and high

recyclability, along with good electrodepositing properties in many electrolytic combinations.

In this chapter, Cu^{2+}/Cu^{0} and Pb^{2+}/PbO_2 were considered as the redox couples for a redox flow battery (as shown in Fig 4.1), motivated by the problem of dendritic lead deposits formed in the soluble-lead acid system[5, 6]. The other half-cell redox couple, lead/lead dioxide, has been investigated for the soluble lead acid battery[8]. Lead and copper are also highly soluble in MSA[9,10]. In this electrolyte both metal ions can be contained at high concentration (up to 2 mol dm^{-3}). The primary negative and positive electrode reactions involved in the copper-lead dioxide battery are as follows:

$$Cu^{2+} + 2e^{-} \underset{\text{discharge}}{\overset{\text{charge}}{\rightleftharpoons}} Cu \qquad E^{0} = +0.34\ V\ vs.\ \text{SHE} \qquad (1)$$

$$Pb^{2+} + 2H_2O - 2e^{-} \underset{\text{discharge}}{\overset{\text{charge}}{\rightleftharpoons}} Pb_2O + 4H^{+} \qquad E^{0} = +1.7\ V\ vs.\ \text{SHE} \qquad (2)$$

These reactions indicate that the use of copper as a negative redox couple does not influence the concentration of protons, which therefore depends only on the formation of lead dioxide during charge (as is the case in the soluble lead-acid flow battery)[11]. The combination of lead and copper has a further advantage of lead-free deposits up to current densities of 120 mA cm^{-2}. It has been reported that the copper-lead dioxide cell has high charge efficiency ($\cong 90$ %), similar to that of a vanadium system, and reasonable voltage efficiency ($\cong 65\%$)[6]. These high efficiencies, together with the advantage of copper to form smooth deposits in many acidic media[7], makes the cell attractive even though the cell voltage is limited to 1.32 V. This cell voltage is comparatively lower than that of other RFBs and is due to the lower reduction potential of copper electrode, which can be improved by stacking up the cells. Hence, this combination was considered in this thesis for testing in a flow battery system.

4.2. Experimental details

Initial investigations were focused on the copper electrochemistry, followed by that of lead dioxide. Cyclic voltammetry experiments on a rotating disc electrode were performed (details as described in section 1.4.1)[12,13]. A glassy-carbon rotating disc electrode of 4 mm diameter (0.126 cm^2) was used as the working electrode, with a platinum mesh (1 cm^2) as the counter electrode in a three-electrode setup with a saturated calomel reference electrode (SCE). The glassy-carbon electrode was polished using 1 µm and 0.05 µm grades of alumina on polishing pads with water, followed by a thorough rinse with deionised water, resulting in a mirror finish surface. This process was repeated between each experiment, using clean polishing pads for each different solution to avoid cross-contamination.

Three solutions were prepared, namely:

(a) 20 mmol dm^{-3} Cu^{2+} in 1 mol dm^{-3} MSA solution,

(b) 20 mmol dm^{-3} Pb^{2+} in 1 mol dm^{-3} MSA solution and

(c) 20 mmol dm^{-3} Cu^{2+} and 20 mmol dm^{-3} Pb^{2+} in 1 mol dm^{-3} MSA.

All solutions contained excess concentrations of MSA to ensure a high electrical conductivity [0.193–0.249 Ω^{-1} cm^{-1}][11]. All data was obtained using commercial electrolyte solutions: lead methanesulfonate, 50 wt % of ($Pb(CH_3SO_3)_2$ in water (Aldrich®) and copper methanesulfonate, 36 wt % ($Cu(CH_3SO_3)_2$ in water (TIB® chemicals AG) with < 2 % of free acid concentration. These solutions could also be prepared from copper (II) carbonate (> 99 %, basic, Fluka®, Sigma-Aldrich) and lead (II) carbonate (55 %, basic, ACS, Alfa Aesar®) in methanesulfonic acid (CH_3SO_3H, 70 wt %, Sigma-Aldrich®). The related equations for the latter preparation method are as follows:

$$CuCO_3 + 2CH_3SO_3H \rightarrow Cu(CH_3SO_3)_2 + CO_2 + H_2O \quad (3)$$

$$PbCO_3 + 2CH_3SO_3H \rightarrow Pb(CH_3SO_3)_2 + CO_2 + H_2O \quad (4)$$

The stripping efficiency and the diffusion coefficients calculated via cyclic voltammetry experiments were used to compare the electrochemical characteristics of copper ions from solutions (a) and (b) above. The same methodology was used to obtain the electrochemical characteristics of lead ions with solutions (b) and (c). The stripping efficiency was calculated from the cyclic voltammograms as the ratio of the charge passed during stripping to that passed during deposition.

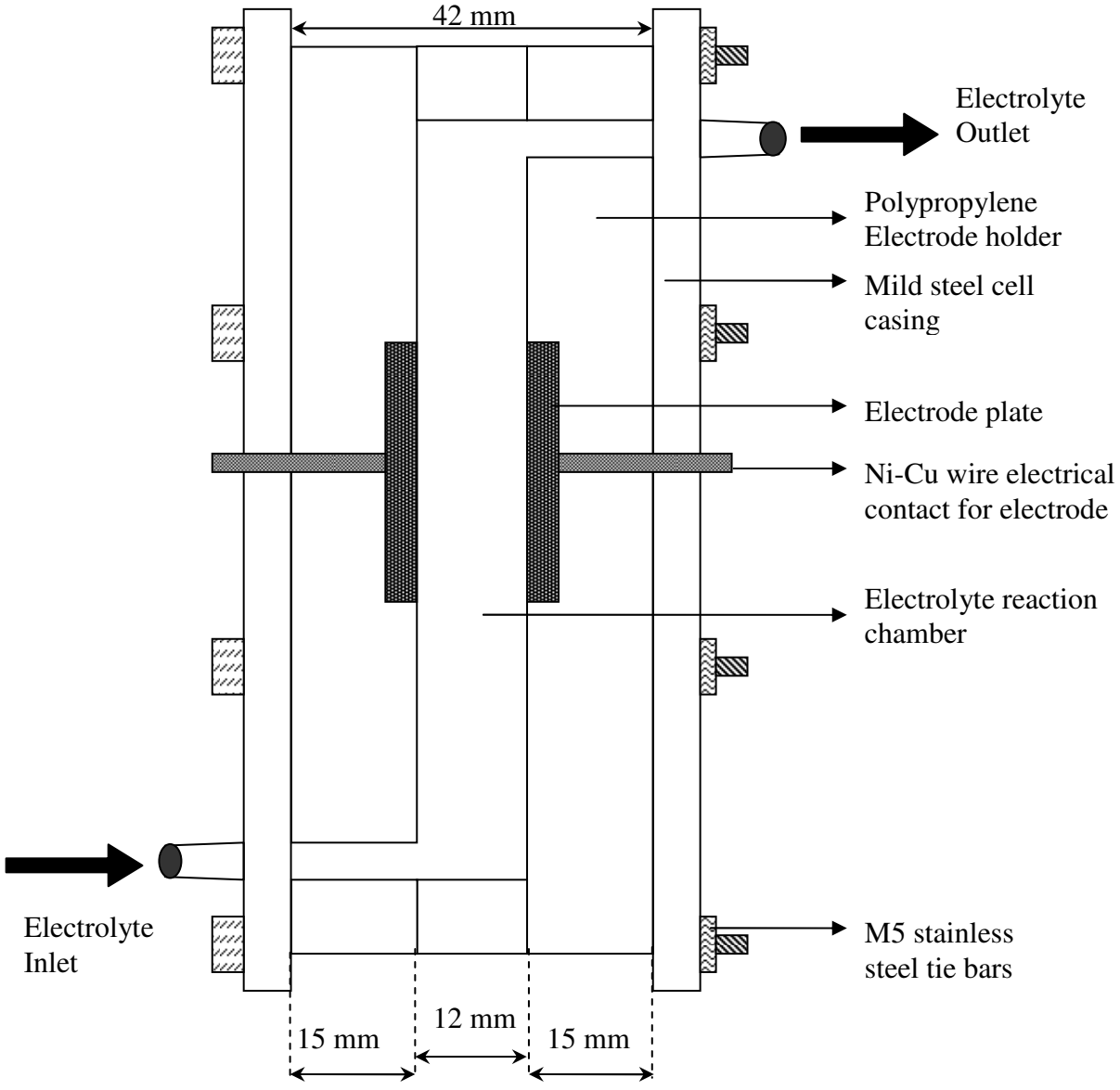

Fig 4.2. A cross sectional view of the of the 6 cm^2 surface area flow cell.

Investigations of the electrodeposition of copper and lead dioxide were also conducted using a standard Hull Cell (Kocour® Company)[14] of 0.267 dm^3 volume with an Entegris carbon polyvinyl-ester polymer plate as the cathode (45 cm^2) and the anode (22.5 cm^2). The deposition of lead and copper was carried out at a constant current using a d.c. power supply (TT*i*® CPX200 dual PSU, rated 35 V / 10 A).

Following the Hull cell deposition studies, half-cell charge-discharge experiments were performed. The current-potential curves of the individual copper and lead dioxide half-cells with a platinum counter electrode were obtained using an Autolab potentiostat and the three-electrode glass cell. The charge-discharge characteristics were used to calculate the charge and voltage efficiencies. The calculations were performed using time averages as described in *Chapter I.*

The test cell was an undivided rectangular flow cell, as shown in Fig 4.2. The cell was connected to an electrolyte tank of 0.25 dm^3 volume (Scott Duran©) through a peristaltic pump (Masterflex® Console drive, Cole-Palmer® Instruments company). The electrode was an Entegris® carbon polyvinyl-ester polymer.

4.3 Results and discussion

4.3.1. Voltammetry

The initial voltammetric investigations on a static glassy carbon electrode (0.126 cm^2) confirmed the independent deposition and stripping of copper and lead ions is possible from the 20 mmol dm^{-3} Cu^{2+} and 20 mmol dm^{-3} Pb^{2+} in 1 mol dm^{-3} MSA solution. The potential was first swept towards a negative potential from 0.5 V *vs.* SCE to −0.9 V *vs.* SCE and then to 1.9 V *vs.* SCE, before sweeping back to 0.5 V *vs.* SCE. The resulting scan showed the individual deposition of copper, which was followed by lead deposition (Fig. 4.3). During the reverse scan, the characteristic stripping peak of a metal was observed

with dissolution of lead followed by copper after which the deposition and stripping of lead dioxide occurred. This is shown in Fig 4.3. The figure shows that beyond the starting potential of 0.5 V *vs.* SCE and towards –0.9 V *vs.* SCE, the initial deposition of copper onto the glassy carbon electrode and lead deposition onto the copper deposit occurred. The reverse scan from –0.9 V *vs.* SCE towards 1.9 V *vs.* SCE shows the stripping peaks of lead and copper deposits. The deposition of lead dioxide indicated at potentials more positive than 1.89 V *vs.* SCE can also be observed. When the potential was swept back to 0.5 V *vs.* SCE, the dissolution of the lead dioxide deposit into the electrolyte can be observed. This also indicates lower and upper potential limits of –0.4 V to 1.9 V *vs.* SCE, for an investigation of stripping efficiency and calculating the diffusion coefficients of copper and lead ions via copper-lead dioxide voltammtery.

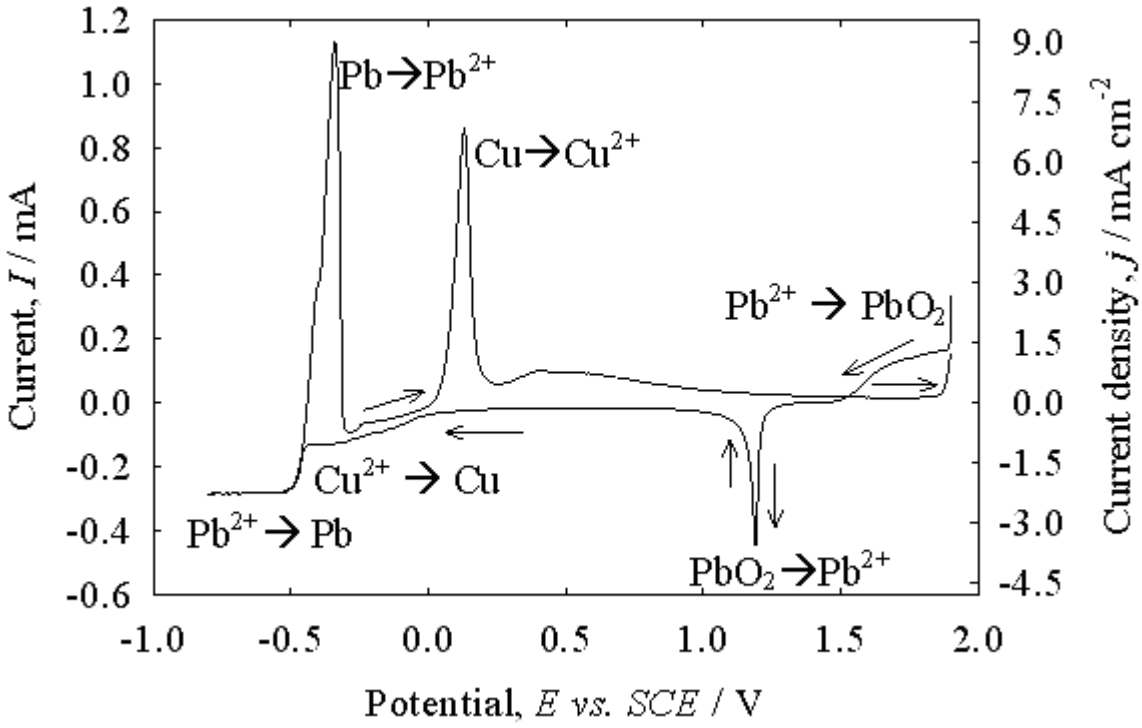

Fig 4.3: Cyclic voltammogram showing the individual deposition and stripping of copper, lead and lead dioxide during a potential sweep from 0.5 V *vs.* SCE to –0.9 V *vs.* SCE and back to +1.9 V *vs.* SCE. The solution was 20 mmol dm^{-3} Cu^{2+} and 20 mmol dm^{-3} Pb^{2+} in 1 mol dm^{-3} MSA solution. A static glassy carbon electrode of 0.12571 cm^2 at a temperature of 23ºC and a scan rate of 50 mV s^{-1} were used.

The cyclic voltammetry at controlled rotation speeds (400, 900, 1600, 2500 rpm) was carried out for solutions containing:

(a) 20 mmol dm^{-3} Cu^{2+} in 1 mol dm^{-3} MSA,

(b) 20 mmol dm^{-3} Pb^{2+} in 1 mol dm^{-3} MSA, and

(c) 20 mmol dm^{-3} Cu^{2+} and 20 mmol dm^{-3} Pb^{2+} in 1 mol dm^{-3} MSA.

The stripping efficiency of copper in solution (a) was 98 ± 0.5 % while the stripping efficiency using solution (c) was 89 ± 0.5 %. A similar experiment was performed for solutions (b) and (c). The stripping efficiency for lead dioxide in solution (b) was 76 ± 1.0 %, while the stripping efficiency in solution (c) was 48 ± 1.0 %. This shows that in solution (c), which contains both copper and lead in 1 mol dm^{-3} MSA, the stripping efficiency of copper was higher than that of lead dioxide, since lead ions inhibit smooth deposition and stripping of copper. This was observed in the subsequent voltammetry, constant-current depositions using the Hull cell and also in half–cell charge–discharge experiments.

Fig 4.4 shows the linear sweep voltammograms for copper deposition from solution (c) at 23 °C. The potential was swept from +0.4 to −0.4 V *vs.* SCE, while with solution (a) it was swept from +0.9 V to −0.9 V *vs.* SCE. With an electrolyte containing 20 mmol dm^{-3} Cu^{2+} and 20 mmol dm^{-3} Pb^{2+} in 1 mol dm^{-3} MSA, the copper deposition was restricted to the range +0.4 V to −0.4 V *vs.* SCE, whilst it deposits until potentials more negative than −0.4 V *vs.* SCE in that of solution (a) with only copper ions.

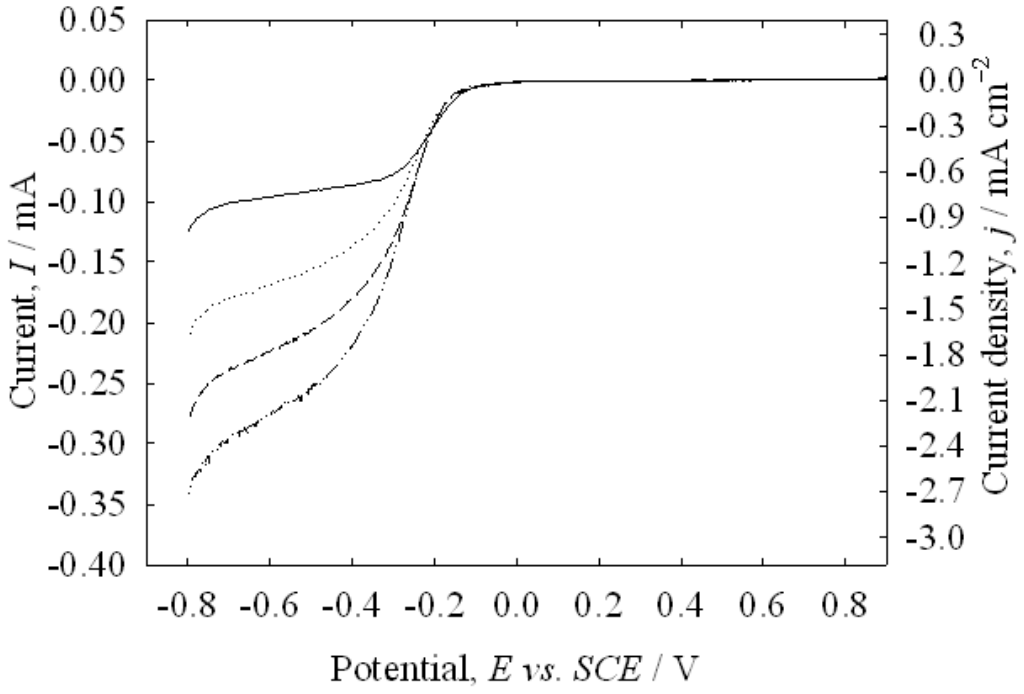

(a)

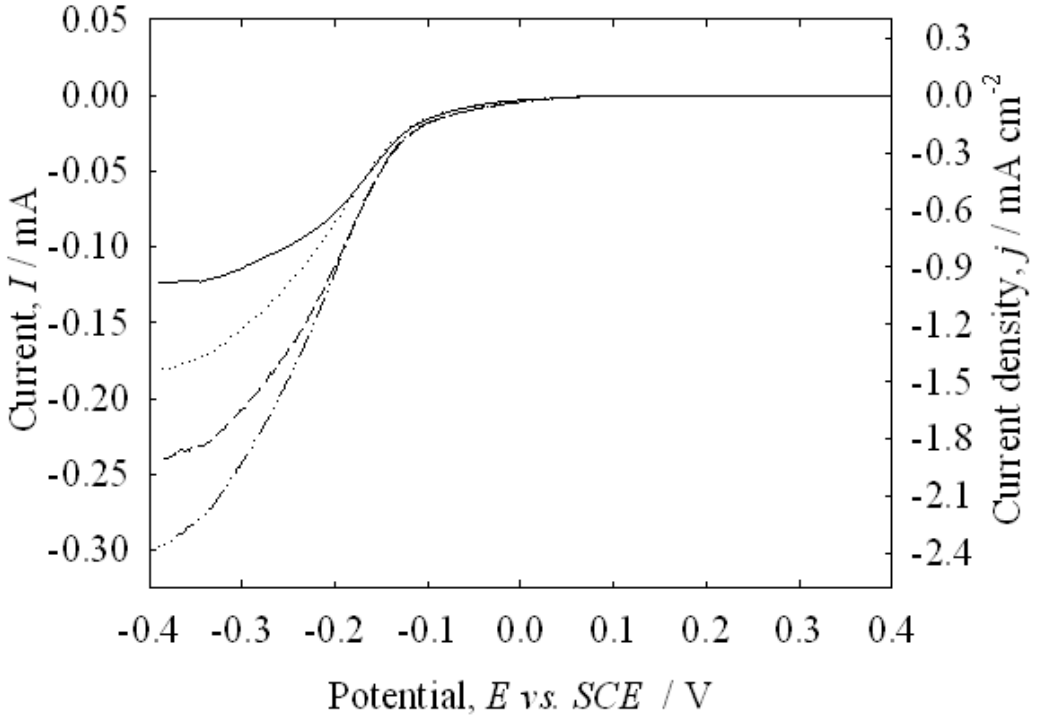

(b)

Fig 4.4: Linear sweep voltamograms showing the deposition of copper from: (a) 20 mmol dm^{-3} Cu^{2+} in 1 mol dm^{-3} MSA; (b) 20 mmol dm^{-3} Cu^{2+} and 20 mmol dm^{-3} Pb^{2+} in 1 mol dm^{-3} MSA solution onto a 0.12571 cm^2 glassy carbon RDE at speeds of (—) 400 rpm, (---) 900 rpm, (·····) 1600 rpm and (-·-·-) 2500 rpm at temperature of 23 ºC and a scan rate of 50 mV s^{-1}.

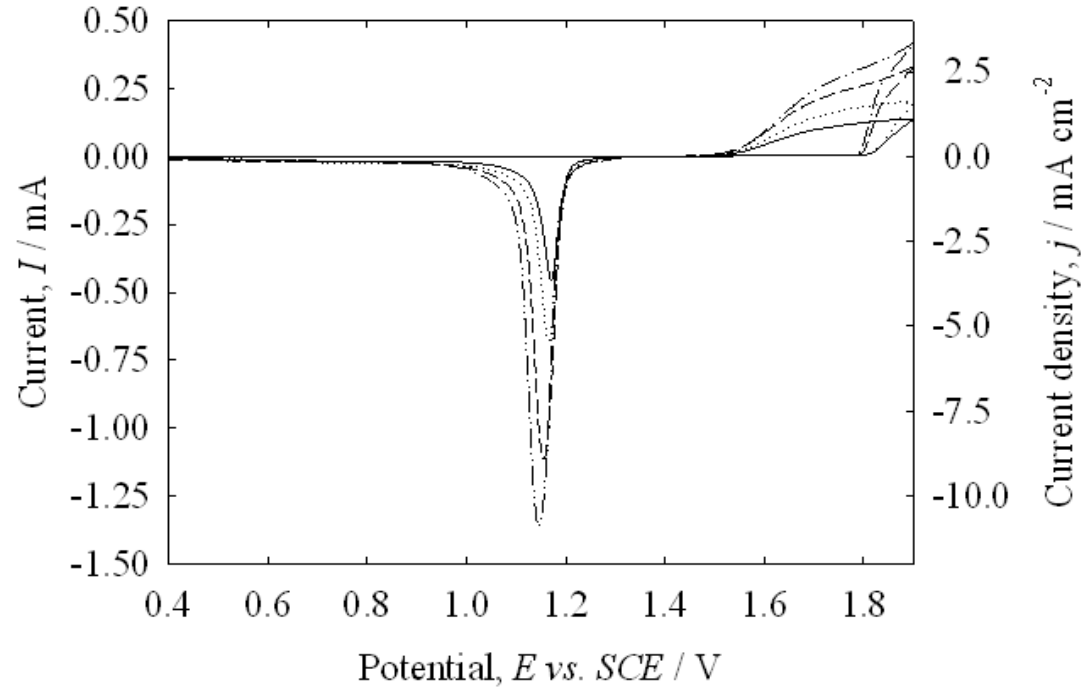

(a)

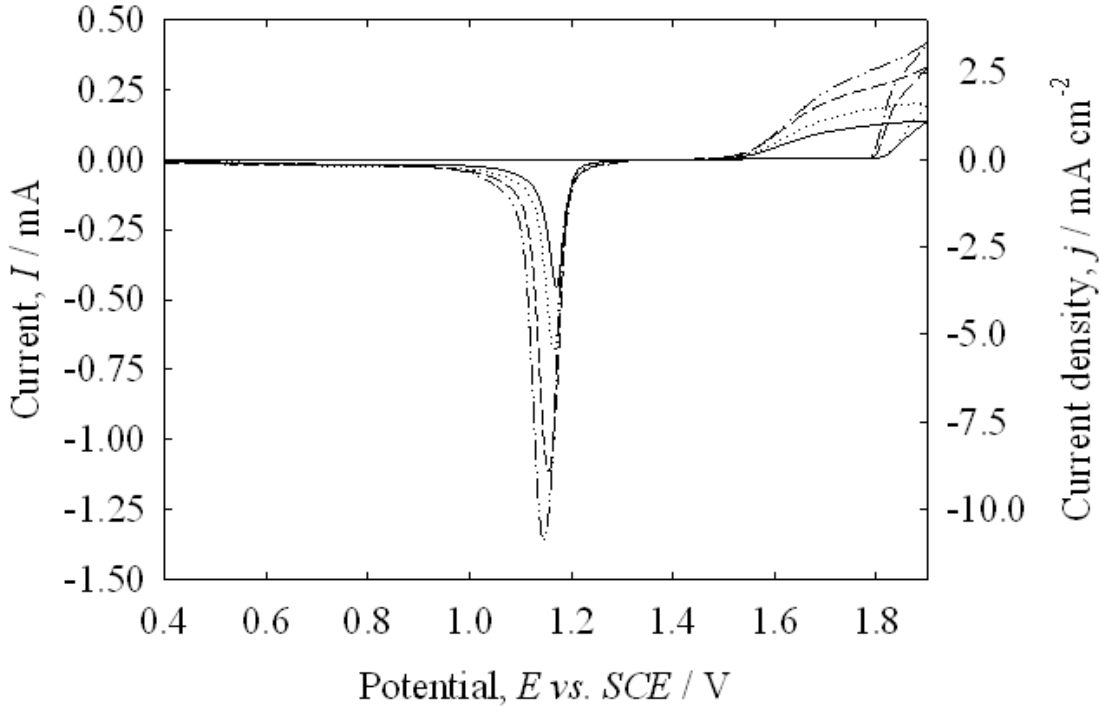

(b)

Fig 4.5: Cyclic voltamograms showing the deposition of lead dioxide from: (a) 20 mmol dm^{-3} Pb^{2+} in 1 mol dm^{-3} MSA; (b) 20 mmol dm^{-3} Cu^{2+} and 20 mmol dm^{-3} Pb^{2+} in 1 mol dm^{-3} MSA solution onto a 0.12571 cm^2 glassy carbon RDE at controlled rotation speeds of (—) 400 rpm, (---) 900 rpm, (·····) 1600 rpm and (-·-·-) 2500 rpm at a temperature of 23ºC and a scan rate of 50 mV s^{-1}.

In solution (c) (Fig 4.4(b)) copper starts to deposit at −0.09 V *vs.* SCE, which is nearly 40 mV less negative than in the case of copper as a single electroactive species in solution[15]. Hence, the presence of lead ions as well as the lower electrodepositon potential of copper contribute to a lower cell voltage for this battery. This behaviour is not observed from copper ions in the cyclic voltammetry of lead/lead dioxide, where the curves remain unaltered and follow an identical deposition and stripping pattern to that with only the lead solution (b). The lead-dioxide deposition and stripping patterns for Pb^{2+} ions from solutions (b) and (c) are shown in Fig 4.5.

Steady state linear sweep and cyclic voltamograms from the curves on Fig 4.4 and 4.5 were compared using the Levich plot for laminar flow at a flat rotating disc electrode, from which the diffusion coefficients for Cu^{2+} and Pb^{2+} ions were calculated[16]:

$$I_L = 0.62nFAD^{2/3}\omega^{1/2}\nu^{-1/6}c \qquad (5)$$

where I_L is the limiting current (mA), n is number of electrons transferred, F is the Faraday constant (C mol^{-1}), A is the surface area of the electrode (cm^2), D is the diffusion coefficient of Pb^{2+} or Cu^{2+} ions in the electrolyte ($cm^2\ s^{-1}$), ω is the rotation speed (rad s^{-1}), ν is the kinematic viscosity of the reactant ions ($cm^2\ s^{-1}$) and c is the concentration of the electroactive species (mol cm^{-1}).

The Levich plot for copper and lead dioxide deposition in Figure 4.6 shows complete mass-transport controlled deposition of both Cu^{2+} and Pb^{2+} from solution (c). For the purpose of comparison, similar curves were obtained for solutions (a) and (b), and from equation (5) the diffusion coefficient for the Cu^{2+} ion in solution (a) was calculated to be $4.8 \pm 0.4 \times 10^{-6}$ $cm^2\ s^{-1}$, while that in solution (c) at −0.4 V *vs.* SCE was found to be 5.1

$\pm$ 0.5 x 10^{-6} cm^2 s^{-1}. Similarly, the diffusion coefficient for Pb^{2+} ion (lead/lead dioxide) in solution (b) was 7.4 $\pm$ 0.7 x 10^{-6} cm^2 s^{-1} and in solution (c) was 6.4 $\pm$ 0.4 x 10^{-6} cm^2 s^{-1}.

From these values, calculated at a potential of 1.83 V *vs.* SCE, the diffusion coefficient for the Pb^{2+} ion in a solution containing Cu^{2+} ions was a factor of 13.5 % lower compared to the value with only Pb^{2+} ions, and these values are similar to those reported in the literature for Pb^{2+} ions in 2 mol dm^{-3} methanesulfonic acid (6.1 x 10^{-6} cm^2 s^{-1}) during the reduction of Pb^{2+} ions[11]. These values also reflect the fact that the presence of lead ions increases the rate of deposition of copper ions.

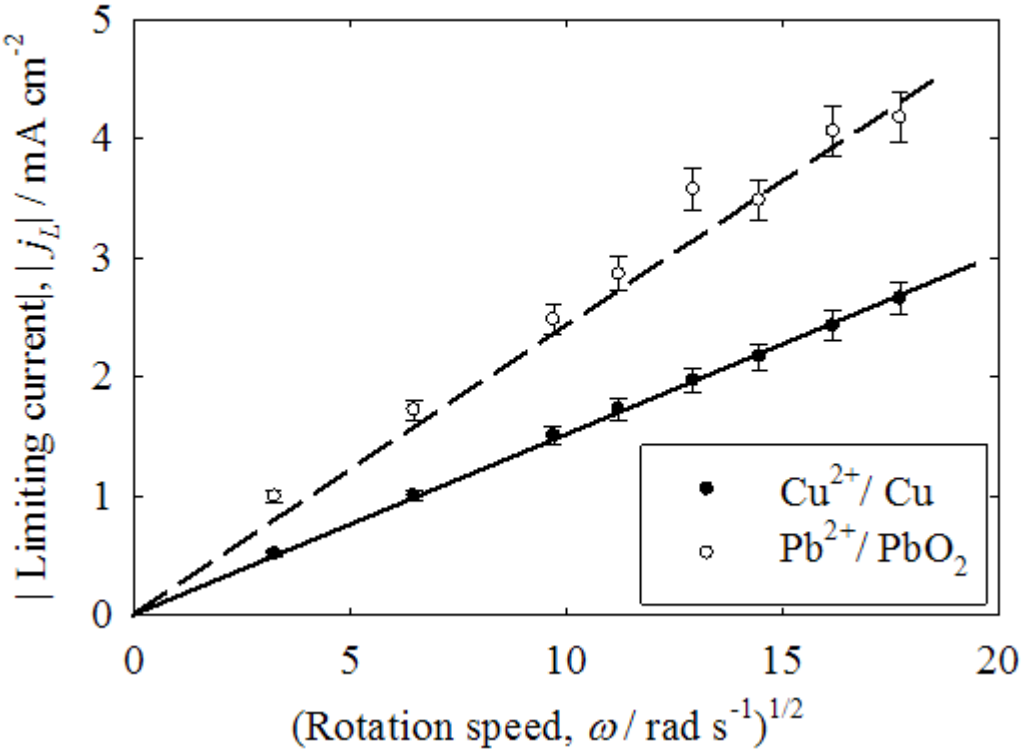

Fig 4.6: Levich plot (with 10 % error indication) for (**—,** ●) copper and (**---, O**) lead ions from 20 mmol dm^{-3} Cu^{2+} and 20 mmol dm^{-3} Pb^{2+} in 1 mol dm^{-3} MSA solution *vs.* rotation speed on to a 0.126 cm^2 glassy carbon rotating disc electrode at a temperature of 23 ºC and a scan rate of 50 mV s^{-1}

4.3.2. Hull cell experiments

Three electrolytes were used for the hull cell experiments: (1) 0.5 mol dm^{-3} Cu^{2+} in 1 mol dm^{-3} MSA; (2) 0.5 mol dm^{-3} Pb^{2+} in 1 mol dm^{-3} MSA; and (3) 0.5 mol dm^{-3} Cu^{2+} with 0.5 mol dm^{-3} Pb^{2+} in 1 mol dm^{-3} MSA. These electrolytes were subjected to copper and lead dioxide electrodeposition at constant currents of 2 A, 3 A and 5 A for each solution.

The aims of these experiments were: (a) to determine a common current density at which smooth metal/metal oxide depositions takes place; (b) to investigate the traces of lead depositions at current densities where smooth copper deposition is observed (similarly on the lead dioxide deposition for copper trace); and (c) to estimate the maximum current density at which secondary deposition is initiated.

Once the metal was deposited, the samples were thoroughly washed and rinsed with deionised water and placed in a desiccator for two days for completely drying. These deposits were subjected to scanning electron microscopy (SEM) and energy dispersive x-ray (EDX) analysis at specific regions of interest. The first technique was used to observe the surface morphology and the latter to find the composition. The current densities indicated were measured using a standardised Hull cell measuring scale provided by the manufacture.

During the experiments with 0.5 mol dm^{-3} Cu^{2+} in 1 mol dm^{-3} MSA, the copper deposits were found to be very smooth and reflective at low current densities (40 – 60 mA cm^{-2}) but at high current densities (> 80 mA cm^{-2}), the surface became nodular. Dendrite formation occurred at the edge of the electrode, which experienced current densities ≥ 120 mA cm^{-2}. On application of a constant current of 5 A for copper deposition in a solution with lead (0.5 mol dm^{-3} Cu^{2+} with 0.5 mol dm^{-3} Pb^{2+} in 1 mol dm^{-3} MSA), nodular patterns were not

evident until the current density reached approximately 200 mA cm^{-2}. This might be due to the capacity of lead ions to suppress dendrite formation and to produce smooth deposits. The SEM image in Fig 4.7 for the 0.5 mol dm^{-3} Cu^{2+} and 0.5 mol dm^{-3} Pb^{2+} in 1 mol dm^{-3} MSA electrolyte shows a surface morphology similar to that of copper. As the applied current was increased the crystalline structure expanded and covered a greater surface area of the electrode. As the applied current increases the amount of material deposited also increases, consistent with Faraday's law.

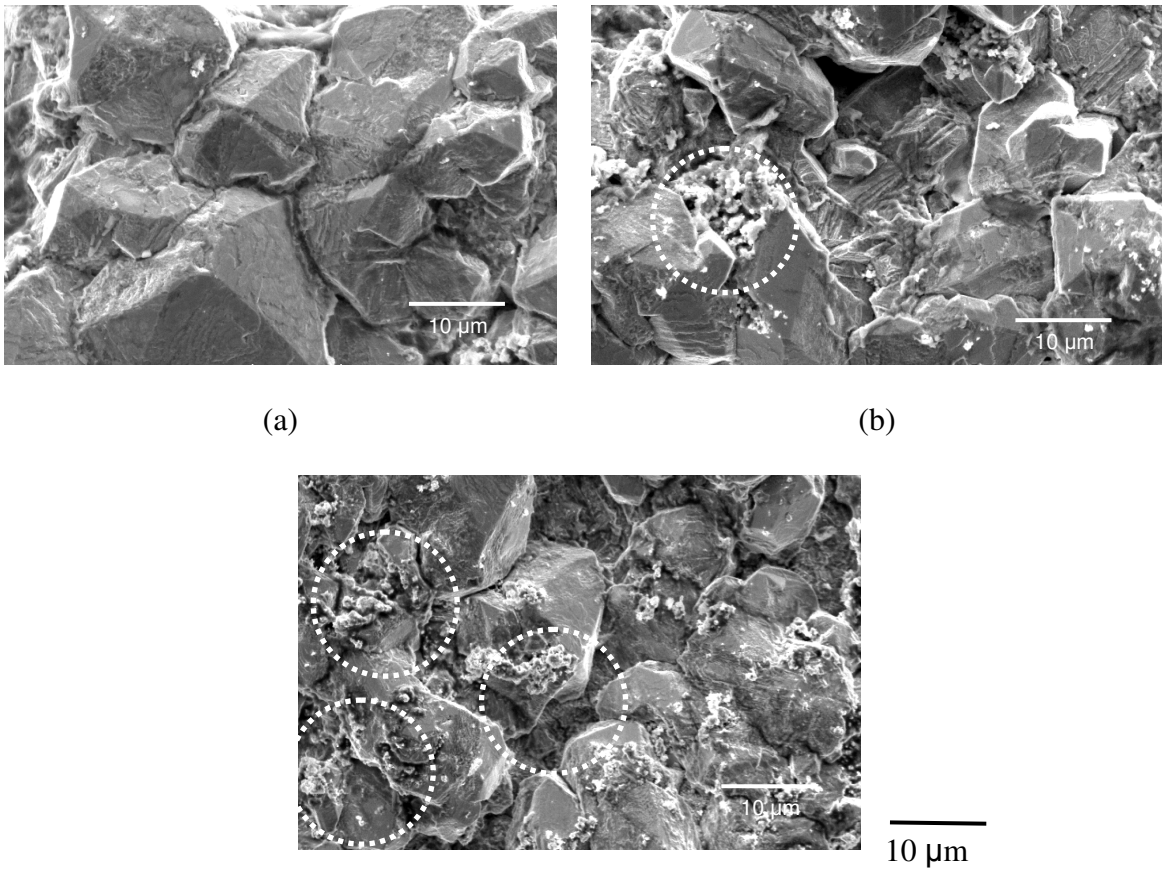

Fig 4.7: Scanning electron microscope images of samples deposited using an electrolyte with 0.5 mol dm^{-3} Cu^{2+} and 0.5 mol dm^{-3} Pb^{2+} in 1 mol dm^{-3} MSA (a) at 60 mA cm^{-2}; (b) at 80 mA cm^{-2};and (c) at 120 mA cm^{-2}, for a current of 5 A.

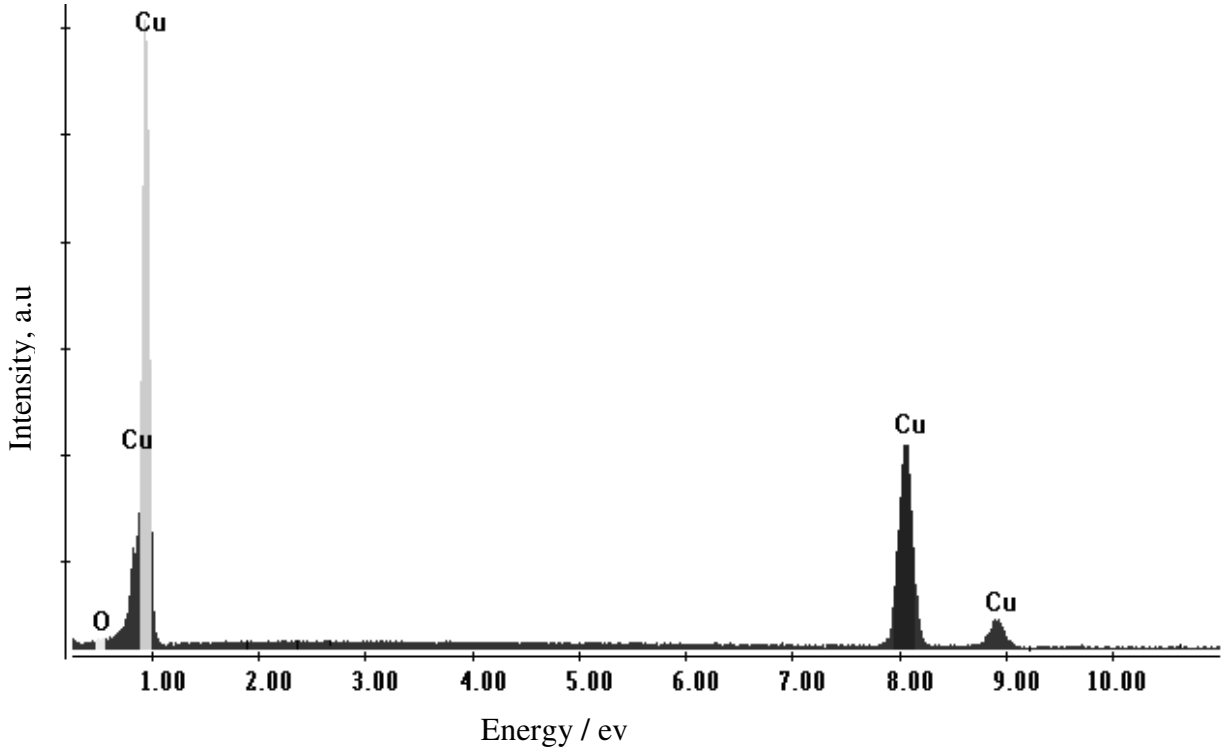

(a)

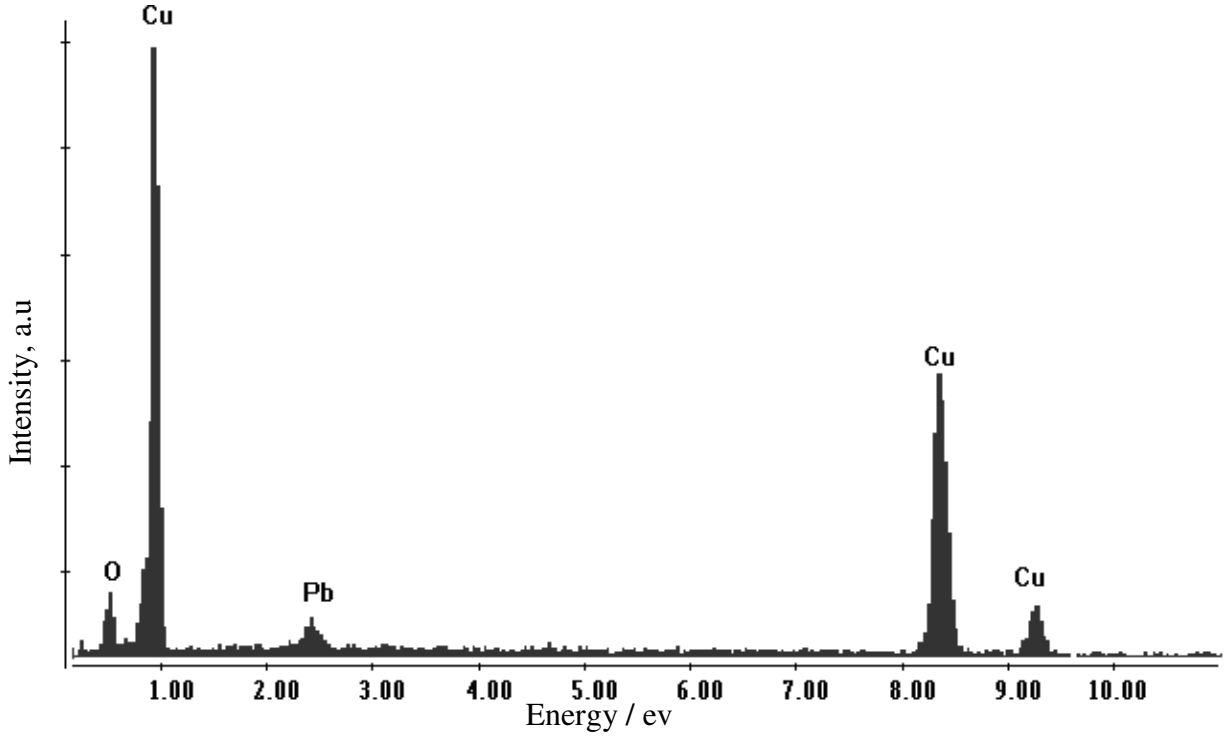

(b)

Fig 4.8: Energy dispersive X-ray analysis spectra showing the level of the elements deposits for 0.5 mol dm^{-3} Cu^{2+} and 0.5 mol dm^{-3} Pb^{2+} in 1 mol dm^{-3} MSA at constant currents of (a) 1 A and (b) 5 A.

In the solution with 0.5 mol dm^{-3} Cu^{2+} and 0.5 mol dm^{-3} Pb^{2+} in 1 mol dm^{-3} MSA, current densities of less than |100| mA cm^{-2} favour the formation of smooth copper deposits on the cathode surface. The depositions performed at these current densities (≤ |80| mA cm^{-2}) showed large polygonal shaped crystallite copper deposit. These formations grew with the increasing current density and nodules of lead deposits were seen beyond ≥ |100| mA cm^{-2} (encircled in Fig 4.7 (b & c)). To show the effect of higher current deposition, the surface structure was also observed under the SEM for samples deposited at constant currents of 3 A and 5 A for a constant current density of 120 mA cm^{-2}.

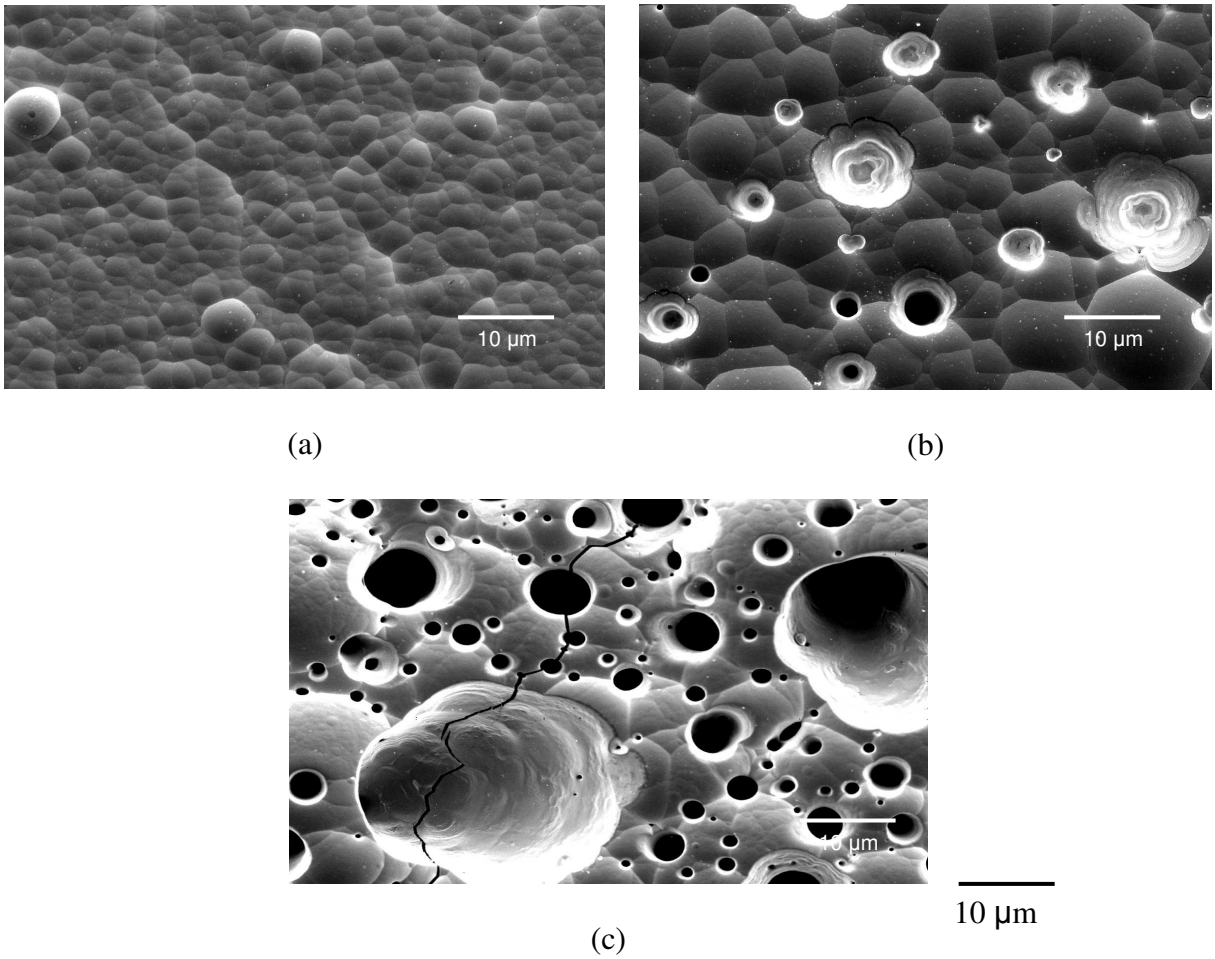

(a) (b)

(c)

Fig 4.9: Scanning electron microscopy (SEM) images of lead dioxide samples deposited at a constant current of 5A from 0.5 mol dm^{-3} Cu^{2+} and 0.5 mol dm^{-3} Pb^{2+} in 1 mol dm^{-3} MSA electrolyte at a current density of: (a) 25 mA cm^{-2}; (b) 45 mA cm^{-2} ; and (c) 60 mA cm^{-2}.

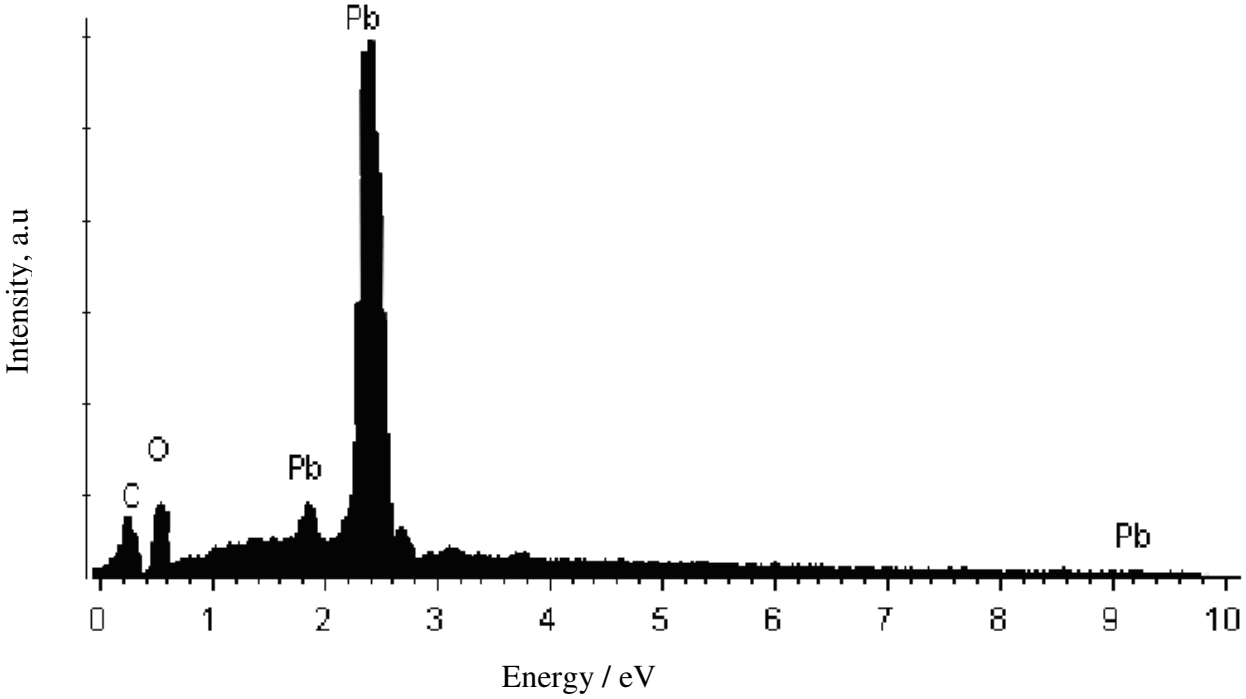

(a)

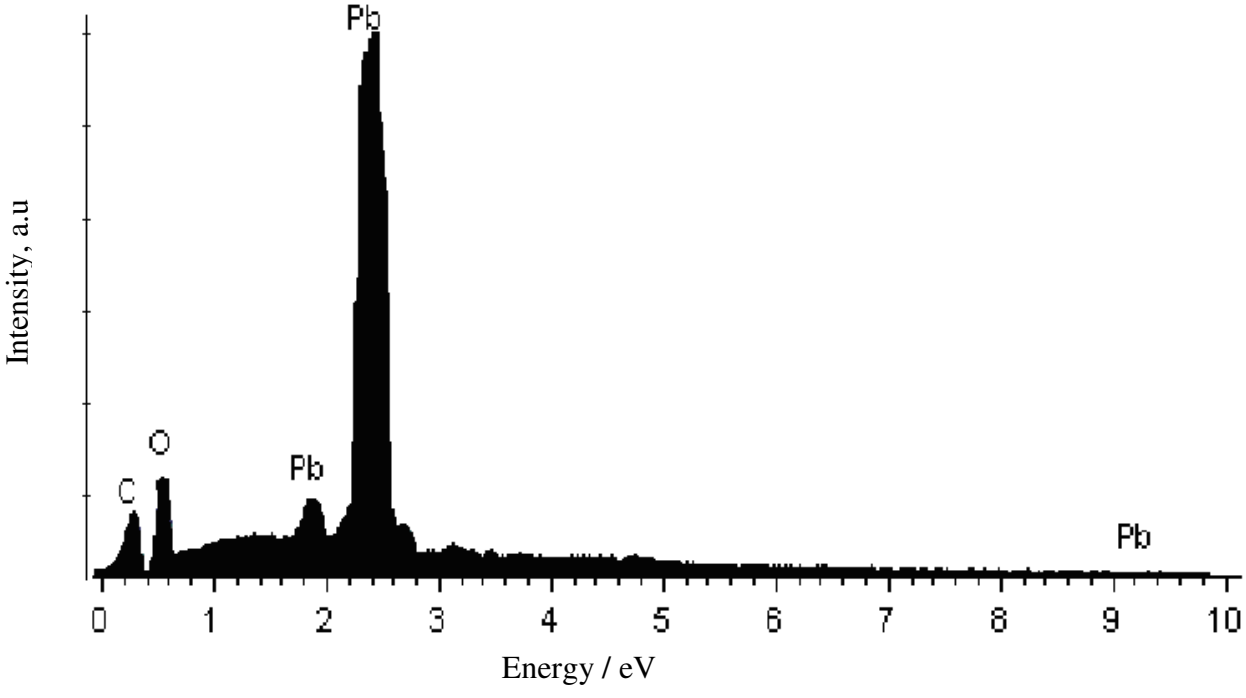

(b)

Fig 4.10: Energy dispersive X-ray analysis spectra showing the level of the elements in the deposition for 0.5 mol dm^{-3} Cu^{2+} and 0.5 mol dm^{-3} Pb^{2+} in 1 M MSA at constant currents of (a) 1 A and (b) 5 A.

The comparative spot EDX analysis for the copper depositions at currents of 2 A and 5 A (as shown in Fig 4.8) suggest that a small amount of lead (< 0.3 %) was co-deposited with copper at high current densities (>120 mA cm^{-2}). This co-deposit (as show n Fig 4.8) was not observed at lower current densities. In the case of the lead dioxide deposition, a similar comparison was made to observe the deposit and any traces of copper.

The SEM images in Fig 4.9 show that beyond a current density of 60 mA cm^{-2} the lead dioxide deposit tends to be porous yet compact[17]. Although at lower current densities (≤ 45 mA cm^{-2}) the electrodeposit was compact and crystallite, at higher current densities (≥ 50 mA cm^{-2}) pitting and cracking occurred due to the internal stress in the deposit formation, making it rough. At these current densities oxygen evolution can be observed, with gas bubble formation on the surface. This can be seen clearly in the form of small holes on the surface of the electrode deposit; a similar pattern is observed on deposits from a solution with 0.5 mol dm^{-3} Pb^{2+} in 1 mol dm^{-3} MSA[18,19].

The lead dioxide deposit is known to crack and have a porous structure without the use of any additives[18,19], but there is much interest in observing any traces of copper deposition at higher current densities. Hence, SEM (Fig 4.9) and EDX (Fig 4.10) analysis were performed for current densities beyond 60 mA cm^{-2}. The analysis showed that the deposit had no traces of copper, which showed that it was essentially a pure lead dioxide deposit.

4.3.3. Charge-discharge experiments

4.3.3.1. Experiments in a three-electrode cell

The three-electrode cell was fitted with a glassy carbon rotating-disc electrode of surface area 0.126 cm^2 and filled with 0.11 dm^{-3} of 0.5 mol dm^{-3} Cu^{2+} and 0.5 mol dm^{-3} Pb^{2+} in 1

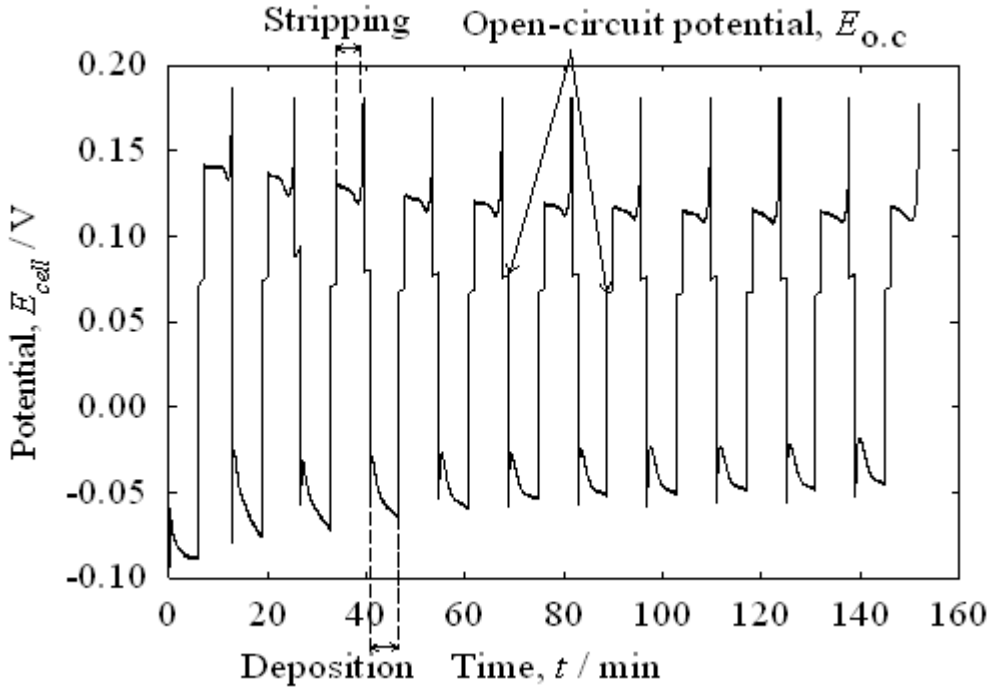

(a)

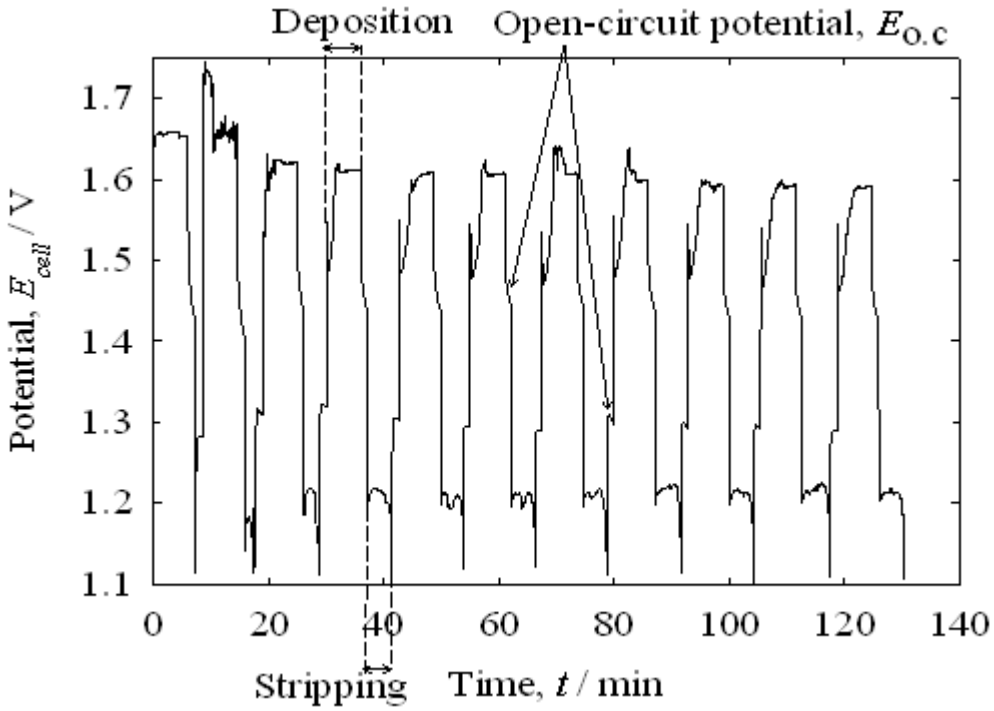

(b)

Fig 4.11: Half-cell charge-discharge sequence at 23℃ for (a) copper (negative) between the limits of −0.1 V and +0.2 V *vs.* SCE and (b) lead dioxide (positive) electrode between limits of +1.1 V and +1.75 V *vs.* SCE. in a 0.5 mol dm^{-3} Cu^{2+} and 0.5 mol dm^{-3} Pb^{2+} in 1 mol dm^{-3} MSA electrolyte for a 5 min charge-discharge sequence at a current density of 30 mA cm^{-2} on a 0.126 cm^2 glassy carbon electrode.

mol dm^{-3} MSA electrolyte. A 5 min charge-discharge experiment was carried out at a constant current density of 20 mA cm^{-2}.

The charge-discharge performance is shown in Fig 4.11 (a) and (b). The charge efficiencies for each of the cycles were calculated, which showed that copper deposition took place with an efficiency of 90 % to 95 %, similar to the values reported in the literature[7]. The lead dioxide efficiency improved after the 3rd cycle from 40 % to 85 % then settled to values between 85 % to 89 %, consistent with literature values of around 90 %[11]. This inequality in the individual half-cell efficiencies limits the total average cell charge efficiency to 82−89 %. This charge efficiency was similar to that of the soluble lead acid battery[20] but the average voltage efficiency of the copper-lead dioxide battery was low, at 58 %.

4.3.3.2. Experiments in a flow cell

Tests were carried out on an undivided rectangular parallel plate flow cell with 6 cm^2 electrodes and an inter-electrode gap of 1.2 cm (shown in Fig 4.2). Initial experiments at higher concentrations of copper and lead (1 mol dm^{-3}) did not yield any charge-discharge performance, due to an electrical short circuit caused by the lead dioxide flakes. The concentrations of the electroactive species were subsequently reduced to 0.5 mol dm^{-3} Cu^{2+} and 0.5 mol dm^{-3} Pb^{2+} in 1 mol dm^{-3} MSA.

On comparison to the soluble lead acid battery the charge efficiency was high but the voltage efficiency was low, which yields a lower total energy efficiency for the copper-lead flow battery. Beyond the 83rd cycle, the cell performance deteriorated and the average voltage efficiency was < 50 %. The electrolyte completely turned black, with lead dioxide shedding during the charge-discharge process.

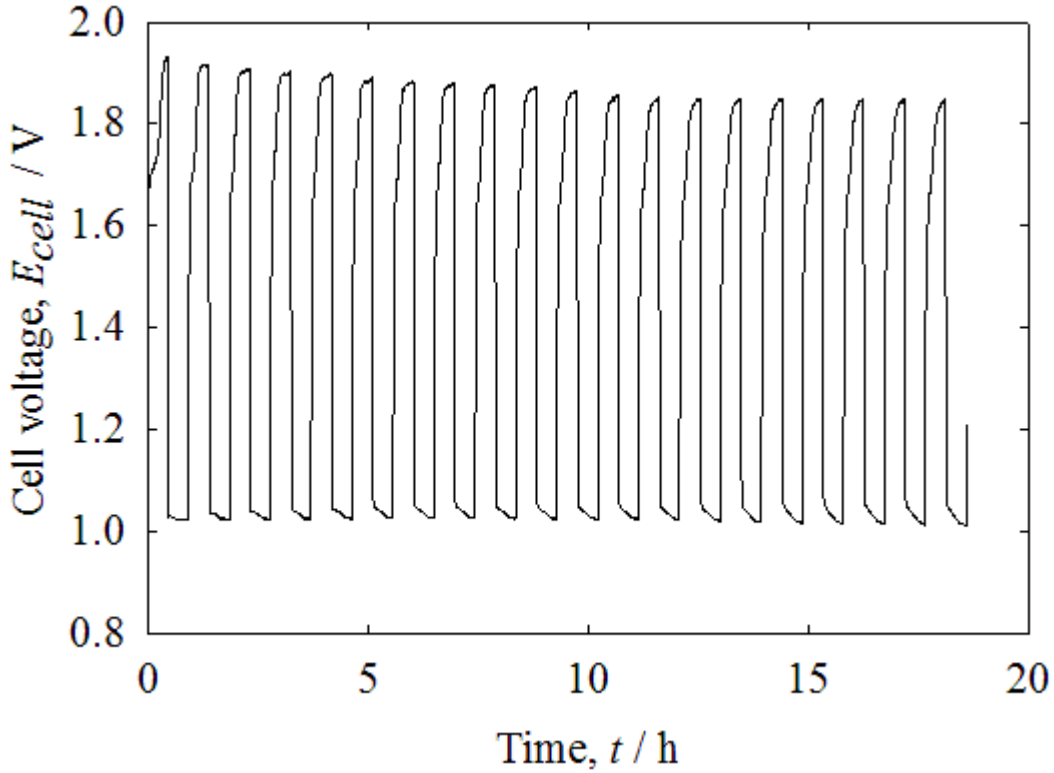

Fig 4.12: Charge-discharge sequence for a 100 cm^2 electrode flow cell from 0.5 mol dm^{-3} Cu^{2+} and 0.5 mol dm^{-3} Pb^{2+} in 1 mol dm^{-3} MSA electrolyte for a 0.5 hour charge period followed by a constant current density discharge at 20 mA cm^{-3},with a cut-off value at 1 V.

The porous flakes of lead dioxide in the bottom of the tank were similar in appearance to the lead dioxide deposit on the electrode, but the electrode with copper deposition remained compact and shiny. This can be due to the charge imbalance produced by the inefficiency of the lead dioxide electrode to completely dissolute the electrodeposits or the phase of the deposit formation.

A similar charge-discharge test for 20 cycles (Fig 4.12) was conducted to observe the performance of the battery on a 100 cm^2 test cell at a flow rate 4 cm s^{-1} and a current density of 20 mA cm^{-2} with an inter-electrode gap of 1.2 cm. The charge and discharge periods were 0.5 h and the same solution (0.5 mol dm^{-3} Cu^{2+} and 0.5 mol dm^{-3} Pb^{2+} in 1 mol dm^{-3} MSA) was used. The cycles showed a regular, repeatable charge-discharge

performance with an average charge efficiency of 88 % and an average voltage efficiency of 54 %. The performance was similar to that of the small scale (6 cm^2) test cell.

4.3.4. Testing of additives

Due to the lower voltage efficiency (≅ 60 %) and porous deposition of lead dioxide, the battery was tested using various additives for the individual copper and lead dioxide depositions. Variable acid concentrations for the electrolyte were also considered, since lead dioxide deposition is highly sensitive to the acid concentration in the solution.

Name of the additive	Quantity	Electrode	Application
Polyethylene glycol (PEG 20,000)	0.5 gm dm^{-3}	Copper	1. Proton reduction 2. Possible compact and large grain sized deposits
Cl^- (NaCl or HCl)	50 gm dm^{-3}		
Polytetraflouroethylene (Disperse PTFE-30%)	20 gm dm^{-3}	Lead dioxide	Improves life time of the electrode (due to high electrochemical stability)
Hexadecyltrimethylammonium Hydroxide (10 % in water)	0.5 mmol dm^{-3}		Improved electrodeposition (proven usage in SLA battery)
Methanesulfonic acid (MSA)	1 mol dm^{-3}		Uniform, compact, and high quality deposition

Table 4.1: List of additives used and their respective quantities for testing the copper–lead dioxide flow battery.

The additives used in testing the battery are listed in Table 4.1. The first two namely; polyethylene glycol (PEG 20,000) and chloride (Cl^-), were used for the copper electrode deposition[21-27]. Hexadecyltrimethylammonium hydroxide (HDTMAH)[19, 28] and polytetrafluro ethylene (PTFE)[29] with various concentrations of MSA[19] were used for the

lead dioxide deposition. The copper additives do not influence the PbO_2 deposition and vice versa[30, 31]. The amount used is given in the table 4.1, along with the specific reason why the additive was used.

Additive combination with 0.5 mol dm^{-3} Cu^{2+} and 0.5 mol dm^{-3} Pb^{2+} electrolyte	**Number of operational cycles out of 25 cycles**	**% Charge efficiency**	**% Voltage efficiency**
1 mol dm^{-3} MSA	24	95	65
50 gm dm^{-3} Cl^-	12	93	55
0.5 mmol dm^{-3} HDTMAH + 0.5 gm dm^{-3} PEG + 50 gm dm^{-3} Cl^-	8	96	48
0.5 gm dm^{-3} PTFE + 0.5 gm dm^{-3} PEG + 50 gm dm^{-3} Cl^-	7	95	45
0.5 mmol dm^{-3} HDTMAH	3	96	50
No additive	1 (failed to discharge)	-	-

Table 4.2: Table showing the successful combinations of additives, with their performance in charge and voltage efficiency values tested in a 6 cm^2 electrode for 10 min charge and a constant current density discharge at 20 mA cm^{-2} with a cut of value of 0.8 V.

The additives were used individually as well as in combination. Each additive combination was tested in a 6 cm^2 cell, initially used in the electrolyte tests. A set of 25, 10 minute charge-discharge cycles at 20 mA cm^{-2} were conducted for each combination, with an electrolyte composition of 0.5 mol dm^{-3} Cu^{2+} and 0.5 mol dm^{-3} Pb^{2+}. The discharge cut-off voltage was 0.8 V, while the charge cut-off was set to 2 V. The average voltage, charge and energy efficiencies were calculated for each case and compared in Table 4.2. The combinations of (HDTMAH + PEG + Cl^-), (PTFE + PEG + Cl^-), HDTMAH, Cl^- and altering the excess acid concentration of 1 mol dm^{-3} MSA, yielded a reasonable performance. The rest of the combinations did not provide any charge-discharge

performance data; cases include no electrodeposits, heavy shedding and no discharge profile.

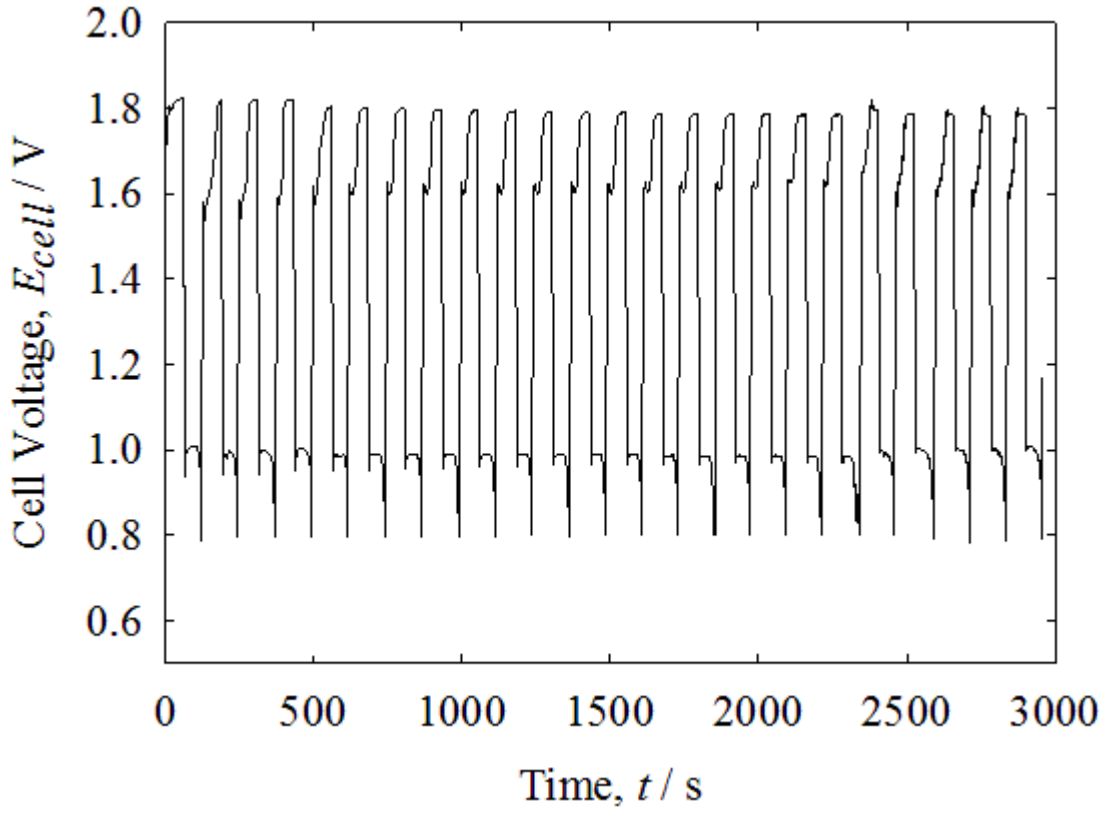

Fig 4.13: Charge-discharge performance for a 6 cm^2 electrode cell employing 0.5 mol dm^{-3} Cu^{2+} and 0.5 mol dm^{-3} Pb^{2+} in 1 mol dm^{-3} MSA electrolyte for 10 min charging and a constant current density discharge at 20 mA cm^{-2} with a cut off cell voltage of 0.8 V.

The combinations of (HDTMAH + PEG + Cl^-), (PTFE + PEG + Cl^-), HDTMAH, Cl^- were not successful in the long-term test (especially in 100 cm^2 test cell), due to the excessive formation of insoluble lead oxide(s) deposits, also seen in the soluble lead acid flow battery. The excess acid addition had a profound effect, which is reflected in the repeatable charge-discharge performance shown in the Fig 4.13. The voltage, charge and energy efficiencies calculated for each cycle are also plotted in Fig 4.14. The charge efficiency ($\cong$ 95 %) is substantially higher on comparison to that of the soluble lead acid

battery (≅ 85 %), while the voltage efficiency remains at ≅ 65 %. The energy efficiency is ≅ 55 %.

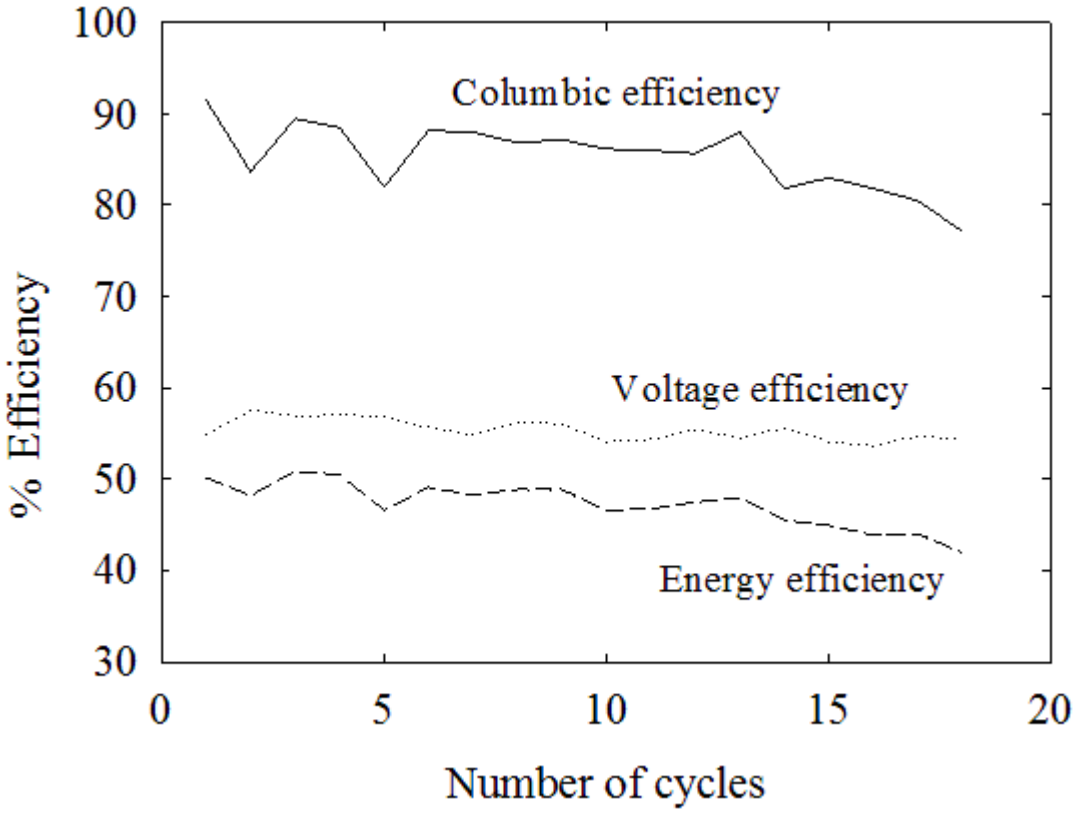

Fig 4.14: The efficiency curves for the charge-discharge performance for a 6 cm^2 electrode cell from 0.5 mol dm^{-3} Cu^{2+} and 0.5 mol dm^{-3} Pb^{2+} in a 1 mol dm^{-3} MSA electrolyte.

The presence of excessive acid also influenced the performance on the first cycle. After repeated cycling, successful operation was not possible with the 6 cm^2 test cell. The excess acid concentration was reduced 10 fold to 0.1 mol dm^{-3}, in the scaled-up test using a 100 cm^2 cell. Hence, a refined combination of 0.5 mol dm^{-3} Cu^{2+} and 0.5 mol dm^{-3} Pb^{2+} with an excess acid concentration of 0.1 mol dm^{-3} MSA was tested in the 100 cm^2 test cell at a linear flow velocity of 4 cm s^{-1}, for 30 min charge-discharge cycles at a constant current of 20 mA cm^{-2} using 100 cm^2 Entegris carbon electrodes.

The above test yielded a vastly improved charge-discharge performance beyond 182 cycles. This stable charge-discharge behaviour can be observed in Fig 4.15. The resulting average charge, voltage, and energy efficiencies were 93 %, 62 % and 57 %, respectively. These values were comparable to those of the soluble lead acid flow battery. This combination was tested extensively for cyclability, yielding stable performance and a reduced degree of forming insoluble oxide(s) of lead.

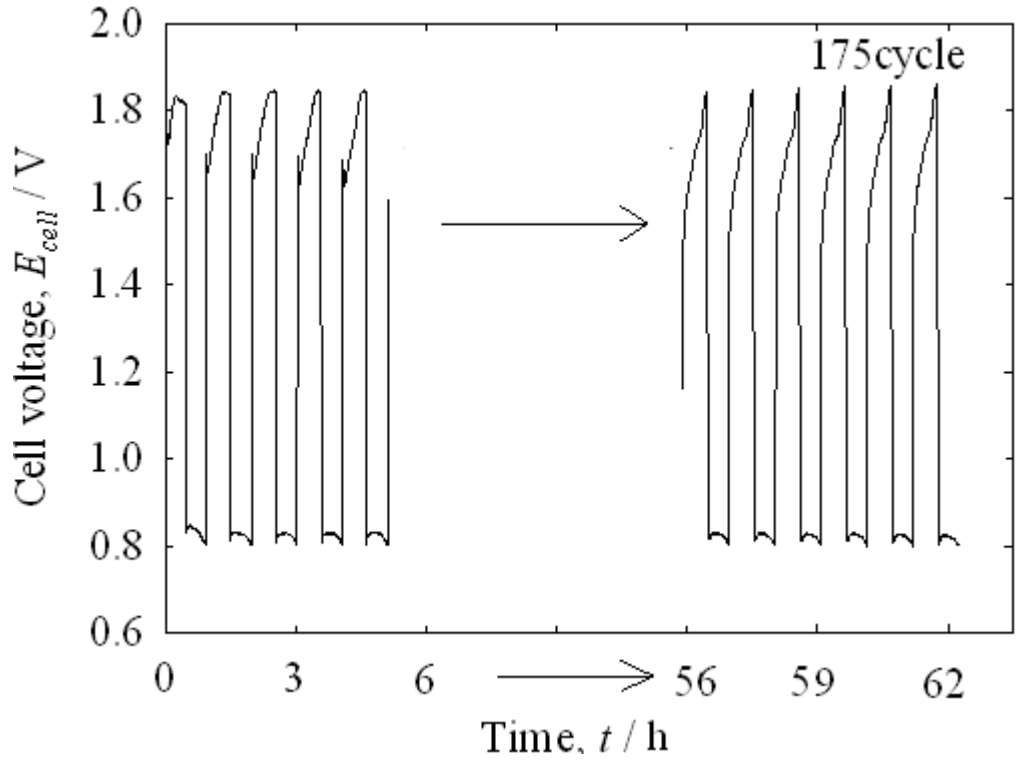

Fig 4.15: Charge-discharge performance (of 175 cycles) for a 100 cm^2 electrode cell using 0.5 mol dm^{-3} Cu^{2+} and 0.5 mol dm^{-3} Pb^{2+} in 0.1 mol dm^{-3} MSA a s the electrolyte. Tests were carried out at a linear flow velocity of 4 cm s^{-1}, for 30 min charging and a constant current density discharge at 20 mA cm^{-2} using a cut-off cell voltage of 0.8 V

Photographic images of the deposits (Fig 4.16) reveal lead dioxide as well as copper deposits on the positive and negative electrodes, respectively. The sedimentation of falling lead dioxide deposit can also been observed at the edge of the flow chamber inlet in Fig 4.16 (b). Beyond 182 cycles the localized dendrite formation on the copper deposit, which

can be seen in Fig 4.16(a) (encircled), caused a short circuit, which let to the failure of the battery.

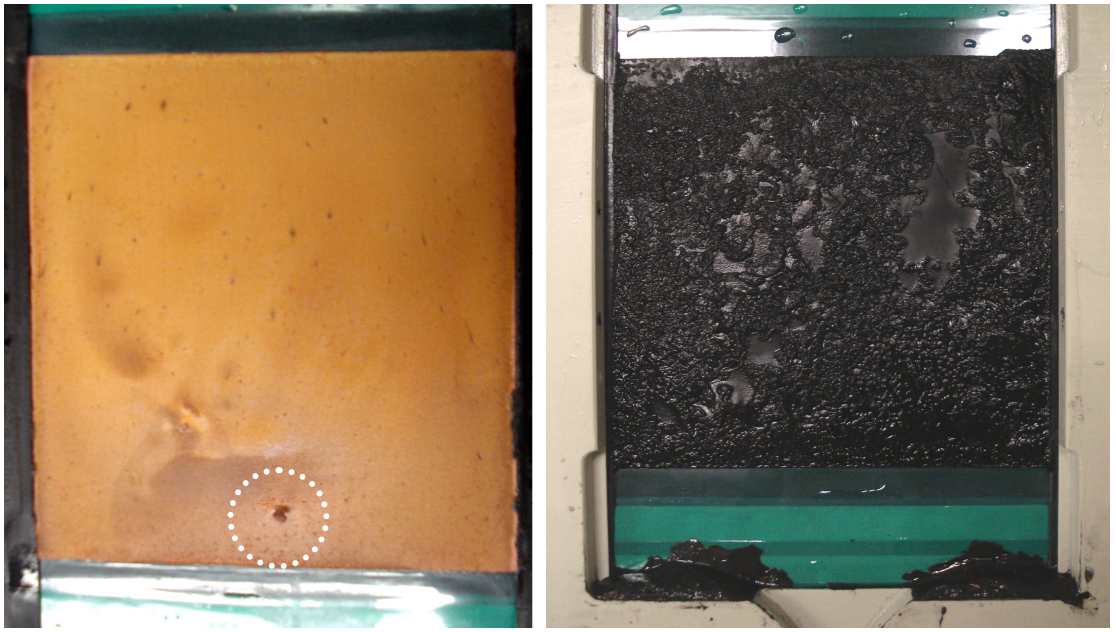

(a) (b) 10 cm

Fig 4.16: Photographs showing the deposits on the: (a) negative (copper) and (b) positive (lead dioxide) electrodes from 0.5 mol dm^{-3} Cu^{2+} and 0.5 mol dm^{-3} Pb^{2+} in 0.1 mol dm^{-3} MSA at a constant current of 20 mA cm^{-2}.

4.4. Further work and conclusions

4.4.1. Further work

The copper-lead dioxide flow battery concept, based on copper and lead dioxide, has been proposed. An electrolyte of 0.5 mol dm^{-3} Cu^{2+} and 0.5 mol dm^{-3} Pb^{2+} in 0.1 mol dm^{-3} MSA was used, but further investigation of the fundamental electrochemistry is required for achieving high-efficiency performance of the battery. In particular, the following aspects are in need of further investigation:

1. The nucleation, growth and dissolution of the negative-electrode deposits, due to the recurring peak during the deposition of copper as shown in Fig 4.4.

2. The effect of individual additives and their combinations, on individual electrode deposits and in the total solution, involving hydrodynamic tools of voltammetry.
3. Further cyclability testing of the suitable additives with the optimised combination of 0.5 mol dm^{-3} Cu^{2+} and 0.5 mol dm^{-3} Pb^{2+} in 0.1 mol dm^{-3} MSA electrolyte, along with further scale-up testing.
4. The exact influence of the concentration of lead ions (available in the electrolyte) on the electrodeposits and performance of the battery.

4.4.2. Conclusion

A novel, undivided flow battery using carbon-vinyl ester composite electrodes and an electrolyte with Cu^{2+} and Pb^{2+} in additive-free MSA has been developed. This is in contrast to a system using a lead dioxide electrode and a carbon-fiber doped graphite electrode, with an electrolyte based on the more corrosive sulfuric acid[5]. The diffusion coefficients for copper and lead ions in the electrolyte were calculated as 5.1 ± 0.5 x 10^{-6} cm^2 s^{-1} and 4.8 ± 0.4 x 10^{-6} cm^2 s^{-1}, respectively, which were in good agreement with the literature values as discussed in section 4.3.1.

The unit cell open-circuit voltage was 1.3 V after charge and 0.3 V after discharge at 20 mA cm^{-2} for 0.5 h charge–discharge cycles.An electrolyte of 0.5 mol dm^{-3} Cu^{2+} and 0.5 mol dm^{-3} Pb^{2+} in 0.1 mol dm^{-3} MSA was used, together with a linear flow velocity 4 cm s^{-1}. The average charge efficiency was nearly 89 %, the voltage efficiency was around 55 % and dendrite formation or heavy shedding (similar to that of the soluble lead-acid flow battery) was reduced, compared to systems based on sulfuric acid[5,6,33]. The copper-lead dioxide cell could potentially be a good secondary battery for energy storage in combination with a renewable source of energy. This is mainly due to its low cost and recyclable electrolytic chemical species, along with the environmentally-friendly acid.

The effect of additives has also been investigated, suggesting a method for achieving a significant improvement in the performance. The proposed combinations of (0.5 mmol dm^{-3} HDTMAH + 0.5 gm dm^{-3} PEG + 50 gm dm^{-3} Cl^-), (0.5 gm dm^{-3} PTFE + 0.5 gm dm^{-3} PEG + 50 gm dm^{-3} Cl^-), 0.5 mmol dm^{-3} HDTMAH and 50 gm dm^{-3} Cl^- have also been tested, yielding successful results (reflected in the efficiency values of the battery). When a low acid concentration (0.1 mol dm^{-3}) was used, a suitable lead dioxide deposit was formed, as well as a bright and shiny copper deposit with a reduced degree of dendrite or nodular formation, leading to further improvements in performance.

References

[1]. M. Schlensinger and M. Paunovic, "*Modern Electroplating*", 4th edition, John Wiley and Sons. Inc.© 2000.

[2]. D. Pletcher and F.C. Walsh, *Industrial Electrochemistry*, Chapman and Hall, London, 1991.

[3]. A. Agrawal, S. Kumari, K.K. Sahu, *Ind. Eng. Chem. Res.,* **48** (2009) 6145.

[4]. C.T.J. Low and F.C. Walsh, *Surf. Coat. Technol*, **202** (2008) 1339.

[5]. D. Pletcher, H. Zhou, G. Kear, C.T.J. Low, F.C. Walsh, R.G.A. Wills, *J. Power Sourc.*, **180** (2008) 621.

[6]. J. Pan, Y. Sun, J. Cheng, Y. Wen, Y. Yang, P. Wan., *Electrochem. Commun.*, **10** (2008) 1226.

[7]. M. Sun, T.J. O'Keefe, *Metallurg. Trans.*, **23B** (1992) 591.

[8]. H.Y. Peng, H.Y. Chen, W.S. Li, S.J. Hu, H. Li, J.M. Nan, Z.H. Xu, *J. Power Sourc.*, **168** (2007) 105.

[9]. D. Gernon, M. Wu, T. Buszta, P. Janney, *Green Chem.*, **1** (1999) 127.

[10]. C.T.J. Low, F.C. Walsh, *Surf. Coat. Technol.,* **202** (2008) 3050

[11]. A. Hazza, D. Pletcher, R.G.A Wills, *Phys. Chem. Chem. Phys.*, **6** (2004)1773.

[12]. http://www.pineinst.com/echem/viewproduct.asp?ID=46876, accessed on April 24, 2011.

[13].http://www.autolab-instruments.com/?pag=12/., accessed on April 24, 2011.

[14].http://www.kocour.net/productDetail.asp_Q_catID_E_93_A_subCatID_E_101_A_productID_E_135#., accessed on April 24, 2011.

[15]. B. Panda, S.C. Das, R.K. Panda, *Hydrometallurgy*, **95** (2009) 87.

[16]. C. Ponce-de-Léon, F.C. Walsh, *Trans. Inst. Met. Fin.*, **81** (5) 2003.

[17]. M. Rosso, *Electrochim. Acta*, **53** (2007) 250.

[18]. A.B. Velichenko, R. Amadelli, E.V. Gruzdeva, T.V. Luk'yanenko, F.I. Danilov, *J. Power Sourc.,* **191** (2009) 103.

[19]. D. Pletcher, H. Zhou, G. Kear, C.T. J. Low, F.C. Walsh, R.G.A. Wills, *J. Power Sourc.,* **180** (2008) 630.

[20]. D. Pletcher, R.G.A Wills, *Phys. Chem. Chem. Phys.*, **6** (2004)1779.

[21]. L. Bonou, M. Eyraud, R. Denoyel, Y. Massiani, *Electrochim. Acta*, **47** (2002) 4139.

[22]. M. Quinet, F. Lallemand, L. Ricq, J.-Y. Hihn, P. Delobelle, C. Arnould, Z. Mekhalif, *Electrochim. Acta*, **54** (2009) 1529.

[23]. V.A. Vas'ko, I. Tabakovic, S.C. Riemer, M.T. Kief, *Microelectron. Eng*., **75** (2004) 71.

[24]. T.P. Moffat, D. Wheeler, D. Josell, *J. Electrochem. Soc.*, **151** (2004) C262.

[25]. A. Radisic, A.C.West, P.C. Searson, *J. Electrochem. Soc.*, **149** (2002) C94.

[26]. L. Bonou, M. Eyraud, R. Denoyel, Y. Massiani, *Electrochim. Acta*, **47** (2002) 4139.

[27]. K. Kondo, T. Matsumoto, K. Watanabe, *J. Electrochem. Soc.*, **151** (2004) C250.

[28]. C.T.J. Low, D. Pletcher, F.C. Walsh, *Electrochem. Commun.*, **11** (2009) 1301.

[29]. S.P. Tong , C.A. Ma, H. Feng, Electrochim. Acta, **53** (2008) 3002.

[30]. A. Hazza, D. Pletcher, R. Wills, *J. Power Sourc.,* **149** (2005) 103.

[31]. E. Expósito, J. Iniesta, J. González-García, V. Montiel and A. Aldaz, *J. Power Sourc.,* **92** (2001) 260

[32]. J. Collins, G. Kear, X. Li, C.T.J. Low, D. Pletcher, R.C. Tangirala, D.S. Campbell, F.C. Walsh, C. Zhang, *J. Power Sourc.*, **195** (2010) 1731.

[33]. X. Li, D. Pletcher, F.C. Walsh, *Electrochim. Acta,* **54** (2009) 4688.

Chapter-V

Conclusions and further work

5.1. Conclusions

This thesis has presented work on the construction, operation and development of three flow batteries at various levels of research, along with chemical investigations involving the selection of redox-couples, the electrochemistry and the characterization of the chemical species. The performance of these batteries under the influence of different operational parameters such as current density, concentration of chemical species, flow rate and additives, together with variation in the constructional parameters such as flow distribution, surface preparation, electrode area and electrode materials has also been investigated. The following conclusions have been reached for the individual RFBs investigated.

- *All-vanadium RFB*: A simplified control-oriented model with minimal parameter fitting has been developed, to measure and analyze the performance (cell voltage and SoC) of the battery under different operational and constructional parameters. The model can readily be extended to other RFBs involving soluble species, and can be used as the basis for a stack model, which would be highly desirable given the current drive towards commercialization.

- *Soluble lead-acid RFB*: The success in the development of this battery from fundamental (0.1261 cm^2) to a test-scale (100 cm^2) level in the laboratory, has propelled it towards pilot-scale studies (1200 cm^2). Although the problems of dendritic lead and inefficient lead dioxide deposits linger on, the operational and the parametric studies in this thesis have provided (for the test-scale cells of around 100 cm^2) the definitive electrolytic composition of the range of concentrations to be used (0.5-1 mol dm^{-3}); the additive required for stable and reproducible electrodeposits (0.005 mol dm^{-3} of HDTMAH); the optimal ranges of current densities (10–40 mA cm^{-2}) and flow rates (1–2 cm s^{-1}) and a

chemical cleaning technique using H_2O_2 for regenerative recycling employing a Ni-C electrode pair as the electrode materials.

- *Copper-lead dioxide RFB*: The work on this RFB in this thesis was a proof-of-concept, from the basic selection of redox couples to stabilizing the operation of a test cell (100 cm^2). The short study of this conceptual level of operation has given insight into the required electrolytic concentration of the species (0.5-1 mol dm^{-3}), the nature of the electrodeposits, possible additive combinations for stable electrodeposits ((0.5 mmol dm^{-3} HDTMAH + 0.5 gm dm^{-3} PEG + 50 gm dm^{-3} Cl^-), (0.5 gm dm^{-3} PTFE + 0.5 gm dm^{-3} PEG + 50 gm dm^{-3} Cl^-), 0.5 mmol dm^{-3} HDTMAH and 50 gm dm^{-3} Cl^-), and the efficiency of flow battery.

The following table gives the simplified cost comparison of the three RFBs discussed above, in terms of costs associated with installation and operational lifetime for each flow battery. It also give the replacement lifetime for each RFB, as well as recyclability and losses associated with a MW-scale RFB installation.

RFB system	**Capital cost (£ kWh^{-1})**	**Replacement period (20 years)**	**Replacement cost (£ kWh^{-1})**	**Recyclable**	**Losses**
All-vanadium	400 – 600	12 – 15	370	Yes	Flow
Soluble lead-acid	250 – 500	9 – 11	245	Yes	Flow and electrode deposits
Copper-lead dioxide†	200 – 400†	8 – 10†	230†	Yes†	Flow and electrode deposits

Table 5.1: Comparison of cost estimates (includes a maximum inflation of 5 %) for the all–vanadium, soluble lead–acid and copper–lead dioxide RFBs. († predicted)

5.2. Further work

The future work required for the development of the all-vanadium, soluble-lead acid and copper-lead dioxide RFBs has been described in detail at the end of each chapter (*sections 2.5*, *3.4.2* and *4.4.4*, respectively). The following areas require specific investigations in all three RFBs:

- *Temperature*: Although the effect of temperature has been analyzed through the model in case of the all-vanadium RFB, its effect is to be verified experimentally on the life of the membrane, efficiency of operation and solubility of the chemical species in all three RFBs.

- *Stack operation and commercialisation*: The effects of operational parameters have also to be studied at the stack level to achieve commercial status of the RFBs. While commercialised versions of the all-vanadium RFB are currently on the market, the soluble lead-acid RFB is still under development for commercial purposes and the copper-lead dioxide RFB requires further research into various aspects of its performance before stack operation can be realised.